Drilling and sampling a natural CO2 reservoir: Implications for fluid flow and CO2-fluid–rock reactions during CO2 migration through the overburden

N. Kampman, M.J. Bickle, A. Maskell, H.J. Chapman, P. Evans, G. Purser, Z. Zhou, F. Schaller, J.C. Gattacceca, P. Bertier, et al.

Drilling and sampling a natural CO_2 reservoir: implications for fluid flow and CO_2-fluid-rock reactions during CO_2 migration through the overburden

N. Kampman[1,2,3*], A. Maskell[1], H.J. Chapman[1], M.J Bickle[1], J.P. Evans[4], G. Purser[3], Z. Zhou[2], J. Gattacceca[1], M. Schaller[5,6], P. Bertier[7], F. Chen[1], A.S. Turchyn[1], N. Assayag[1,8], C. Rochelle[3] and A. Busch[9]

[1]Department of Earth Sciences, University of Cambridge, Downing Street, Cambridge CB2 3EQ, UK
[2]Lancaster Environment Centre, University of Lancaster, Bailrigg, Lancaster LA1 4YQ, UK
[3]British Geological Survey, Environmental Science Centre, Keyworth, Nottingham NG12 5GG, UK
[4]Department of Geology, Utah State University, 4505 Old Main Hill Logan, UT 84322-4505
[5]Department of Earth and Planetary Sciences, Rutgers University, 610 Taylor Road, Piscataway, NJ 08854-8066
[6]Department of Geological Sciences, Brown University, 324 Brook St., Providence, RI 02912
[7]RWTH Aachen University, Bunsenstrasse 8, 52072 Aachen, Germany
[8]UPMC, Université Pierre et Marie Curie, ISTEP, Institut des Sciences de la Terre de Paris, F-75005, Paris, France
[9]Shell Global Solutions International, Kessler Park 1, 2288 GS Rijswijk, The Netherlands

*corresponding author: n.kampman@lancaster.ac.uk

Abstract

This paper presents the initial results of a scientific drilling project to recover core and pressurized fluid samples from a natural CO_2 reservoir, near the town of Green River, Utah. The drilling targeted a stacked sequence of CO_2-charged Jurassic sandstone reservoirs and caprocks, situated adjacent to a CO_2-degassing normal fault. This site has actively leaked CO_2 from deep supercritical CO_2 reservoirs at depth >2km within the basin for over 400,000 years. The project objectives were to gather samples to examine reactive fluid flow in the reservoirs, caprocks and faults, during migration of CO_2 through the geological overburden from the deep supercritical CO_2 reservoirs. Downhole fluid sampling and fluid element and isotope geochemistry show that the shallow reservoirs are being actively fed by inflow of CO_2-saturated brines through the faults. Comparisons of shallow and deep fluid geochemistry suggests that: (i) CO_2 and CO_2-charged brines co-migrated from the deep reservoirs, (ii) the CO_2-saturated brines migrating from depth interact with significant volumes of meteoric groundwater in aquifers in the shallower Permian and Jurassic sandstones, diluting the brine composition, and (iii) that a significant fraction of the CO_2 migrating from depth is dissolved in these brine-meteoric water mixtures, with >99% of the CO_2 in fluids sampled from the shallow reservoirs being derived during fluid migration, after the fluids left their source reservoir. The $^{87}Sr/^{86}Sr$ ratio of the brine flowing through the faults is significantly elevated due to the addition of Sr from silicate mineral dissolution during fluid migration.

The association of bleached sandstones in the core with CO_2-rich fluids supports interpretations from elsewhere that CO_2-charged brines with CH_4 or H_2S reductants can dissolve hematite present within the sediment. Analysis of fluid geochemistry and

sandstone petrology suggest that the CO_2-rich fluids dissolve carbonate, hematite and gypsum in the reservoirs, as they flow away from the faults.

Element and isotope geochemistry of fluid samples from the drillhole and Crystal Geyser constrain mixing models which show that, within the Navajo Sandstone, the reservoir fluids are undergoing complex mixing of: (i) CO_2-saturated brine inflowing from the fault, (ii) CO_2-undersaturated meteoric groundwater flowing through the reservoir and (iii) reacted CO_2-charged brines flow through fracture zones in the overlying Carmel Formation caprock, into the formations above. Such multi-scale mixing processes may significantly improve the efficiency with which groundwaters dissolve the migrating CO_2.

1 Introduction

Understanding the geochemical behaviour of carbon dioxide stored in geological reservoirs, over a range of time-scales, is crucial for quantifying the risk of leakage and the geochemical evolution of the stored CO_2 through the life of an individual storage site (see review in Kampman *et al.,* 2013 this issue). CO_2 dissolution in brine will tend to stabilize the CO_2 in storage reservoirs (e.g. Gilfillan *et al.,* 2009) and reactions between CO_2-charged brines and reservoir minerals might either enhance the long-term storage security by precipitation of carbonate minerals or facilitate leakage through mineral dissolution and corrosion of caprocks and fault seals (e.g. Bickle, 2009). A further concern is that migration and intrusion of CO_2 will drive acidification of potable groundwaters which may mobilize potentially toxic trace metals.

Buoyant supercritical CO_2 may migrate from a storage reservoir through fractured or corroded caprocks, permeable fault zones or laterally discontinuous seals. Understanding the fluid-fluid and fluid-rock reactions that may retard the migration of CO_2 from deep storage sites to the surface is of critical importance for demonstrating the retentive capacity of the geological overburden, above deep storage reservoirs. Concerns that may arise during the migration of CO_2 through the overburden include escape of CO_2 to the surface and contamination of shallow potable aquifers by: (i) intrusion of CO_2, resulting in dissolution and desorption of potentially toxic metals from minerals by acidic CO_2-charged fluids and (ii) entrainment of deep formation brine with the migrating CO_2, which may contain high concentrations of metals and radionuclides.

Fluid-rock reactions involving Fe-oxide minerals are a potential source of contaminants in CO_2-charged groundwaters. Elevated trace metal concentrations from

mineral dissolution and pH driven desorption reactions are predicted from modelling studies (e.g. Apps et al., 2010), experiments (e.g. Little and Jackson, 2010) and recent field tests (e.g. Trautz et al., 2012); however shallow CO_2-injection field experiments have not shown hazardous levels of contamination in the short-term (Kharaka et al., 2010; Trautz et al., 2012). The reducing conditions present in deeper geological formations may enable more effective rates of Fe-oxide and Fe-oxyhydroxide dissolution in the presence of elevated CO_2 concentrations (e.g. Frio Brine Pilot Experiment; Kharaka et al., 2006).

The efficiency of the geological overburden for dispersing and trapping a migrating CO_2 plume can only be established from engineered CO_2-injection leakage experiments or direct observations from leaking natural CO_2 accumulations, with the latter allowing observations of processes on the timescales required for CO_2 storage. Numerical modelling studies (e.g. Doughty and Myer, 2009; Zhou *et al.,* 2010), while providing valuable information on likely large scale flows and pressure changes, lack the resolution to properly track CO_2 dissolution and fluid-mineral reactions in reservoirs with heterogeneities characteristically on 10 cm scales, given their grid-scales of metres to hundreds of metres.

In this paper we discuss the initial results of a core and a downhole fluid sampling campaign during recent scientific drilling of a natural CO_2 system at Green River, Utah. The ~322 m deep vertical hole was drilled in July 2012, penetrating a stacked sequence of CO_2-charged sandstone reservoirs and their intervening caprocks. These shallow reservoirs are filled through a normal fault system through which CO_2 and CO_2-charged fluids migrate from deep supercritical CO_2 reservoirs at depth within the basin. We present the initial results of surface and downhole fluid sampling during drilling of the CO_2 reservoirs and some preliminary observations from the recovered core. Analytical methods to recover pH and CO_2 content of pressurized fluid samples onsite are presented. Element and isotope

115 geochemistry of the fluid samples recovered from the drill hole are used to examine fluid
116 flow, fluid-fluid mixing and fluid-rock reactions in the faulted CO_2-reservoirs. The results are
117 supported by: (i) published analyses of brine compositions from the deep supercritical CO_2
118 reservoirs sampled during oil well exploration drilling and (ii) long-term sampling and
119 monitoring of fluid geochemistry from Crystal Geyser sourced from the underlying CO_2
120 reservoirs. Interpretation of the fluid-rock reactions occurring within the CO_2 reservoirs
121 inferred from the fluid geochemistry is supported by preliminary petrographic and
122 mineralogical observations from the core.

123 **1.1 Leaking natural CO_2 reservoirs of the South Western USA**

124 The greater Colorado Plateau and Southern Rocky Mountains region, USA, contains a
125 number of natural CO_2 reservoirs (Allis *et al.,* 2001; reviewed in Bickle *et al.,* 2013). This
126 includes the stacked sequence of CO_2-reservoirs in Jurassic, Permian and Carboniferous
127 sediments of the northern Paradox Basin, near the town of Green River, Utah (Fig. 1-3).
128 Many of these natural reservoirs have contained CO_2 securely for thousands to millions of
129 years. This has been used to argue for the stability of CO_2 in geological reservoirs and that
130 the long-term integrity of caprocks can be preserved in the presence of CO_2 and CO_2-
131 charged fluids. Whilst it is expected that a well-sited CO_2 storage facility will not leak, some
132 natural CO_2 reservoirs (such as the Green River site) have conductive features where CO_2
133 and CO_2-charged fluids are able to escape from deep reservoirs of supercritical CO_2 to
134 surface. The accumulations at Springerville-St Johns Dome, Arizona and Green River, Utah
135 currently leak CO_2 through faults and possess fault-associated, surface travertine deposits
136 attesting to CO_2 leakage in the recent and geological past (Fig 3; Allis *et al.,* 2005, Burnside
137 *et al.,* 2013; Gilfillan *et al.,* 2011; Kampman *et al.,* 2012; Keating *et al.,* 2010, 2012, 2013).
138 Radiometric dating of these surface travertine deposits attest to leakage from the St Johns

Dome accumulation for >350ka (Embid and Crossey, 2009) and from the Green River accumulation for >400ka (Burnside *et al.,* 2013; Kampman *et al.,* 2012). The long-lived nature of CO_2 accumulations penetrated by large conductive faults raises a number of important questions about the rates and mechanism of leakage from deep geological reservoirs to the surface. What are the intrinsic permeabilities of faults at depth to supercritical/gaseous CO_2 and/or CO_2-charged brines? What impact does fluid-rock reactions with supercritical CO_2 and CO_2-charged fluids have on fault permeability? Does surface CO_2 leakage at these sites reflect migration of a discrete CO_2-phase or degassing of CO_2-charged fluids in the shallow subsurface? Are these natural reservoirs being continuously recharged with CO_2 or are leakage rates sufficiently small so as not to dissipate the accumulations over geological time-scales? Some of these questions may be addressed by drilling and sampling of fluids and rock core from the reservoirs, faults and geological overburden.

2 Green River Natural CO_2 Accumulation and Hydrology

CO_2-charged fluids leak to surface along the Green River anticline where they form a series of CO_2 springs and geysers, including the spectacular Crystal Geyser (Fig. 3; Assayag *et al.,* 2009; Baer and Rigby, 1978; Burnside et al., 2013; Dockrill and Shipton, 2010; Evans *et al.,* 2004; Gouveia and Friedmann, 2006; Gouveia *et al.,* 2005; Han *et al.,* 2013; Heath, 2004, 2009; Kampman *et al.,* 2009, 2012; Pasala *et al.,* 2013 Shipton *et al.,* 2005; Shipton *et al.,* 2004; Vrolijk *et al.,* 2005). The natural springs discharge from the footwalls of the Little Grand Wash and Salt Wash normal faults but abandoned oil exploration and water wells leak CO_2 over a wider region (Fig. 1-4). Oil exploration drilling has encountered accumulations of: (i) CO_2 gas and CO_2-charged brine in the Navajo Sandstone at depths of

~200-350 m, (ii) CO_2 gas and CO_2-charged brine in the Jurassic Wingate Sandstone at depths of ~400-500 m, (iii) accumulations of supercritical CO_2 and CO_2-charged brine in the Permian White Rim Sandstone at depths of ~800-900 m, and (iv) supercritical CO_2 and CO_2-charged brine in Carboniferous (Pennsylvanian and Mississippian) aged carbonate and evaporite deposits at depths >900m (Fig. 2; Jay Beach, Delta Petroleum pers. comm. 2007; Drilling Reports e.g. Navajo Sandstone - Greentown State 36-11, API 4301931462; Wingate - Greentown Federal 26-43D, API 4301931547; White Rim - Green Town Federal 35-12, API 4301931507).

The surface exposures, CO_2 springs along the fault zones, stacked sequence of reservoirs, the relatively shallow depth (160-350m) of the upper CO_2-bearing reservoir, the Navajo Sandstone and the prior knowledge of the site made it an excellent drilling target to document processes within a leaking CO_2-charged system.

2.1.1 Structural Geology

The Little Grand Wash and Salt Wash normal faults are 35-40 km in lateral extent and contain a clay gouge core, surrounded by a fault damage zone of high angle open fractures orientated parallel to the fault (Dockrill and Shipton, 2010; Shipton *et al.,* 2004, 2005; Vrolijk *et al.,* 2005). Formation top data from oil exploration drill-holes constrains the penetration depth of the faults to at least the Carboniferous strata, and they probably penetrate deeper. Dockrill and Shipton (2010) conclude that the faults are laterally sealing towards the fault center, with throws of 250-300 m, but become laterally transmissive towards the fault tips, where reservoir-reservoir rock is juxtaposed (Fig 4; Dockrill and Shipton, 2010). Buoyant supercritical and gaseous CO_2 is thought to accumulate at the crest of the Green River anticline, adjacent to the two faults, beneath the south dipping fault seals. Open fractures in the fault damage zone allow CO_2 and CO_2-charged brines to escape

upwards under artesian head, from the deep supercritical CO_2 reservoirs (Fig. 3-5; e.g. Pasala *et al.,* 2013). CO_2-leakage points away from the faults (Fig. 3; Tumble Weed Geyser and Chaffin Ranch Geyser) occur where exploration or water well drill-holes penetrate fluids in the Navajo Sandstone flowing horizontally away from the fault tips under a regional hydraulic head (Hood and Patterson, 1984; Kampman *et al.,* 2009). Details of the local hydrology are discussed in Kampman *et al.,* (2009) and the regional hydrology is discussed in Hood and Patterson (1984).

2.1.2 Ancient Travertine Deposits

Ancient travertine deposits overlie damage zones in the footwall blocks of both the Little Grand Wash and Salt Wash faults (Fig. 3; Burnside *et al.,* 2013; Kampman *et al.,* 2012). The travertine mounds are localized to the intersection of the faults with the apex of the Green River anticline and the mounds are distributed along a considerable portion of the faults' lengths to the east and west (Fig. 3). U-Th dating of the deposits attests to leakage of CO_2 from the site for at least the last 400ka (Burnside *et al.,* 2013). Kampman *et al.,* (2012) argue that there were successive pulses of CO_2-leakage with a periodicity controlled by climate driven changes in formation fluid over-pressure and the hydraulic behaviour of the faults. Pulses of CO_2 and CO_2-charged brine injection, recorded by changes in the geochemistry of surface travertines, are argued to have been accompanied by increased rates of CO_2 degassing from the faults. These pulses occurred at the transition from local glacial to interglacial conditions following climate warming and crustal unloading during drainage of pluvial lakes and the retreat of mountain glaciers in the region (Kampman *et al.,* 2012).

2.1.3 Crystal Geyser, Tenmile Geyser and the Green River Airport Well

The modern day Crystal Geyser erupts from an abandoned exploration drill-hole Ruby #1 State Well drilled in 1935, which reached a total depth of ~800m in the upper portions of the Permian White Rim Sandstone (Baer and Rigby, 1978). The drill-hole was uncased and is now rubble filled below a depth of ~15 m, having been dynamited in the 1990s (Han *et al.,* 2013; Shipton *et al.,* 2004). It is likely that the drillhole is only weakly or non-transmissive at depths greater than the Navajo Sandstone. The saline fluid expelled from Crystal Geyser is thought to predominantly originate from the Navajo Sandstone, and emanation temperatures are consistent with a fluid largely derived from this depth (Baer and Rigby, 1978; Heath *et al.,* 2009; Kampman *et al.,* 2009). The waters expelled from Crystal Geyser and the CO_2-springs have previously been shown to contain variable mixtures of meteoric waters, derived from areas of groundwater recharge in the San Rafael Swell (Hood and Patterson, 1984), and evaporite derived brines from the deep Carboniferous formations input along with the CO_2 (Kampman *et al.,* 2009; Wilkinson *et al.,* 2009).

Two other important CO_2-springs in the area, discussed in this study, are Tenmile Geyser and the Green River Airport Well. Tenmile Geyser escapes from an abandoned petroleum exploration well, situated within hangwall block of the Salt Wash Graben fault. The spring is notable for the large fraction of deeply derived brine in the expelled fluid (Kampman *et al.,* 2009), elevated concentrations of N_2, Ar, He and CH_4 in the exsolved gas (this study) and an anomalous $CO_2/^3He$ ratio (Wilkinson *et al.,* 2009). The Green River Airport well escapes from exploration drill-hole Grand Fault 14-24. This drill-hole was sited within the footwall block of the Little Grand Fault, on the westerly limb of the Green River anticline and originally penetrated to the base of the Mississippian Leadville Limestone at 3.2km. This CO_2-spring emits warm (~27^oC) fluid sourced from the Navajo Sandstone, and

lies on a fluid flow path running along the length of the Little Grand Fault, up-stream of Crystal Geyser (Fig. 3). It is the most proximal spring to zones of groundwater recharge in the San Rafael Swell, and contains CO_2 inputs from depth without the addition of significant brine from deeper formations (Kampman *et al.,* 2009).

3 Field Sampling and Analytical Methodology

3.1 Scientific Drilling

Drilling of hole CO2W55 was carried out from 2nd-28th July, 2012, using a CS4002 Truck Mounted Core Drill by DOSECC Inc (Fig. 5). The drilling and fluid sampling methods are presented in detail in Kampman *et al.,* 2013a. The drill site is located on the footwall block of the Little Grand Wash Fault (Fig. 2, 5; 38.93792 N, -110.13892 W, 1238 m Elev.), ~90m north of the main fault trace of the Little Grand Fault and ~285 m to the west of Crystal Geyser (Fig 5). The fault damage zone In the vicinity of the drill site currently emits dry CO_2 gas (Allis *et al.,* 2005; Han *pers comms,* 2013) and has hosted CO_2 and CO_2-charged fluid discharge in the geological past, being overlain by ancient travertine deposits (Dockrill and Shipton, 2010; Doelling, 1994; Shipton *et al.,* 2004).

3.1.1 Core Stratigraphy and CO_2-Charged Zones

The vertical hole was drilled to a depth of 322.5 m using DOSECC's hybrid coring system with >99% core recovery (Fig. 6). Fluid samples were collected during drilling from fluid returns to surface and using a wireline downhole fluid sampling tool to recover fluid samples at formation pressures. The drill hole transected three Jurassic formations; the Entrada Sandstone, Carmel Formation and Navajo Sandstone (Fig. 6-7).

From surface, the drill-hole transected ~35 meters of marine and lacustrine red siltstone facies of the 'Earthy' Entrada Sandstone member which grade into the 115 m-thick

aeolian dune deposits of the lower Entrada Sandstone, with intercalated marginal marine and sabkha influences throughout (see Crabaugh and Kocurek, 1993). The basal units comprise fine-to medium-grained quartz-arenite to subarkosic sandstone (76–89 wt% quartz, 8.5–16.5 wt% K-feldspar, 2.2–6.5 wt% plagioclase, and trace muscovite, tourmaline, apatite and zircon), variably cemented with quartz, calcite and dolomite (Beitler et al., 2004; Wigley *et al.,* 2012). Free CO_2 gas and CO_2-charged fluids were first encountered in the basal 35-150 m of the Entrada Sandstone, which is not overlain by a regional caprock, indicating that thin siltstone layers (such as those within the Entrada) can act as effective seals to the upward migration of CO_2 and CO_2-charged fluids. Zones of CO_2-bearing fluids were identified based on the presence of CO_2-degassing in intervals of the core, and CO_2-charged fluid returns to surface.

Below the Entrada lies the Carmel Formation (top at 149 mbs), a 50 m-thick complex sequence of three laterally gradational lithofacies including: (i) interbedded, unfossiliferous red and grey shale and bedded gypsum, (ii) red and grey mudstone/siltstone, and (iii) fine-grained sandstone. These are interpreted as marine sediments deposited in quiet, subtidal conditions under the influence of periodic hypersaline water and form a regional seal (Blakey *et al.,* 1997; Peterson and Turner-Peterson, 1989). Within the Carmel Formation the drill core intersected a ~17m thick fracture zone comprising a ~6m thick core containing meter scale blocks of siltstone and shale breccia hosted in remobilized gypsum beds. These are bound by a zone of intense fracturing, comprising low (1-20^o) and high angle (70-89^o) gypsum-filled open fractures over a ~2m thick interval in the hangwall and ~9m thick interval in the footwall. The footwall fractures are characterized by high-angle 70-80^o striated surfaces with mm to cm normal offsets. The footwall fracture zone was found to bear CO_2-charged fluid.

279 The Carmel Formation is underlain by the ~122m thick Navajo Sandstone which
280 regionally and locally is a homogenous unit comprising thick sets of high-angle cross-
281 bedded, well-sorted, fine- to medium-grained aeolian sandstone with internal stratification
282 (see Verlander, 1995 and references therein). The entire cored interval of the Navajo
283 Sandstone was found to contain CO_2-charged fluid. The Navajo Sandstone in the northern
284 Paradox Basin is a quartz-arenite to subarkosic fine-to medium-grained sandstone,
285 dominated by quartz (72–86 wt.%) and K-feldspar (6–11 wt.%) with minor amounts of
286 plagioclase (1–3 wt%) and trace heavy mineral fractions of tourmaline, apatite and rutile (<1
287 wt.%) (Beitler *et al.,* 2005; Cooley *et al.,* 1969; Harshbarger *et al.,* 1957; Parry *et al.,* 2004).
288 Primary quartz and feldspar grains are rimmed with hematite and goethite (Beitler *et al.,*
289 2005), the sediment is cemented by dolomite (and occasional calcite) and weathered
290 feldspar grains are altered to illite, smectite and kaolinite (Zhu *et al.*, 2006).

291 The Entrada and Navajo Sandstone sampled in the core and in surface outcrops
292 contain zones of open high angle fractures adjacent to the fault, with assemblages of
293 gypsum and pyrite mineralization on the fracture walls (Fig. 6-7). The sandstone units of the
294 middle and lower Entrada Sandstone and the entire sequence of the Navajo Sandstone have
295 been bleached pale white-yellow by dissolution of hematite grain coatings, which normally
296 give these sandstone units a distinctive red colour (Fig. 7). The host rock surrounding high
297 angle fractures are also bleached. The lower portions of siltstone and claystone seals within
298 the Entrada Sandstone and at the base of the Carmel Formation caprock have been
299 bleached by dissolution of hematite grain coatings where they are in contact with the CO_2-
300 rich fluids.

No continuous free gas flow (other than that degassed from the fluid within the well-bore) was observed at the well-head whilst drilling in the Navajo Sandstone, even when the hole was unweighted with drilling mud, suggesting that the drill-hole did not penetrate a free CO_2-gas cap, or at least not a substantial one. Pockets of free CO_2 gas were, however, encountered in the shallower Entrada Sandstone at depths of ~50 mbs and ~140 mbs. The CO_2 gas pockets were identified during tripping out of the rods from the drill-hole, where the gas/fluid ratio in fluid returns to surface would rapidly increase when the base of the rods encountered a zone in the formation containing CO_2-gas.

Across the anticline, the Jurassic Sandstone reservoirs and deeper Carboniferous and Permian strata in the basin are over-pressured, which drives fluid flow from depth through the faults (Fig 8). Shut-in pressures were recorded periodically during drilling. Zero shut-in pressure was observed during drilling through the Entrada Sandstone, Carmel Formation and through much of the upper Navajo Sandstone, suggesting pressure communication between the formations transected by the drill-hole and Crystal Geyser (which as a flowing well acts as a pressure release). Within the basal Navajo Sandstone a maximum shut-in pressure of 13.8 bar was measured at surface at a drill-hole depth of 221 mbs, equivalent to a downhole pressure of 35.5 bar and formation overpressure of 12.8 bar. This shut-in pressure may overestimate the formation pressure due to accumulation of CO_2 gas within the borehole during measurement which elevates the measured pressure at the wellhead. Regional measurements of hydraulic head in wells penetrating the Navajo Sandstone (Hood and Patterson, 1984) imply a local water head of 46m, equivalent to a formation pressure of 26.2 bar and formation overpressure of 3.4 bar.

3.2 Fluid Sampling from Drill-hole CO_2W55

The reactivity of geological fluids primarily depends on their dissolved CO_2 content and pH. The solubility of CO_2 in formation fluids is highly dependent on pressure and temperature, with fluids saturated in CO_2 at formation conditions rapidly degassing CO_2 at the surface. These degassing processes make sampling of high-pressure fluids from CO_2 reservoirs challenging. Accurate measurements of in-situ dissolved CO_2 concentration and pH are crucial for monitoring the progress of CO_2 dissolution and for the prediction of mineral stability and fluid-mineral reactions.

Wireline downhole fluid sampling is the most practical means of repeat sampling of pressurized fluids during borehole drilling. Commercially available wireline fluid samplers include the Leutert Bottom Hole Positive Displacement Sampler (PDS sampler), which has previously been used to recover pressurized fluid samples from deep boreholes and geothermal fields (Fig. 9A; Kietäväinen *et al.,* 2013; Regenspurg *et al.,* 2010). The PDS sampler can be used to recover formation fluid samples (~0.6 L) at reservoir pressure from which dissolved gases can be collected (e.g. Regenspurg *et al.,* 2010) and on which in-situ pH and dissolved CO_2 concentrations can be measured on pressurized samples at surface (Fig. 9B-D).

Both open-hole and downhole fluid samples were collected from drill-hole CO2W55 during drilling. Surface fluid samples were collected from fluid returns to surface and the driller's depth at the time of collection was used to estimate their source depth. Fluid samples were collected from the Entrada Sandstone and Carmel Formation when the drill-hole was at a depth of 98 m and 188 m, respectively. Downhole fluid samples were collected from the Navajo Sandstone at formation pressures using the PDS sampler during the course

of drilling. Four fluid samples (~0.6 L) were collected at depths of 206 m, 224 m, 276 m and 322 m. In order to collect un-degassed and uncontaminated fluids, the PDS sampler was lowered to the base of the hole and: (i) the hole was allowed to flow for 15-45 minutes to flush out the drilling mud using the natural overpressure of the formation, (ii) the hole was shut in to allow pressure recovery for 1-2 hours and (iii) the sampler was then left down hole for 5-6 hours to collect a fluid sample. Full details of the drilling and fluid sampling methods are presented in Kampman *et al.,* 2013a.

3.3 Onsite measurement of dissolved CO_2 and pH

The recovered fluid samples in the downhole sampler were transferred into pre-cleaned high-pressure piston separator sample cylinders at a field laboratory, using a hydraulic transfer pump. Details of pH and dissolved CO_2 concentration measurements on the pressurized fluid samples are presented in Kampman *et al.,* 2013a. Fluid pH and dissolved CO_2 concentrations were measured in the field laboratory using high pressure apparatus (Fig. 9C-D), generally within a few hours of sample collection. An aquilot of the fluid sample was pumped from the piston sample cylinders at pressure through a high-pressure pH rig (Fig 9C; Corr Instruments). The pH probe was calibrated prior to each analysis using pH 3, 4.01, 6 and 7 reference buffer solutions. The pH cell was flushed with formation fluid until a stable pH was attained and the fluid pH recorded.

A second aquilot of sample was pumped at pressure into a 30mL micro piston separator cylinder filled with 15mL of 3M KOH solution (Fig 9D), to capture the dissolved CO_2 in solution by conversion to CO_3^{2-} and precipitation as K_2CO_3 from which total CO_2 concentration could be determined by gran titration. A sample of the exsolved CO_2 gas for analysis of carbon and noble gas isotope ratios was then collected from the piston sample

cylinder by degassing the fluid into evacuated lengths of copper tubing, sealed by cold welding. The remaining fluid was then pumped through 0.2 µm nylon filters and stored in pre-cleaned high-density polyethylene bottles, prewashed with filtrate; one sample acidified to pH 2–3 with 6M HCl and one un-acidified sample for chemical analyses. An aquilot of each sample was prepared and alkalinity was determined immediately by gran titration in the field.

3.4 Sampling of CO_2 Springs

Individual samples were collected from the nine CO_2-springs along the Green River anticline during field seasons in 2006 (Kampman *et al.*, 2009), 2007 and 2010. Fluid Eh, pH and alkalinity were measured in the field using a platinum ORP electrode, field pH meter and by gran titration, respectively. Fluid samples were collected and prepared as above. Samples for gas composition analysis (CO_2, N_2, Ar, O_2 and CH_4) were collected into tubes of annealed copper, flushed with sample gas, and sealed by swage clamps.

3.5 Monitoring and Sampling Crystal Geyser

Prior to drilling of hole CO_2W55, in 2007, a time-series fluid and gas sample set was collected from the build-up to, and during, a short duration (~1.5 hours) large magnitude Type B eruption of Crystal Geyser. A day prior to drilling of hole CO2W55 a Level Logger was installed at a depth of ~5 m in the conduit of Crystal Geyser, to monitor changes in temperature and water level of the geyser during the drilling.

Within a single eruption cycle (SEC; Fig. 10) Crystal Geyser exhibits a bimodal eruption pattern of large eruption events that last between 1-1.5 hours (Type B; Han *et al.,* 2013) and 5-7 hours (Type D; Han *et al.,* 2013) and which occur every 7-10 hours or 20-30 hours, respectively (see also; Gouveia and Friedmann, 2006; Gouveia *et al.,* 2005). Type B and D

eruptions are separated by periods of small frequent low magnitude 'bubbling events' that occur approximately every 15 minutes, termed Type A and C eruptions following the nomenclature of Han *et al.,* (2013) (Fig. 11). Both small and large eruptions are characterised by a drop in pressure and temperature at the mouth of the geyser and the magnitude of this drop is related to the magnitude of the eruption (Han *et al.,* 2013). CO_2-degassing within the geyser conduit is thought to initiate at a depth of ~120m (Assyag *et al.,* 2009). The bimodal pattern of eruptions appears to have evolved through time with eruption durations increasing towards the present (Fig. 11). Only a single Type B eruption was observed during drilling and Type D eruptions were of significantly longer duration (~24 hours) and lower frequency (every ~70 hours) than data previously reported for Crystal Geyser.

3.6 Analytical Geochemistry

The element and isotopic composition of fluids sampled from the drillhole are presented in table 1 and 2, from the CO_2 springs in table 3 and Crystal Geyser in table 5. Major (Na^+, K^+, Ca^{2+}, Mg^{2+}) and minor elements (Al^{3+}, B^{3+}, Ba^{2+}, Fe^{2+}, Li^+, Mn^{2+}, Rb^+, SiO_2, Sr^{2+}) were measured on acidified samples by Varian Vista-PRO simultaneous inductively coupled plasma-atomic emission spectrometry (ICP-AES) at the University of Cambridge following the method given in de Villiers *et al.,* (2002) using a mixed standard with cation proportions specifically designed to match the waters to minimise matrix effects. All samples were analysed in two separate runs with reproducibility within ±2%. Analyses were performed against international water standards T-167, T-143, P35, LGC6019 and ION-20 which reproduce to better than ±6% (2σ) for all elements analysed and often < ±1.0% (2σ; Na^+, K^+, Ca^{2+}, Mg^{2+}, Fe^{2+}, Li^+, Mn^{2+}, SiO_2, Sr^{2+}). Fluid anion (Br^-, F^-, Cl^- and SO_4^{2-}) composition was

415 measured on unacidified samples using a Dionex ICS-3000 Ion Chromotography system at
416 the University of Cambridge. Analyses were performed against international water
417 standards T-167, T-143, P35 and LGC6019 which reproduce to better than ±2% (2σ) for all
418 elements analysed and often <±0.2% (2σ; Br^-, Cl^- and SO_4^{2-}).

419 Analysis of major and minor gases (CO_2, O_2, N_2, Ar, CH_4, H_2S) sampled from the CO_2-
420 springs was carried out at the British Geological Survey, Wallingford by gas chromatography,
421 using a porous polymer column and a flame ionisation detector (Darling and Gooddy, 2006;
422 Table 4). The detection limit of this method is better than 1 part per million by volume
423 (ppmv).

424 3.6.1 Fluid Stable Isotopes

425 The $\delta^{18}O$ and δD of unacidified fluid samples was determined by cavity ringdown
426 spectroscopy using a Picarro L2130-i Analyzer with autosampler injection, in the Godwin
427 Laboratory, University of Cambridge. Each sample was injected nine times into the
428 vaporizer, with the first three results being rejected to avoid memory effects from the
429 previous samples. Values for the final six injections were averaged with in-run precision
430 better than ±0.1‰ for $\delta^{18}O$ and ±0.5‰ for δD (2σ). Sets of six analyses were performed
431 with bracketing internal standards to calibrate the results to V-SMOW and to account for
432 drift. Internal standards were calibrated against V-SMOW, GISP, and SLAP. All results are
433 reported in parts per thousand (‰) relative to V-SMOW. External error was estimated by
434 repeated analysis of internal standards giving ±0.2‰ for $\delta^{18}O$ and ±1‰ for δD (2σ).

435 Sulphur and oxygen isotopes of aqueous sulphate were analysed in the Godwin
436 Laboratory at the University of Cambridge. The $\delta^{34}S_{SO4}$ was determined through combustion
437 in excess oxygen in a Flash EA furnace, coupled by continuous flow to a Delta V Mass
438 spectrometer. The $\delta^{18}O_{SO4}$ was determined through pyrolysis in a TC/EA coupled by

continuous flow to a Delta V Mass Spectrometer. Both samples for sulphur and oxygen isotopes were run with NBS 127 standards bracketing sets of samples (NBS 127 $\delta^{34}S_{SO4}$=20.3‰, NBS127 $\delta^{18}O_{SO4}$=8.6‰). Samples were corrected to NBS127 to account for drift in the mass spectrometer over the course of a run. Data is presented as an average of several replicate measurements with the 2σ standard deviation based on these replicate analyses.

3.6.2 Fluid and mineral Sr-isotopes

Rock samples for detailed analysis were selected from: (i) representative sections of the Navajo Sandstone in the CO2W55 core (sample depths: 227.8 and 259.7m), (ii) gypsum beds from the Carmel Formation in the CO2W55 core and, (iii) outcrop samples of gypsum and calcite veins associated with bleached portions of the exhumed Entrada Sandstone from Salt Wash Graben, studied by Wigley *et al.*, 2012, 2013a 2013b (Table 6). Powdered samples underwent sequential leaching to obtain solutions for Sr-isotopic analysis of gypsum, and the silicate and carbonate fractions of the sandstones. This was supplemented with a single representative sample of Navajo Sandstone, obtained from a CO_2-free drill-hole Blaze #1-C (USGS core repository, Denver, USA. API: 4301930215) located ~25km to the north east of the Green River anticline (Fig. 1). Samples were subjected to a multi-step sequential leaching procedure using: (i) deionized water, (ii) 10% cold acetic acid (to extract the carbonate fraction) and, (iii) 1M cold HCl (to remove any remaining carbonate). A final solution was produced from the silicate residue using HF digestion.

$^{87}Sr/^{86}Sr$ of acidified fluid samples and leachates were determined at the University of Cambridge. Strontium was separated by standard cation exchange methods using Dowex 50W x8, 200-400 mesh resin with the strontium isotopic ratios determined on the Sector 54 VG mass-spectrometer at Cambridge using triple collector dynamic algorithm and

normalised to $^{86}Sr/^{88}Sr$ of 0.1194 using an exponential fractionation correction (Bickle *et al.,* 2003). The internal standard NBS 987 gave 0.710263 +/- 0.000009 (1σ) on 158 separate measurements made during the course of these analyses. Strontium blanks were always less than 250pg and negligible for the Sr concentration of these samples.

3.6.3 Quantitative Mineralogy

A representative suite of samples of the Navajo Sandstone were selected from the CO2W55 core for quantitative mineralogical analysis by XRD at Aachen University (table 7). Rock samples are crushed manually in a mortar. Special care is taken to avoid strain damage. Crushed material is milled with a McCrone Micronising mill (15 minutes) to assure uniform crystallite sizes. Milling is done in ethanol to avoid dissolution of water-soluble components and strain damage to the samples. An internal standard (Corundum, 20 wt.%) is added before milling. All reported mineral compositions relate to the crystalline content of the analysed samples.

Mineral quantification is performed on diffraction patterns from random powder preparates. Sample holders are prepared by means of a side filling method, which minimises preferential orientation. The measurements are done on a Huber MC9300 diffractometer using CoKα-radiation produced at 40 kV and 40 mA. The sample is illuminated trough a fixed divergence slit (1.8 mm, 1.45°), a graphite monochromater and 58 mm, 0.3 mm spacing soller slits. The diffracted beam is measured with a scintillation detector. Counting time is 20 seconds for each step of 0.02° 2θ. Diffractograms are recorded from 2° to 92° 2θ. Quantitative phase analysis is performed by Rietveld refinement. BGMN software is used, with customised clay mineral structure models (Ufer *et al.,* 2008).

4 Results and Discussion

The following sections discuss the results of geochemical measurements on open-hole and downhole fluid samples collected from the CO2W55 drill-hole in 2012. The results are compared to geochemical measurements on fluid samples from the wider CO_2-springs and eruptions of Crystal Geyser. Interpretation of the data is supported by published formation fluid chemistries from CO_2-charged reservoirs in the deeper Permian White Rim Sandstone and Pennsylvanian Paradox Formation obtained during oil exploration drilling on the Green River anticline (Supplementary Table 1; Breit and Skinner, 2002). Element and isotope geochemical profiles and mixing diagrams are used to constrain the sources of fluids in the CO_2 reservoirs and fault, fluid flow, fluid-fluid mixing and fluid-rock reaction in the CO_2-charged sandstones. The results are compared to preliminary petrographic and mineralogical observations from core-samples to constrain the CO_2-promoted fluid-rock reactions.

4.1 CO_2 concentrations, alkalinity and pH in downhole fluid samples

In-situ CO_2 concentrations and fluid pH within the Navajo Sandstone were measured on pressurized downhole fluid samples collected during drilling (Table 1). CO_2 concentrations measured from high pressure samples increase systematically from 511 mmol/L to 927 mmol/L towards the base of the Navajo Sandstone (Fig. 12A-B; Table 1). Fluid pH decreases from 5.3 to 5.1 and alkalinity increases from 51 mmol/L to 64 mmol/L from the top of the formation to the base (Fig. 12A). The measured total dissolved CO_2 concentrations and concentrations estimated from the measured in-situ pH and alkalinity using PHREEQC (Parkhurst and Appelo, 1999) are in good agreement (Fig. 12B). Gradients of the theoretical concentration of CO_2 at saturation in the Navajo Sandstone were calculated using the

equations of Duan *et al.,* (2006) and the measured fluid salinity profile, a temperature profile estimated from a local geothermal gradient of 21.2 ^{o}C/km (Heath *et al.,* 2009), a surface temperature of 12 ^{o}C and a hydrostatic pressure gradient (Fig 12B). The measured CO_2 concentrations at the base of the formation are close to theoretical CO_2 saturation at hydrostatic pressures, and decrease up-wards becoming increasingly undersaturated at shallower depths.

4.2 Gas geochemistry and groundwater redox state

The CO_2-charged groundwaters within the Navajo Sandstone are mildly reducing (Table 3). The Eh of the fluid emanating from the CO_2-springs, measured using a platinum ORP electrode, ranges from ~0mV to ~-50mV. Such Eh measurements are susceptible to incorporation of O_2 in the turbulent spring waters, and these measurements most likely represent an upper bound.

The composition of the gas exsolved from the CO_2-springs (Table 4) is dominated by CO_2 (80.5 to 97.1%), with minor quantities of N_2 (2.27 to 18.1%) and Ar (0.54 to 1.91%), and trace CH_4 (73 to 247 vpm). The redox state of the spring waters was calculated using PHREEQC and the measured CO_2/CH_4 ratio of the exsolved gas, (assuming the fluids are CO_2 saturated at depth and given near quantitatively exsolution of the gas taking into account that ~10% of the CO_2 remains in the fluid when they degas) and this implies a fluid Eh in the range of ~-100 to -150mV, which represents a lower bound.

4.3 Element and isotope geochemistry: Overview

The fluid samples from the Entrada Sandstone and Carmel Formation were collected at surface. The fluid samples from the Navajo Sandstone include both the four samples collected downhole at formation pressure and thirteen samples collected at surface.

Cementation of the drillhole during the course of drilling isolated the Entrada Sandstone and Carmel Formation after they had been sampled, preventing significant contamination of fluids sampled from the Navajo Sandstone with fluids from these shallower reservoirs. Within the Navajo Sandstone, scatter is observed in the open-hole fluid samples collected at surface compared to the downhole samples (Figs. 14-15, 17, 18), probably due to mixing of fluids from different source depths within the well-bore and possible contamination during collection at surface. This is especially apparent for deeper samples from the Navajo, where these fluids are likely mixed with fluids from shallower portions of the formation, as they ascend to surface. Due to this apparent fluid mixing within the wellbore the surface sampled fluids from the Navajo Sandstone are presented but are not used in our interpretation.

The fluid samples collected from the Entrada Sandstone, Carmel formation fracture zone and the detailed profile through the Navajo Sandstone reveal systematic trends in fluid element and isotope geochemistry with depth (Fig. 12-18; Table 1-2). The acidic fluids of the Entrada, Carmel and Navajo formations contain high concentrations of Na, K, Cl, SO_4^{2-} and HCO_3^-, and concentrations of these elements generally increase with depth within the drill-hole (Fig. 13-14). These CO_2-charged Ca-Mg-Na-K-Cl-SO_4^{2-}-HCO_3^- waters share a genetic relationship, which is evident from mixing plots of fluid element and isotope geochemistry (see discussions below). Within the Navajo Sandstone, concentrations of most major (Na, K, HCO_3^-, Cl and SO_4^{2-}) and some minor elements (B, Br, Li, Rb) increase systematically from the top to the base of the formation (Fig 13-14). The observed increase in fluid salinity towards the base of the Navajo formation is accompanied by progressively heavier S-, O- and D-isotopic compositions and increasingly radiogenic $^{87}Sr/^{86}Sr$ ratios (Fig. 15-17).

The gradients in fluid chemistry (B, Br, Li, Rb, Na, K, Cl) and dissolved CO_2 concentrations are shown below to reflect conservative mixing between two components

555 inferred to be: (i) deeply sourced CO_2-saturated brines flowing vertically into the formations
556 from the Little Grand Wash fault and (ii) CO_2-undersaturated fluid dominated by meteoric
557 groundwater flowing horizontally into the fault zone. The dense CO_2-saturated brines
558 introduced along the faults are presumed to flow along the base of the formations, and mix
559 with meteoric fluid. A second suite of elements (Al, Si, Sr, Ca, Mg, Fe and Mn) and the Sr-
560 isotopic compositions of the fluids sampled from the borehole exhibit non-conservative
561 behaviour in the brine endmembers and mixtures. In the sections below, element and
562 isotope mixing diagrams and Sr-isotopic analysis of minerals are combined with
563 mineralogical and petrographic observations and used to show that these components of
564 the fluids are buffered by fluid-rock reactions involving gypsum, carbonate (dolomite and
565 calcite) and hematite.

566 **4.4 Fluid-fluid interactions: brine-meteoric water mixing**

567 Fluid sampled from the drill-hole, Crystal Geyser and the regional CO_2-springs are
568 enriched in halogens (e.g. Cl, Br), sulphate, and alkali and alkaline metals (e.g. Na, K, B, Li,
569 Rb) typical of brines derived from evaporite formations (Fig. 13-14; e.g. Warren, 2010). The
570 Paradox Basin contains thick deposits of evaporites in the Middle Pennsylvanian Paradox
571 Formation and brine-rich aquifers in the Pennsylvanian Hermosa Formation and
572 Mississippian Leadville Limestone (Fig 2; Hanshaw and Hill, 1969; Hite, 1968; Wengerd and
573 Strickland, 1954). Intrusion of brine from these formations into overlying meteoric aquifers
574 occurs in several places across the Paradox Basin (e.g. Spangler *et al.,* 1996 Naftz *et al.,*
575 1997). All the fluids sampled from the drillhole, Crystal Geyser and the wider CO_2 springs
576 plot along arrays in Br/Cl, Li/Cl, B/Cl and Rb/Cl space, with element/Cl ratios consistent with
577 brines derived from the Paradox Formation (Fig 19; brine chemistries from Rosenbauer *et*
578 *al.,* 1991 and the USGS formation water database; Breit and Skinner, 2002). Within the

579 Navajo Sandstone, increasing fluid salinity is accompanied by increasingly heavy $\delta^{18}O$ and
580 δD isotope ratios (Fig. 15), reflecting mixing of isotopically heavy brines from the Paradox
581 formation with isotopically light meteoric groundwater (c.f. Kampman *et al.,* 2009;
582 Wilkinson *et al.,* 2009). In $\delta^{18}O$ and δD space, all fluid samples plot on a two-component
583 mixing array between meteorically derived groundwater, lying on the North American
584 Meteoric water line, and brines from the Carboniferous formations (Fig. 20; Paradox
585 Formation brine stable isotopic composition from Spangler *et al.,* 1996; $\delta^{18}O$ = 2.2‰ and δD
586 = -42‰).

587 Fluid salinity and $\delta^{18}O$ and δD ratios increase in the order Entrada < Carmel < Navajo
588 drill-hole < Crystal Geyser fluid < regional CO_2 springs (Fig. 14-16). The concentrations of Br
589 and Cl (and possibly B, Li and Rb concentrations and $\delta^{18}O$ and δD ratios) appear to act as
590 conservative tracers in these sandstone reservoirs, being little affected by fluid-rock
591 reaction. Some scatter in Br concentrations in the most saline of the springs may reflect
592 variability in the composition of the brine inputs. The brine-meteoric dilution line is
593 preserved in formation fluid samples collected from CO_2-reservoirs in the White Rim
594 Sandstone and Carboniferous strata during oil exploration drilling on the anticline,
595 suggesting mixing of meteoric groundwaters at depth within the basin (Fig. 21-22,
596 Rosenbauer *et al.,* 1991; Breit and Skinner, 2002).

597 The fraction of Carboniferous brine in the CO_2 springs, calculated from the
598 conservative tracers (Cl and Br), exhibits a minimum at Airport Well, where CO_2 enters the
599 Navajo Sandstone without significant inputs of Carboniferous brine, and a maximum of
600 5.14% in the most saline of the regional CO_2 springs. Carboniferous brine inputs increase
601 along fluid flow paths within the Navajo Sandstone parallel to the faults, sampled by the
602 CO_2-springs (Fig. 23). Within the CO2W55 drillhole the brine fraction increases

systematically with depth; the Entrada Sandstone fluid contains 0.55% Carboniferous brine; the Carmel fracture zone fluid contains 0.69% Carboniferous brine and within the Navajo Sandstone the Carboniferous brine fraction increases with depth from 0.71% at the formation top to 1.93% at the base, where fluid enriched in Carboniferous brine flowing in from the fault is sampled. Crystal Geyser contains a maximum of 2.99% Carboniferous brine in the most saline fluid sampled. It is located close to the main fault trace (Fig. 3; ~45m versus 90m for the drill-hole) and it is therefore likely that Crystal Geyser samples more Carboniferous brine enriched fluid within the Navajo Sandstone, before it is diluted with meteoric groundwater during flow away from the fault (where it is then subsequently sampled from the drill-hole).

4.5 Fluid-Rock Reaction

4.5.1 Fluid-rock reactions in Jurassic sandstones: regional and local sandstone bleaching

Dissolution of hematite grain coatings is a common feature within the Jurassic red-bed sandstones of the Paradox Basin and wider geographic region, where it produces spectacular wide-spread zones of sandstone bleaching, which records passage of the bleaching fluid. The bleaching has variously been attributed to reaction with buoyant hydrocarbons and methane rich brines (Beitler *et al.,* 2003, 2005; Chan *et al.,* 2000; Garden *et al.,* 2001; Parry *et al.,* 2004, 2009) and with dense CO_2-charged brines containing methane or sulphide reductants (Loope *et al.,* 2010, 2011; Potter-McIntyre *et al.,* 2013; Wigley *et al.,* 2012, 2013a, 2013b). Such acid-reductive hematite dissolution is possible with a wide range of naturally occurring sources of acidity (e.g. CO_2, organic acids, H_2S) and reductants (e.g. CH_4, HS^-, H_2S) and different combinations most likely act as the bleaching agent in different places. At Green River bleaching of exhumed portions of the red-bed Entrada Sandstone has previously been attributed to the passage of CO_2-charged brines,

627 with minor quantities of dissolved CH_4 (Wigely *et al.,* 2012). The presence of these CO_2-rich
628 brines has been inferred from analysis of CO_2-CH_4 bearing fluid inclusions within secondary
629 mineral phases and from the isotopic composition of secondary carbonate cements
630 associated with the bleaching (Wigley *et al.,* 2012; Wigley *et al.,* 2013b).
631
632 4.5.2 Fluid-rock reactions in the CO2W55 drill-hole
633 The concentrations of Ca, Mg, Sr, Fe, Mn, Si, Al and SO_4, and $^{87}Sr/^{86}Sr$, $\delta^{32}S_{SO42}$ and
634 $\delta^{18}O_{SO42}$ ratios in fluids sampled from the Entrada, Carmel and Navajo formations are
635 decoupled from the simple Carboniferous brine-meteoric groundwater mixing trends (Fig.
636 16-18, 33). The concentrations of these elements are most likely altered by fluid-rock
637 reactions with the primary sources being: dolomite cements within the Navajo Sandstone,
638 dolomite and calcite cements within the Entrada Sandstone, gypsum beds and veins in the
639 Carmel and Entrada formations and hematite and clay grain coatings within the sandstones.
640 Results of sequential leaching for Sr-isotopic composition of the dolomite and silicate
641 fractions of the Navajo Sandstone from the CO2W55 core, and of gypsum beds and veins
642 from the Carmel Formation and Entrada Sandstone are presented in figure 24. Samples of
643 gypsum veins in the Entrada Sandstone from the CO2W55 core were supplemented with
644 samples of gypsum and calcite veins sampled from fracture zones in outcrops of bleached
645 portions of the Entrada Sandstone at Salt Wash Graben (Table 6; Fig. 8, 24). Their Sr-isotopic
646 composition are compared to samples of hematite concretions and calcite veins from
647 bleached portions of the Entrada Sandstone where the bleaching is thought to occur
648 without significant inputs of CO_2 (Fig. 24; Chan *et al.*, 2000).
649 Fluids sampled from the base of the Navajo Sandstone are undersaturated in
650 carbonate (Fig. 25A), hematite (Fig. 25B), feldspar (Fig. 25C-D), clay (Fig. 25C-D), sulphate

(Fig. 25E) and silica (Fig. 25F) minerals. The saturation state of most minerals increases from the base of the formation to the top, with dolomite, hematite, albite, kaolinite, K-feldspar and quartz reaching saturation, or over-saturation at the top of the formation. Similarly elevated mineral saturation states are observed in fluids sampled from the Entrada Sandstone and Carmel Formation (Fig. 25).

Within the Navajo Sandstone fluid sample profile the Ca, Mg, Sr, Fe, Mn, Si and Al concentrations are relatively constant through the formation increasing near the top of the reservoir, close to the contact with the Carmel formation (Fig. 18). The downhole fluid samples from the Navajo Sandstone exhibit changes in Ca, Mg and Sr concentration and Mg/Ca and Sr/Ca ratios that are consistent with the dissolution of dolomite (Fig. 26). Quantitative mineralogy of representative samples from the Navajo Sandstone show that the CO_2-charge reservoir unit is depleted in hematite, calcite and feldspar and enriched in dolomite and clay, compared to a compilation of representative unbleached Navajo Sandstone samples from the wider Paradox Basin (Fig. 27). The dissolution of hematite grain coatings, assemblages of gypsum and pyrite in open fractures and presence of dissolved CH_4 in the reservoir fluids suggests the bleaching reactions may occur through a series of linked reactions involving CO_2 as wells as a range of reduced species following reaction stoichiometries such as:

$$4Fe_2O_3 + 15CO_2 + 6H_2O + CH_4 \rightarrow 8Fe^{2+} + 16HCO_3^- \quad (1)$$

$$Fe_2O_3 + 4CO_2 + H_2O + 2HS^- \rightarrow Fe^{2+} + 4HCO_3^- + FeS_2 \quad (2)$$

674 The fluids contain high concentrations of dissolved sulphate; reduced sulphur species may
675 be present in a meta-stable state, arising from inorganic reduction involving other reduced
676 species or from the activity of sulphur reducing bacteria, commonly present in groundwater
677 systems (e.g. Chapelle *et al.*, 1992). The distribution of dolomite in the core is highly
678 heterogeneous with some areas containing extensive zones of pore-occluding Fe-rich
679 dolomite cements, whilst other areas are free of cement and contain abundant secondary
680 porosity (Fig. 27, 28). The dolomite cements are Fe-rich, complexly zoned and overgrow
681 corroded Fe-poor cores, interpreted to be original early digenetic dolomite cement (Fig 28A-
682 B). The zoned cements contain evidence of variable repeated dissolution and reprecipitation
683 events, with the amount of dissolution-reprecipitation increasing towards the base of the
684 core (Fig. 28C).

685 The Entrada Sandstone fluid is enriched in Ca, Mg, Sr, Fe and SO_4 relative to fluid
686 from the Carmel Formation and Navajo Sandstone, without a corresponding change in
687 conservative ion tracer (Fig. 13, 17, 18). Elevated concentrations of Ca, Mg, Sr and SO_4 and
688 lower $^{87}Sr/^{86}Sr$ ratios in the Entrada Sandstone most likely reflect additions of Sr to the fluid
689 from the dissolution of dolomite and/or calcite and gypsum. High concentrations of Fe in
690 the Entrada Sandstone fluid are in excess of those expected for dissolution of carbonate
691 minerals (Fig. 26) and most likely reflect dissolution of hematite grain coatings present in
692 the Entrada Sandstone. Depressed $^{87}Sr/^{86}Sr$ ratios in the Carmel Formation (Fig. 17) may
693 reflect inputs of low $^{87}Sr/^{86}Sr$ from the dissolution of gypsum beds in-contact with the fluid
694 hosting fracture zone.

695 **4.6 Fluid sources and fluid-fluid mixing during eruptions of Crystal Geyser**

696 Time-series fluid samples collected from Crystal Geyser exhibit a systematic trend in fluid
697 element and isotope geochemistry through the course of an individual eruption (Fig. 29-30).

Changes in fluid geochemistry and temperature coincide with the onset of an eruption and these changes reflect sampling of fluids from different source depths. During the build-up to an eruption the geyser predominantly samples Na-K-Cl-SO_4-HCO_3 enriched fluid from the Navajo Sandstone (Fig 29); as an eruption initiates Ca-Mg-Sr-Fe-Mn enriched fluid is increasingly sampled and this is thought to originate from the Entrada sandstone (Fig 30). These fluid end-members mix within the geyser conduit. This mixing process is evident from element and isotope mixing diagrams, where fluids sampled from the geyser plot along binary mixing arrays between the most saline fluid sampled by the geyser and the Entrada fluid end-member (Fig 31, 32). Increased concentrations of Ca, Mg, Sr, Fe and Mn are accompanied by shifts in the $^{87}Sr/^{86}Sr$ ratio of the fluid as the geyser samples less radiogenic, carbonate enriched waters from the Entrada Sandstone. The compositional trends are accompanied by changes in fluid temperature from ~18.5 °C in the build-up to an eruption, declining to ~16.8 °C during the eruption as inflow of fluid from the shallower cooler Entrada Sandstone reservoir increases (Fig. 12). The proportion of Entrada Sandstone Fluid in the erupted fluids varies from a minimum of ~1-7% during the build-up to an eruption, to a maximum of ~31% during a large Type B eruption.

4.7 Complex fluid-fluid mixing within the reservoirs and fault

In Br versus Cl space the fluids sampled from the drill-hole, springs and geyser plot along a single linear binary mixing line reflecting variable dilution of the Carboniferous brine inputs by meteoric groundwaters (Fig 31A & C). In plots of Sr (or Ca, Mg, Fe and Mn) versus Cl (or Br) the fluids plot on a mixing plane due to inputs to the fluid from mineral dissolution (Fig 31B, 31D-F 32). Below, we discuss mixing phenomena that happen at different spatial scales and result from the mixing of fluids which are themselves already mixtures of Carboniferous brine and meteoric groundwaters; the spatial sampling of fluids within the

722 Navajo Sandtone allows sampling of fluids at different stages of mixing, such that each pair
723 of samples that spatially brackets another sample are 'end-members' to the intermediate
724 mixture. The term end-member is used here to define any pair of fluid samples that bracket
725 an intermediate mixture, and does not necessarily imply that the end-member is a pure
726 fluid (i.e. end-members are also mixtures)

727 The fluids sampled from the drill hole and Crystal Geyser plot on two distinct binary
728 mixing arrays, with one common end-member representing saline CO_2-charged brine from
729 the fault (Fig. 31D-F; Fault Brine). This common end-member (Fault Brine) is estimated as
730 the most saline fluid sampled by Crystal Geyser, which also demarks the intersection of
731 binary mixing lines in Sr-Cl space. Samples taken during the eruption of Crystal Geyser plot
732 along a linear array between a Carboniferous brine-rich end-member (Fault Brine) and an
733 end-member fluid that may be derived from the Entrada Sandstone (Entrada Sandstone
734 Fluid). This end-member is distinctively enriched in Sr, Ca, Mg and Fe, most likely derived
735 from carbonate and hematite dissolution (Fig. 31D-F). Downhole fluid samples from the
736 Navajo Sandstone plot along an array between a Carboniferous brine-rich end-member
737 (Fault Brine; with a slightly less radiogenic Sr-isotopic composition that the saline fluid
738 sampled from Crystal Geyser) and an end-member fluid similar in composition to the
739 fracture zone in the Carmel Formation (Fig. 31D-F; Carmel Fm. Fluid). The fluid sample
740 profile through the Navajo Sandstone contains between ~54% 'Fault Brine' at the base of
741 the formation, decreasing to ~1% at the formation top. These trends and proportions are
742 similarly observed in plots of $^{87}Sr/^{86}Sr$ versus 1/Sr and 1/Cl (Fig. 31). The three 'end-member'
743 fluids 'Fault Brine', 'Entrada Sandstone Fluid' and 'Carmel Fm. Fluid' are themselves
744 mixtures of Carboniferous brine and meteoric groundwater. They also bracket the
745 intermediate mixtures of fluids sampled within the Navajo Sandstone and from Crystal

746 Geyser. It is likely that fluids within the Entrada Sandstone and Carmel fracture zone will
747 have a range of compositions, but as only two samples were collected, they are treated as
748 representative of the fluids present in these formations, which likely have a range in
749 compositions.

750 The validity of these mixing models can be tested by using the mixing arrays defined
751 by fluid sampled from Crystal Geyser and the downhole fluids sampled from the Navajo
752 Sandstone to estimate the solute chemistry of the end-member fluids. The solute chemistry
753 of the end-member fluids can be estimated from the mixture compositions and their
754 element/Cl ratios, and the measured Cl concentrations of the inferred end-members. The
755 results are presented in table 8 and show that the mixing models generally predict the
756 solute chemistry of the end-members within ±10-15% for most elements, with Fe being a
757 notable exception, and better than <±5% for many. The model predicts the composition of
758 the Entrada end-member reasonably well, which relies on the array defined by fluids
759 sampled from Crystal Geyser; this mixing happens quickly within the conduit of Crystal
760 Geyser, and is thus less susceptible to modification by fluid-rock reaction. The model is less
761 able to predict certain elements (notably Ca, Mg, Sr, Fe Mn, and HCO_3) in the Fault Brine and
762 Carmel Formation end-member compositions, estimated from the mixing array defined by
763 the downhole Navajo fluid samples, possibly because fluid mixing and fluid flow rates here
764 are slow, relative to the rates of potential fluid rock reactions involving carbonate and Fe-
765 oxide minerals.

766 Within the Navajo Sandstone Sr concentrations and $^{87}Sr/^{86}Sr$ ratios increase
767 systematically with depth, becoming increasingly radiogenic towards the base of the
768 formation and as salinity increases, to a maximum $^{87}Sr/^{86}Sr$ ratio of 0.71213 (Fig 17; 31E-F).
769 In fluids sampled by Crystal Geyser, Sr concentrations and $^{87}Sr/^{86}Sr$ ratios increase as

770 salinity, and brine fraction of the sampled fluid increases, to a maximum $^{87}Sr/^{86}Sr$ ratios of
771 0.712726, in the most saline fluid sampled (Fig 31E-F). Carboniferous age brines from the
772 Paradox Basin typically have non-radiogenic $^{87}Sr/^{86}Sr$ ratios, close to Pennsylvanian or
773 Mississippian seawater (e.g. Fig 24-25; 0.70845 to 0.70864; Spangler *et al.,* 1996 Naftz *et al.,*
774 1997). The radiogenic $^{87}Sr/^{86}Sr$ ratio of the CO_2-charged brines flowing into the Navajo
775 Sandstone from the fault reflects addition of radiogenic Sr from silicate mineral dissolution
776 reactions during migration of the CO_2-charged brines from depth.

777 Sr concentration and Sr-isotope gradients in the Navajo Sandstone reflect a
778 combination of fluid-rock reaction and fluid-fluid mixing trends between Sr-rich radiogenic
779 CO_2-saturated brines flowing in from the faults, low $^{87}Sr/^{86}Sr$ meteoric enriched fluids
780 flowing laterally into the fault zone and low $^{87}Sr/^{86}Sr$ fluids descending from the fracture
781 zone in the Carmel Formation. These mixing plots suggest that within the Navajo Sandstone:
782 (i) the most saline fluids sampled from the drillhole is derived from dilution of a
783 Carboniferous brine rich fluid comparable to fluid sampled by Crystal Geyser, and presumed
784 to be input along the base of the formation from the fault, (ii) that this brine-rich fluid mixes
785 with CO_2-charged, but brine-poor, fluid flowing parallel to the fault, similar to that sampled
786 earlier on the flow path by Airport Well, (iii) this mixture then flows through fractures into
787 the overlying Carmel Formation caprock.

788 This interpretation is supported by data on the isotopic composition of SO_4^{2-} in these
789 fluids, which reflect sequential dilution of fluid enriched in isotopically heavy sulphate with
790 an isotopically light sulphate-rich fluid flowing horizontally into the fault zone, which then
791 flows upwards through fractures in the Carmel Formation caprock (Fig. 33). A conceptual
792 model illustrating the overall patterns of fluid flow and fluid-fluid mixing with in the fault
793 and region surrounding the drill-hole is presented in figure 34.

4.8 Estimating dissolved CO_2 concentration in end-member fluids

Cross plots of the fraction of end-member fluids in downhole fluid samples from the Navajo Sandstone versus their measured DIC form linear arrays from which the total DIC of end-member fluids can be estimated (presented in Fig. 35). The inflowing Carboniferous brine from the fault and Carmel Formation fluid end-members have estimated DIC concentrations of 1.37 mol/L and 0.56 mol/L respectively, of which 1.30 mol/L and 0.50 mol/L are dissolved CO_2, the remainder being HCO_3^-. The estimated CO_2 concentration of fluid flowing into the Navajo Sandstone from the fault is higher than the average theoretical CO_2 saturation (~1.08 mol/L) at formation temperature and fluid pressure for fluid within the Navajo Sandstone, at the site of Crystal Geyser. This suggests that the brine end-member may be degassing as it decompresses within the fault zone. The estimate of the theoretical CO_2 solubility was calculated using the equations of Duan et al. (2006), using the fluid composition of the fault brine end-member, a geothermal gradient of 21.2^oC/km and a hydrostatic pressure gradient. The theoretical CO_2 saturation for fluid from within the Carmel fracture zone is 0.68 mol/L, and the estimated CO_2 concentration corrected for alkalinity is 0.50 mol/L, suggesting the fluid sampled from the fracture zone maybe CO_2-undersaturated.

4.9 Estimating CO_2 dissolution during CO_2 and CO_2-charged brine migration from the deep supercritical reservoirs

The shallow Jurassic Entrada (0.55% Carboniferous brine) and Navajo Sandstones (1.93% Carboniferous brine) and the deeper Permian White Rim Sandstone reservoirs (10.73% Carboniferous brine) are fed by flow of CO_2-saturated brines from deep supercritical CO_2-charged Carboniferous reservoirs (Fig. 2, 21). The dissolved CO_2 concentrations in brines of the deeper Permian White Rim Sandstone and Carboniferous formations can be estimated

from the CO_2-solubility equations of Duan *et al.,* 2006 and the known salinity, pressure and temperature gradients through the basin (Fig 21); the theoretical saturated CO_2 concentrations in the White Rim Sandstone and Carboniferous formations are ~1.3 mol/L and ~0.4-0.8 mol/L, respectively. The migrating Carboniferous brines undergo substantial dilution with meteoric groundwaters in the shallow reservoirs and fault; this would lead to a concomitant dilution of the dissolved CO_2 concentration of the brines. The amount of dissolved CO_2 in the Permian and Jurassic sandstone reservoirs, that originates as a dissolved phase in the CO_2-charged Carboniferous brines, can be estimated from the CO_2/Cl of the Carboniferous brine (0.42:4.2 moles/L) and the measured or estimated CO_2/Cl ratios of the sandstone formation fluids (White Rim: 1.32:0.45 moles/L and Navajo: 0.93:0.08 moles/L). The Carboniferous brine-meteoric groundwater dilution factors imply that >~99% of the CO_2 in fluids sampled from the Navajo Sandstone is derived after the fluids have migrated from the Carboniferous reservoirs, with ~75% of the dissolved load being acquired during migration from the White Rim Sandstone to the Navajo Sandstone. This implies that: (i) both free phase CO_2 and brine co-migrate from the deep Carboniferous reservoirs, (ii) that brine-meteoric water mixing in the vicinity of the fault zone is an effective means of dissolving this migrating CO_2 and, (iii) that such fluid-fluid interactions can efficiently retard the migration of free phase CO_2 to the surface. A significant fraction of the CO_2-migrating from the deeper Carboniferous reservoir is then likely transported away from the faults by regional groundwater flow (e.g. Bickle and Kampman, 2013).

5 Conclusions

For the first time core and pressurized downhole fluid samples have been obtained from a natural CO_2 reservoir and caprock. The CO2W55 drill-hole transected a series of CO_2-

charged reservoirs within the Jurassic Entrada and Navajo Sandstones, and a CO_2-charged fracture zone in the Carmel Formation caprock. Fluid geochemistry and analysis of in-situ pH and CO_2 concentrations, using pressurized fluid sampling whilst drilling, shows that the reservoirs are being fed by active inflow of CO_2-saturated brines from the faults, originally derived from reservoirs of supercritical CO_2 in Carboniferous strata at depths of >2km. The evidence for CO_2-saturated fluids at the base of the Navajo requires that a mixture of Carboniferous brine and free-phase CO_2 must be introduced from the fault zone. The absence of a free CO_2 gas cap within the Navajo Sandstone requires that this gas is effectively dissolved and dissipated in the Navajo Sandstone formation fluids. Pockets of free CO_2-gas were encountered in the shallow Entrada Sandstone, suggesting that the CO_2-saturated fluids degas within the fault and shallow reservoirs above the base of the Navajo Sandstone, and that this free CO_2 gas is the source of the surface CO_2 flux. Comparison of the sampled fluid geochemistry to analyses of brine compositions from the deep White Rim Sandstone and Carboniferous CO_2 reservoirs suggests that: (i) CO_2 and CO_2-charged brines co-migrated from the deep reservoirs, (ii) the CO_2-saturated brines migrating from depth interact with significant volumes of meteoric groundwater in aquifers in the shallower Permian and Jurassic sandstones, diluting the brine composition, and (iii) that a significant fraction of the CO_2 migrating from depth is dissolved in these migrating brine-meteoric water mixtures, with >99% of the CO_2 in fluids sampled from the Navajo Sandstone being derived during fluid migration, after the fluids left their source reservoir. The $^{87}Sr/^{86}Sr$ ratio of the inflowing brine is significantly elevated for ratios expected for Sr in Carboniferous brines, requiring significant fluid-rock reaction and addition of radiogenic Sr from silicate mineral dissolution, during fluid migration.

Element and isotope geochemistry of fluid samples from the drillhole and Crystal Geyser constrain mixing models which show that within the Navajo Sandstone the reservoir fluids are undergoing complex mixing of: (i) CO_2-saturated Carboniferous brine inflowing from the fault, (ii) CO_2-undersaturated meteoric groundwater flowing through the reservoir and (iii) reacted CO_2-charged brines flow through fracture zones into the formations above. Element and isotope geochemistry of time-series fluid samples from Crystal Geyser reveals that the geyser is fed by fluids from both the Entrada and Navajo Sandstones. Onset of a large-scale eruption coincides with a change in this fluid source. Whether the change in fluid source is a response or a trigger for the onset of the eruptions is not known.

CO_2-charged fluids flowing through the Navajo Sandstone both dissolve and precipitate dolomite at different spatial and temporal scales. CO_2-charged fluids flowing through the Entrada Sandstone dissolve dolomite, calcite, gypsum and hematite. The hematite content of the Navajo and Entrada Sandstones is significantly reduced where they are in contact with the CO_2-charged fluids, bleaching it from red to pale white. This suggests that the CO_2-charged brines have dissolved the hematite grain coatings originally present in the sediment, supporting interpretations from elsewhere that CO_2-charged brines with CH_4 or H_2S reductants can cause sandstone bleaching.

The results of this study highlight the important potential retentive capacity of the geological overburden above deep CO_2 reservoirs, for retarding CO_2 migration to the surface. This capacity is site specific and future CO_2 storage programs should include a study of the formations overlying the target reservoir including the hydrodynamics, permeability and fluid geochemistry of overlying aquifers, in order to understand the likely migration pathways of leaking CO_2-charged fluids and the trapping potential of the geological overburden.

6 Acknowledgments

We would like to thank all those who helped during the drilling program in particular Chris Delahunty, the rest of the DOSECC drilling team, Don Hamilton from Starpoint, Karen Silliman, and the core loggers from Utah State University; Brady Utley, Digant Yvas and Nathan Giles. Gas composition analyses were performed by George Darling at BGS Wallingford. Carbon storage research at Cambridge, Oxford and the British Geological Survey is supported by the UK Department of Energy and Climate Change through the Carbon Capture and Storage research and development programme and Natural Environment Research Council grants NE/F004699/1, NE/F002823/1 and NEF002645/1. Niko Kampman, Pieter Bertier and Utah State University acknowledges financial support from Shell Global Solutions International. GP and CAR publish with the permission of the Executive Director of the British Geological Survey, NERC.

7 References

Allis, R., Chidsey, T., Gwynn, W., Morgan, C., White, S., Adams, M. and Moore, J., 2005. Implications of results from CO_2 flux surveys over known CO_2 systems for long-term monitoring. United States Geological Survey.

Allis, R., Bergfeld, D., Moore, J., McClure, K., Morgan, C., Chidsey, T., Heath, J. and McPherson, B., 2001. Natural CO_2 Reservoirs on the Colorado Plateau and Southern Rocky Mountains: Candidates for CO_2 Sequestration. Proc. nat. conf. on carbon sequestration.

Apps, J.A., Zheng, L., Zhang, Y., Xu, T., Birkholzer, J.T., 2010. Evaluation of Potential Changes in Groundwater Quality in Response to CO_2 Leakage from Deep Geologic Storage. Transport in Porous Media, 82(1): 215-246.

Assayag, N., Bickle, M., Kampman, N., Becker, J., 2009. Carbon isotopic constraints on CO_2 degassing in cold-water Geysers, Green River, Utah. Energy Procedia, 1(1): 2361-2366.

Baer, J.L., Rigby, J.K., 1978. Geology of the Crystal Geyser and environmental implications of its effluent, Grand County, Utah. Utah Geology, 5(2).

Bickle, M., 2009. Geological carbon storage. Nature Geoscience, 2(12): 815-818.

Bickle, M., & Kampman, N., 2013. Lessons in carbon storage from geological analogues. Geology, 41(4), 525-526.

Bickle, M., Kampman, N., Wigley, M., 2013. Geochemistry of CO_2 sequestration: Natural Analogues. Rev Mineral Geochem, 77, in press

Blakey, R. C., Havholm, K. G., & Jones, L. S., 1996. Stratigraphic analysis of eolian interactions with marine and fluvial deposits, Middle Jurassic Page Sandstone and Carmel Formation, Colorado Plateau, USA. Journal of Sedimentary Research, 66(2), 324-342.

Breit, G. N., and Skinner, C.C., 2002. Produced Waters Database: U.S. Geological Survey Provisional Release, May 2002

Burnside, N., Shipton, Z., Dockrill, B., Ellam, R.M., 2013. Man-made versus natural CO_2 leakage: A 400 k.y. history of an analogue for engineered geological storage of CO_2. Geology.

Chan, M.A., Parry, W., Bowman, J., 2000. Diagenetic hematite and manganese oxides and fault-related fluid flow in Jurassic sandstones, southeastern Utah. AAPG bulletin, 84(9): 1281-1310.

Chapelle, F. H., & Lovley, D. R., 1992. Competitive Exclusion of Sulfate Reduction by Fe (lll)-Reducing Bacteria: A Mechanism for Producing Discrete Zones of High-Iron Ground Water. Ground water, 30(1), 29-36.

Condon, S. M., & Huffman, A. C., 1997. Geology of the Pennsylvanian and Permian cutler group and Permian Kaibab limestone in the Paradox Basin, southeastern Utah and southwestern Colorado. US Government Printing Office.

Cooley, M.E., Harshbarger, J.W., Akers, J.P., Hardt, W.F., 1969. Regional hydrology of the Navajo and Hopi Indian Reservations, Arizona, New Mexico, and Utah. U.S. U.S. Geol. Surv. Prof. Paper 521-A, 61 pp.

Crabaugh, M., & Kocurek, G. (1993). Entrada Sandstone: an example of a wet aeolian system. Geological Society, London, Special Publications, 72(1), 103-126.

de Villiers, S., Greaves, M., & Elderfield, H., 2002. An intensity ratio calibration method for the accurate determination of Mg/Ca and Sr/Ca of marine carbonates by ICP-AES. Geochemistry, Geophysics, Geosystems, 3(1).

Dockrill, B., Shipton, Z.K., 2010. Structural controls on leakage from a natural CO_2 geologic storage site: Central Utah, U.S.A. Journal of Structural Geology, 32(11): 1768-1782.

Doelling, H., 1994. Tufa deposits in western Grand County. Utah Geological Survey, 26(2-3): 8-10.

Doelling, H.H., 2001. Geologic map of the Moab and Eastern Part of the San Rafael Desert 30′ ×60′ quadrangles, Grand and Emery counties, Utah and Mesa county, Colorado. Geologic map 180: Utah Geological Survey Geologic Map 180, scale 1:100,000.

Doughty, C., & Myer, L. R., 2009. Scoping calculations on leakage of CO_2 in geologic storage: The impact of overburden permeability, phase trapping, and dissolution. Geophysical Monograph Series, 183, 217-237.

Duan, Z., Sun, R., Zhu, C., Chou, I., 2006. An improved model for the calculation of CO_2 solubility in aqueous solutions containing Na^+, K^+, Ca^{2+}, Mg^{2+}, Cl^-, and SO_4^{2-}. Marine Chemistry, 98(2-4): 131-139.

Dubacq, B., Kampman, N., Assayag, N., Wigley, M., Bickle, M., 2011. CO_2 Degassing and Groundwater Mixing in the Navajo Aquifer, Green River, Utah. Mineralogical Magazine, 75(3): 786.

Embid, E., Crossey, L., 2009. U-series dating, geochemistry, and geomorphic studies of travertines and springs of the Springerville area, east-central Arizona, and tectonic implications, PhD Thesis, University of New Mexico, Albuquerque.

966 Gilfillan, S. M. V., Lollar, B. S., Holland, G., Blagburn, D., Stevens, S., Schoell, M., Cassidy, M.,
967 Ding, Z., Zhou Z., Lacrampe-Couloume, G. and Ballentine, C. J., 2009. Solubility
968 trapping in formation water as dominant CO_2 sink in natural gas fields. Nature,
969 458(7238): 614–618.
970 Gilfillan, S., Wilkinson M., Haszeldine R.S., Shipton Z.K., Nelson S.T., Poreda R.J., 2011. He
971 and Ne as tracers of natural CO_2 migration up a fault from a deep reservoir.
972 International Journal of Greenhouse Gas Control 5: 1507-1516
973 Goldstein, H. L., Reynolds, R. L., Reheis, M. C., Yount, J. C., & Neff, J. C., 2008. Compositional
974 trends in aeolian dust along a transect across the southwestern United States.
975 Journal of Geophysical Research: Earth Surface (2003–2012), 113(F2).
976 Darling, W. G., & Gooddy, D. C., 2006. The hydrogeochemistry of methane: Evidence from
977 English groundwaters. Chemical Geology, 229(4), 293-312.
978 Gouveia, F., Friedmann, S., 2006. Timing and prediction of CO_2 eruptions from Crystal
979 Geyser, UT. United States. Dept. of Energy.
980 Gouveia, F., Johnson, M., Leif, R., Friedmann, S., 2005. Aerometric measurement and
981 modeling of the mass of CO_2 emissions from Crystal Geyser, Utah. UCRL-TR-211870,
982 Lawrence Livermore National Lab., Livermore, CA (USA).
983 Han, W. S., Lu, M., McPherson, B. J., Keating, E. H., Moore, J., Park, E., Watson, Z. T. and
984 Jung, N.-H., 2013. Characteristics of CO_2-driven cold-water geyser, Crystal Geyser in
985 Utah: experimental observation and mechanism analyses. Geofluids, 13(3); 283–297.
986 Hanshaw, B. B., & Hill, G. A., 1969. Geochemistry and hydrodynamics of the Paradox basin
987 region, Utah, Colorado and New Mexico. Chemical Geology, 4(1), 263-294.
988 Harshbarger, J.W., Repenning, C.A., Irwin J.H., 1957. Stratigraphy of the Uppermost Triassic
989 and the Jurassic Rocks of the Navajo Country. U.S. Geol. Surv. Prof. Paper 291, 71 p.
990 Heath, J., 2004. Hydrogeochemical Characterization of Leaking Carbon Dioxide-Charged
991 Fault Zones in East-Central Utah, Utah State University, USA.
992 Heath, J. E., Lachmar, T. E., Evans, J. P., Kolesar, P. T., & Williams, A. P. (2009).
993 Hydrogeochemical Characterization of Leaking, Carbon Dioxide-Charged Fault Zones
994 in East-Central Utah, With Implications for Geologic Carbon Storage. Carbon
995 Sequestration and Its Role in the Global Carbon Cycle, 147-158.
996 Hintze, L. F., 1993. Geologic history of Utah: Brigham Young University Geology Studies,
997 Special Publication 7, 202 p. Reprinted with minor revisions July.
998 Hite, R. J., 1968. Salt deposits of the Paradox Basin, southeast Utah and southwest Colorado.
999 Geological Society of America Special Papers, 88, 319-330.
1000 Hood, J., Patterson, D., 1984. Bedrock aquifers in the northern San Rafael Swell area. Utah,
1001 with special emphasis on the Navajo Sandstone. State of Utah Department of
1002 Natural Resources Technical Publication, 78(128).
1003 Hovorka, S. D., Benson, S. M., Doughty, C., Freifeld, B. M., Sakurai, S., Daley, T. M., Kharaka,
1004 Y.K., Holtz, M., Trautz, R.C., Nance, S., Myer, L.R., Knauss, K.G., 2006. Measuring
1005 permanence of CO_2 storage in saline formations: the Frio experiment. Environmental
1006 Geosciences, 13(2): 105.
1007 Kampman, N., Bickle, M., Becker, J., Assayag, N., Chapman, H., 2009. Feldspar dissolution
1008 kinetics and Gibbs free energy dependence in a CO_2-enriched groundwater system,
1009 Green River, Utah. Earth and Planetary Science Letters, 284(3-4): 473-488.
1010 Kampman, N., Burnside, N. M., Shipton, Z. K., Chapman, H. J., Nicholl, J. A., Ellam, R. M., and
1011 Bickle, M. J., 2012. Pulses of carbon dioxide emissions from intracrustal faults
1012 following climatic warming. Nature Geoscience, 5(5): 352-358.

1013 Kampman, N., Maskell, A., Bickle, M.J., Evans, J.P., Schaller, M., Purser, G., Zhou, Z.,
1014 Gattacceca, J., Peitre, E.S., Rochelle, C.A., Ballentine, C.J., Busch A., & scientists of the
1015 GRDP, 2013a. Scientific drilling and downhole fluid sampling of a natural CO_2
1016 reservoir, Green River, Utah. Scientific Drilling, 1: 1-11.
1017 Kampman, N., Bickle, M., Wigley, M., Dubacq, B., 2013b. Fluid flow and CO_2-fluid-mineral
1018 interactions during CO_2-storage in sedimentary basins. Chemical Geology Reviews,
1019 this issue
1020 Keating, E. H., Fessenden, J., Kanjorski, N., Koning, D. J., & Pawar, R., 2010. The impact of
1021 CO_2 on shallow groundwater chemistry: observations at a natural analog site and
1022 implications for carbon sequestration. Environmental Earth Sciences, 60(3), 521-536.
1023 Keating, E. H., Newell, D. L., Viswanathan, H., Carey, J. W., Zyvoloski, G., & Pawar, R., 2012.
1024 CO_2/Brine Transport into Shallow Aquifers along Fault Zones. Environmental science
1025 & technology, 47(1), 290-297.
1026 Keating, E. H., Alexandra Hakala, J., Viswanathan, H., William Carey, J., Pawar, R., Guthrie, G.
1027 D., & Fessenden-Rahn, J., 2013. CO_2 leakage senarios: simulations informed by
1028 observations at a natural analog site. Applied Geochemistry, 30, 136-147.
1029 Kharaka, Y. K., Cole, D. R., Hovorka, S. D., Gunter, W. D., Knauss, K. G., Freifeld, B. M., 2006.
1030 Gas-water-rock interactions in Frio Formation following CO_2 injection: Implications
1031 for the storage of greenhouse gases in sedimentary basins. Geology, 34(7), 577-580.
1032 Kharaka, Y. K., Thordsen, J. J., Kakouros, E., Ambats, G., Herkelrath, W. N., Beers, S. R.,
1033 Gullickson, K. S., 2010. Changes in the chemistry of shallow groundwater related to
1034 the 2008 injection of CO_2 at the ZERT field site, Bozeman, Montana. Environmental
1035 Earth Sciences, 60(2), 273-284.
1036 Little, M. G., & Jackson, R. B., 2010. Potential impacts of leakage from deep CO_2
1037 geosequestration on overlying freshwater aquifers. Environmental science &
1038 technology, 44(23), 9225-9232.
1039 Loope, D.B., Kettler, R.M., Weber, K.A., 2010. Follow the water: Connecting a CO_2 reservoir
1040 and bleached sandstone to iron-rich concretions in the Navajo Sandstone of south-
1041 central Utah, USA. Geology, 38(11): 999-1002.
1042 Loope, D. B., Kettler, R. M., & Weber, K. A., 2011. Morphologic Clues to the Origins of Iron
1043 Oxide–Cemented Spheroids, Boxworks, and Pipelike Concretions, Navajo Sandstone
1044 of South-Central Utah, USA. The Journal of Geology, 119(5), 505-520.
1045 Mayo, A.L., Nielsen, P.J., Loucks, M., Brimhall, W.H., 1992. The Use of Solute and Isotopic
1046 Chemistry to Identify Flow Patterns and Factors Which Limit Acid Mine Drainage in
1047 the Wasatch Range, Utah. Ground Water, 30(2): 243-249.
1048 Naftz, D., Peterman, Z., Spangler, L., 1997. Using δ^{87}Sr values to identify sources of salinity to
1049 a freshwater aquifer, Greater Aneth Oil Field, Utah, USA. Chemical Geology, 141(3):
1050 195-209.
1051 Nuccio, V., Condon, S., 1996. Burial and thermal history of the Paradox Basin, Utah and
1052 Colorado, and petroleum potential of the Middle Pennsylvanian Paradox Formation.
1053 US Government Print. Office.
1054 Oldenburg, C. M., & Rinaldi, A. P., 2011. Buoyancy effects on upward brine displacement
1055 caused by CO_2 injection. Transport in porous media, 87(2), 525-540.
1056 Parkhurst, D.L., Appelo, C.A.J., 1999. User's Guide to Phreeqc (version 2)–A Computer
1057 Program for Speciation, Batch-Reaction, One-Dimensional Transport, and Inverse
1058 Geochemical Calculations. US Department of the Interior. US Geological Survey,
1059 Denver.

Parry, W.T., Chan, M.A., Beitler, B., 2004. Chemical bleaching indicates episodes of fluid flow in deformation bands in sandstone. AAPG Bull. 88, 175–191.

Parry, W. T., Chan, M. A., & Nash, B. P., 2009. Diagenetic characteristics of the Jurassic Navajo Sandstone in the Covenant oil field, central Utah thrust belt. AAPG bulletin, 93(8), 1039-1061.

Pasala, S.M., Forster, C.B., Deo, M., Evans, J.P., 2013. Simulation of the impact of faults on CO_2 injection into sandstone reservoirs. Geofluids, 13(3): 344-358.

Peterson, F., Turner-Peterson, C., 1989. Geology of the Colorado Plateau: Grand Junction to Denver, Colorado June 30–July 7, 1989, 130. American Geophysical Union.

Potter-McIntyre, S., Allen, J., Chan, M., Shik Han, W., Lee, S.-Y. and McPherson, B., 2013. Iron precipitation in a natural CO_2 reservoir: Jurassic Navajo Sandstone in the northern San Rafael Swell, UT, USA. Geofluids.

Rosenbauer, R., Bischoff, J.L., Kharaka, Y.K., 1991. Geochemical effects of deep-well injection of the Paradox Valley brine into Paleozoic carbonate rocks, Colorado, U.S.A. Applied Geochemistry, 7: 273-286.

Shipton, Z. K., Evans, J. P., Kirschner, D., Kolesar, P. T., Williams, A. P., & Heath, J., 2005. Natural leaking CO_2-charged systems as analogs for failed geologic storage reservoirs. The CO_2 Capture and Storage Project (CCP).

Shipton, Z. K., Evans, J. P., Dockrill, B., Heath, J., Williams, A., Kirchner, D., & Kolesar, P. T., 2004. Analysis of CO_2 leakage through 'low-permeability' faults from natural reservoirs in the Colorado Plateau, east-central Utah. Geological Society London Special Publications, 233(43).

Spangler, L., Naftz, D., Peterman, Z., 1996. Hydrology, chemical quality, and characterization of salinity in the Navajo aquifer in and near the Greater Aneth oil field. San Juan County, Utah. US Geo. Survey Water-Res. Inv. Report 96-4155.

Trautz, R. C., Pugh, J. D., Varadharajan, C., Zheng, L., Bianchi, M., Nico, P. S., Birkholzer, J. T., 2012. Effect of Dissolved CO_2 on a Shallow Groundwater System: A Controlled Release Field Experiment. Environmental Science & Technology, 47(1): 298-305.

Truini, M., & Longsworth, S. A., 2003. Hydrogeology of the D aquifer and movement and ages of ground water determined from geochemical and isotopic analyses, Black Mesa area, northeastern Arizona. US Department of the Interior, US Geological Survey.

Trimble, L. M., & Doelling, H. H., 1978. The geology and uranium vanadium deposits of the San Rafael River mining area, Emery County, Utah. Utah Geological Survey.

Ufer, K., Stanjek, H., Roth, G., Dohrmann, R., Kleeberg, R., & Kaufhold, S., 2008. Quantitative phase analysis of bentonites by the Rietveld method. Clays and Clay Minerals, 56(2), 272-282.

Verlander, J. E., 1995. The Navajo Sandstone. Geology Today, 11(4), 143-146.

Vrolijk. P., Myers, R., Sweet, M.L., Shipton, Z.K., Dockrill, B., Evans, J.P., Heath J., Williams A. 2005. Anatomy of reservoir-scale normal faults in central Utah: stratigraphic controls and implications for fault zone evolution and fluid flow. In: Pederson, J. and Dehler, C.M. (eds.) Interior Western United States: Geological Society of America Field Guide, v. 6, p. 261-282.

Warren, J.K., 2010. Evaporites through time: Tectonic, climatic and eustatic controls in marine and nonmarine deposits. Earth-Science Reviews, 98(3): 217-268.

Wengerd, S. A., & Strickland, J. W., 1954. Pennsylvanian stratigraphy of Paradox salt basin, Four Corners region, Colorado and Utah. AAPG Bulletin, 38(10), 2157-2199.

Wigley, M., Kampman, N., Dubacq, B., Bickle, M., 2012. Fluid-mineral reactions and trace metal mobilization in an exhumed natural CO_2 reservoir, Green River, Utah. Geology, 40(6): 555-558.

Wigley, M., Dubacq, B., Kampman, N., Bickle, M., 2013a. Controls of sluggish, CO_2-promoted, hematite and K-feldspar dissolution kinetics in sandstones. Earth and Planetary Science Letters, 362: 76-87.

Wigley, M., Kampman, N., Chapman, H., Dubacq, B., Bickle, M., 2013b. In-situ re-deposition of trace metals mobilized by CO_2-charged brines. Geochemistry, Geophysics, Geosystems.

Wilkinson, M., Gilfillan, S.V.M., Haszeldine, R.S., Ballentine, C.J., 2009. Plumbing the depths: Testing natural tracers of subsurface CO_2 origin and migration, Utah. In: Grobe, M., Pashin, J.C., Dodge, R.L. (Eds.), Carbon dioxide sequestration in geological media — State of the science. AAPG Studies in Geology, pp. 619-634.

Zhou, Q., Birkholzer, J. T., Mehnert, E., Lin, Y. F., & Zhang, K., 2010. Modeling basin-and plume-scale processes of CO_2 storage for full-scale deployment. Ground Water, 48(4), 494-514.

Zhu, C., Veblen, D.R., Blum, A.E., Chipera, S.J., 2006. Naturally weathered feldspar surfaces in the Navajo Sandstone aquifer, Black Mesa, Arizona: Electron microscopic characterization. Geochim. Cosmochim. Acta 70, 4600-4616.

Figure 1 Geological features of the Paradox Basin and surrounding region. (a) Structural provinces of the Paradox Basin and bordering uplifts (redrawn after Condon, 1997). (b) Main structural features of the Northern Paradox Basin, in the vicinity of the study area. The outlined area in grey is the maximum extent of the Pennsylvanian evaporite formations which demarks the extent of the Paradox Basin. Yellow stars denote the locations of CO_2-charged springs or regions of dry CO_2 exhalations.

Figure 2 Generalized stratigraphic section for the Green River area. Thickness data compiled from Trimble and Doelling (1978) and Hintze (1993). Hydrological data from Hanshaw and Hill (1969) and Hood and Patterson (1984).

Figure 3 Geological map of the Green River anticline showing locations of the Little Grand Wash and Salt Wash Graben normal fault systems, CO_2-springs and location of drill-hole CO2W55 (base map redrawn after Doelling, 2001 & Kampman *et al.,* 2009). The distribution of ancient travertine mounds along the faults is highlighted, reflecting sites of paleo-CO_2 leakage (drawn from maps in Dockrill and Shipton, 2010). Structure contours are the height of the top surface of the Navajo Sandstone above sea level, the main shallow CO_2 bearing reservoir. Groundwater flow trajectories in the Navajo Sandstone are also shown (after Hood and Patterson, 1984 and maps in Kampman *et al.,* 2009). Meteoric fluid flows from recharge zones in the San Rafael Swell to the north-west to zones of discharge in the Green River. The CO_2 and CO_2-charged brines flowing up the faults, mix with meteoric fluids in the

Navajo Sandstone and flow parallel to the faults where they are sealing, and to the south-east where they are transmissive, being driven by the regional gradient in groundwater head.

Figure 4 Geological cross section parallel to the plane of the Little Grand Wash Fault and perpendicular to the axis of the Green River anticline constructed with stratigraphic data from oil exploration drill holes (after Solum pers comms. 2012). Drillhole locations shown are for the CO2W55 drillhole, Crystal Geyser, Airport Well and the Green Town Federal 36-11 drill hole which transected CO2-charged reservoirs in the Permian and Carboniferous stratigraphy. The cross section shows the distribution of the main CO2 reservoir horizons in the Permian and Jurassic stratigraphy; the White Rim Sandstone, Wingate Sandstone, Navajo Sandstone and Entrada Sandstone. The juxtaposition of reservoir rocks in the footwall and hangwall blocks is shown. The position of a hypothetical gas-water contact is shown for each reservoir formation, controlled by the position of the reservoir spill point. The location of fluid samples collected from the CO2W55 drillhole are shown (red stars, orange and yellow triangles).

Figure 5 Cross section of the region surrounding drill hole CO2W55 showing the location of the Little Grand Wash fault system, including the northerly fault transacted by the drill hole (limited exposure precluded mapping this at surface), and the CO_2-driven cold water geyser at Crystal Geyser. The transect taken by the drill-hole is projected on the left-side of the figure. The general structure of the fault is also shown using information from field mapping and in Shipton *et al.,* (2004) and Dockrill and Shipton, (2010).

Figure 6 Sedimentary log of the core recovered from drill-hole CO2W55 showing the main geological features of the three units, the Entrada Sandstone, Carmel Formation and Navajo Sandstone, transacted by the drill-hole. Zones of CO_2-degassing core and hydrocarbon bearing zones are also shown.

Figure 7 A) Sandstone bleaching in exhumed portions of the Entrada Sandstone, Salt Wash Graben. B) High angle fracture zones adjacent to the fault with zones of intense bleaching and gypsum and pyrite mineralization on the fracture walls. C) Bleached halo around open mineralized fracture D) Bleached halo around high angle fracture in the Entrada Sandstone, CO2W55 core. E-F) Gypsum and pyrite filled fracture in the bleached Entrada Sandstone G) Bleached Siltstone-sandstone contacts from CO_2-hosting sections of the Entrada Sandstone. H) Sections of gypsum beds and gypsum filled fracture zone in the Carmel formation I) Bleached claystone at the interface between the Carmel caprock and CO_2-charged Navajo Sandstone J) Bleached Navajo Sandstone.

Figure 8 A) Formation pressures estimated for the Jurassic through to the upper Carboniferous stratigraphy of the Green River anticline. Formation pressures are estimated from mud weight gradients used in oil exploration drill holes. Also shown is the theoretical hydrostatic pressure gradient. B) The difference between the hydrostatic pressure gradient and formation pressures estimated from mud weight data are used to estimate the formation overpressure. This represents an upper bound and actually formation over pressure may be less than the estimate. Reservoirs become increasingly overpressures with depth due primarily to the artesian nature of this portion the Paradox Basin.

Figure 9 A) Schematic diagram of the Leutert Positive Displacement Bottomhole Sampler redrawn from www.leutert.com. B-C) Photograph and schematic diagram of the high-pressure pH rig constructed to measure fluid pH on samples recovered using the PDS sampler. D) Schematic diagram of the micro-piston cylinder system used to capture dissolved CO_2 by mixing sample with an excess of KOH solution.

Figure 10 Crystal Geyser level logger data (water temperature and water level) during drilling of scientific drill-hole CO2W55. The level logger was installed at a depth of ~5m below the mouth of the geyser. Typically, a single eruption cycle (SEC) of Crystal Geyser is composed of two major eruption events (Type B and D eruptions) of varying duration and frequency, each proceeded by small frequent bubbling events (Type A and C eruptions), and each followed by a recharge period (R^1 and R^2; nomenclature following Han *et al.,* 2013). Type B and D eruptions comprise short duration large magnitude and long duration low magnitude eruptions, respectively. During the drilling of hole CO2W55 the typical pattern of eruptions, eruption durations and frequent was significantly perturbed. Only a single Type B eruption was observed of much reduced magnitude and duration. An increased duration and reduced frequency of Type D eruptions was observed (see Fig 10). Also shown are drillers depths and formation intervals for hole CO2W55 at various times during the course of drilling. Periods of cementing, redrilling cement, fluid sampling, flowing the hole and waiting are also shown.

Figure 11 A) A compilation of eruption duration and frequency data for Crystal Geyser from various studies from 1978 to 2010, redrawn after Han *et al.,* 2013. B) Eruption data for Crystal Geyser during drilling of hole CO_2W55.

Figure 12 A) In-situ pH measured on pressurized samples and alkalinity determined by gran titration in the field. B) Dissolved CO_2 concentrations measured directly on titrated samples and recalculated from measured pH and alkalinity. Also shown is the theoretical CO_2 solubility curved calculated for a hydrostatic pressure gradient, local geothermal gradient and measured salinity profile using the equations of Duan *et al.,* 2006.

Figure 13 Anion concentrations (and boron) in fluid samples collected from Jurassic CO_2-charged reservoirs, during drill-hole CO2W55. Downhole fluid samples collected from the Navajo sandstone using the Leuterts wireline sampler (red squares) are number 1-4 in order of sample depth. Samples from the Entrada Sandstone (yellow triangle), Carmel Formation (orange triangle) and Navajo Sandstone (pink squares) were collected at surface when the hole was flowing.

Figure 14 Major and minor cation concentrations (Na, K, Li, Rb) in fluid samples collected from the Jurassic CO_2-charged reservoirs, from drill-hole CO2W55.

Figure 15 $\delta^{18}O$ and δD isotope ratios of fluids sampled from the CO2W55 drill-hole.

Figure 16 $\delta^{34}S_{SO4}$ and $\delta^{18}O_{SO4}$ of sulphate in fluids sampled from the CO2W55 drill-hole.

Figure 17 Sr concentrations and Sr-isotope ratios in fluid samples collected from the Jurassic CO_2-charged reservoirs, during drill-hole CO2W55.

Figure 18 Groundwater chemistry of CO_2-charged fluids from drill-hole CO_2W55 showing profiles for elements buffered by fluid-rock reaction; Ca, Mg, Sr, Fe, Mn, Al and Si.

Figure 19 Element cross plots of fluid chemistry from the CO_2W55 drill-hole, Crystal Geyser and other CO_2-springs from the Green River anticline. The ratio of halogen, alkali and alkaline metals are consistent with fluid mixing between dilute meteoric fluid and brine derived from the Paradox Formation, which is enriched in B, Br, Cl, Li, K, Na, Rb and SO_4^{2-}. Paradox Valley brine compositions taken from Rosenbauer *et al.*, (1991).

Figure 20 $\delta^{18}O$ and δD isotope ratios for fluid of Navajo Sandstone fluids from the CO_2W55 drill-hole and CO_2-springs from the Green River anticline from this study and from Heath *et al.,* (2009). The CO_2-charged fluids deviate from the North American Meteoric Water Line, as defined by local surface waters from Mayo et al, (1992), due to mixing with isotopically heavy saline brines from the Paradox Formation ($\delta^{18}O$: 2.19‰ and δD -42‰; Spangler *et al.,* 1996).

Figure 21 A-B) Basin scale salinity profiles for formation fluid samples from the brine-rich Carboniferous aquifers and White Rim Sandstone, recovered during oil exploration drilling on the Green River anticline. Elevated salinity in the White Rim and Jurassic sandstone aquifers reflects intrusion of the CO_2-charged brines from depth. C) HCO_3 concentrations in formation fluid samples. Alkalinity in Carboniferous, White Rim and Jurassic sandstone aquifers are elevated due to fluid-rock reactions between the CO_2-charge fluids and carbonate and silicate reservoir minerals. D) Basin-scale CO_2 solubility curve

Figure 22 Element cross plot showing dilution of Carboniferous brines by mixing with meteoric fluids in the shallower CO_2-reservoirs of the White Rim Sandstone and Jurassic Sandstones. Brine compositions from Rosenbauer *et al.,* (1991) and Breit and Skinner, (2002).

Figure 23 Brine inputs along flow paths within the Navajo Sandstone, parallel to the Little Grand Wash and Salt Wash faults, calculated from Cl and Br concentrations in the spring waters and end-member fluids.

Figure 24 $^{87}Sr/^{86}Sr$ for fluids and minerals relevant to this study. From bottom to top this includes the Sr-isotopic composition of; i) brine from the Paradox Formation, Greater Aneth oil field (Spangler et al., 1996); (ii) typical groundwaters from the Navajo Sandstone where CO_2 is absent (Naftz *et al.,* 1997); (iii) the Green River CO_2 springs, which sample fluid primarily from the Navajo Sandstone (Kampman *et al.*, 2009); (iv) Crystal Geyser (this study); (v-vii) CO2W55 Navajo, Carmel and Entrada Sandstone fluids (this study); (viii-xi) CO_2-deposited aragonite veins from the Little Grand Wash and Salt Wash faults (Kampman *et al.,* 2012); (x) Calcite and gypsum veins from bleached Entrada Sandstone, Salt Wash Graben; (xi) Carmel Fm. gypsum beds from the CO2W55 core; (xii) Navajo Sandstone Fe-dolomite cements from the CO2W55 core; (xiii) Silicate fractions of the Navajo and Entrada Sandstones from regional compilation of samples and the CO2W55 core (this study and Truini and Longsworth, 2003) (xiv) carbonate fractions of typical diagenetic calcite and dolomite cements from the Navajo and Entrada Sandstones (this study and Goldstein et al.,

2008) and; (xv) calcite veins and hematite concretions associated with regional hydrocarbon bleaching of the Jurassic Sandstones (Chan *et al.*, 2000).

Figure 25 Saturation index for (A) carbonate, (B) Fe-bearing, (C-D) silicate, (E) sulphate and (F) silica minerals in fluids sampled from the CO2W55 drillhole calculated using PHREEQC.

Figure 26 Cross plots of carbonate and metal-oxide derived solutes for fluids from the CO_2W55 drill-hole. Also shown are Mg/Ca and Sr/Ca ratios for the carbonate fraction of leachates from samples of the Navajo Sandstone from the CO2W55 core.

Figure 27 Quantitative mineralogy from; (i) XRD analysis of representative samples from the Navajo Sandstone from the CO2W55 core and; (ii) a compilation of quantitative mineralogy of representative unbleached samples of the Navajo Sandstone (from data in Chan et al., 2000; Beitler et al., 2005).

Figure 28 Back scatter electron (BSE) images of carbonate cements within samples of the Navajo Sandstone from the CO2W55 drillhole, and from a nearby drill core where CO_2 is absent. Increasing brightness in the backscatter images relates primarily to increasing Fe-concentration in the mineral. (A) Typical Fe-poor diagenetic dolomite cements in samples from the Big Hole #2 core (see Figure 1 for location). (B) Zomplexly zoned dolomite cements from the upper CO2W55 core showing Fe-poor cores of original diagenetic cement overgrown by Fe-rich rims. (C) Complexly zoned Fe-rich dolomites with evidence for exstenseive dissolution-reprecipitiaiton, from the lower intervals of the Navajo Sandstone, in contact with the low pH brine inputs.

Figure 29 Time-series fluid chemistry from the build-up to and eruption of a Type B eruption of Crystal Geyser. Samples were collected in 2007, prior to drill of hole CO2W55. Temperature, Na, K, Cl and SO_4^{2-} concentrations and O-isotope of the expelled fluid evolve as the geyser initially samples brine enriched fluid from the Navajo Sandstone then progressively incorporates meteoric enriched fluid from the shallower cooler Entrada Sandstone reservoir.

Figure 30 Time-series fluid chemistry from the build-up to and eruption of a large short duration Type B eruption of Crystal Geyser. Samples were collected in 2007, prior to drill of hole CO2W55. Fluid chemistry evolves as the geyser samples different CO_2-reservoirs; initially sampling brine enriched fluid from the Navajo Sandstone followed by influx of Ca, Mg, Sr, Fe, Mn enriched fluid from the Entrada Sandstone, as a major eruption initiates.

Figure 31 Mixing diagrams for Br, Cl and Sr concentrations and Sr-isotopes ratios for fluids from drill-hole CO_2W55 and time-series fluid samples from Crystal Geyser. Navajo Sandstone drill-hole fluid samples plot along mixing lines between CO_2-saturated brine flowing in from the fault and dilute CO_2-undersaturated fluids descending from the fracture zone in the Carmel Formation. Time-series samples from an eruption of Crystal Geyser plot along a mixing line between the most saline fluids sampled from the geyser and fluid from the Entrada Sandstone that is enriched in Sr (and Ca, Mg, Fe and Mn) from the dissolution of carbonate and Fe-oxides in the host reservoir. In 1/Sr versus Sr-isotope space, Navajo

Sandstone surface fluid samples collected from the drill-hole show depletions in Sr concentrations without a corresponding change in the Sr-isotope ratio. This reflects loss of Sr from solution by the precipitation of carbonate minerals.

Figure 32 Mixing diagrams for Na, Ca, Mg and Mn versus Cl in fluids from the CO2W55 drillhole. (A) The fluids contain high concentrations of Na and changes in Na-Cl concentrations are dominated by fluid-fluid mixing trends. The Na concentration in the inflowing brine is elevated relative to concentrations expected for pure brine dilution, which may reflect enrichment of Na due to fluid-mineral reactions involving feldspar. (B-D) Ca, Mg and Mn concentrations in fluids sampled from the Navajo Sandstone are variably enriched and depleted in Ca relative to concentrations expected for pure fluid-fluid mixing, suggesting fluid-rock reactions involving carbonate and Fe-oxide minerals buffer the solute concentration.

Figure 33 The S- and O-isotopic composition of sulphate versus sulphate concentrations in fluid samples from the drill-hole and Crystal Geyser. Mixing lines calculated for mixing of the Carmel Formation end-member and the most saline fluid sampled by Crystal Geyser are shown.

Figure 34 Conceptual model of fluid flow, fluid mixing and fluid-rock reaction in the vicinity of drill-hole CO2W55. CO_2 and CO_2-saturated brine migrate through the fault from supercritical reservoirs of CO_2 in Carbonate formations at depth, mixing with meteoric groundwaters in fault and in sandstone aquifers in the White Rim and Wingate Sandstones. This dilutes the brine composition and the migrating CO_2 is progressively dissolved. Highly diluted CO_2-saturated brine eventually enters the base of the Navajo Sandstone, where it flows along the base of the formation mixing with CO_2-enriched groundwaters horizontally along the fault. CO_2-charged brines also enter the Entrada Sandstone were the flow laterally dissolving carbonate and hematite. These solute enriched solutions descend through the Carmel Formation, where they dissolve gypsum, before flowing into the upper portions of the Navajo Sandstone.

Figure 35 The change in dissolved inorganic carbon concentrations (DIC) in downhole fluid samples from the Navajo Sandstone versus (i) Cl concentration and (ii) of brine derived from the fault, from the Navajo Sandstone. In these CO_2-charged acidic waters DIC is predominantly CO_2(aq) with some HCO_3^-.

Table 1. Geochemistry of fluids sampled from the CO2W55 drill-hole. *sample contaminated with drilling mud.

Table 2. Isotope geochemistry of fluids sampled from the CO2W55 drill-hole

Table 3. Element and isotope geochemistry of fluids sampled from the CO_2-springs sampled in 2007.

Table 4. Composition of gas exsolved from the CO_2-springs sampled in 2007.

Table 5. Composition of gas exsolved from the CO_2-springs sampled in 2007.

Table 6. Element and isotope geochemistry of time-series samples from Crystal Geyser sampled in 2007.

Table 6. Sr-isotope geochemistry of leachates from rock samples used in this study.

Table 7. XRD data of Navajo Sandstone samples from the CO2W55 drill-hole.

Table 8. Estimated and measured composition of end-member fluids.

Supplementary Table 1. Geochemistry of fluids sampled from oil exploration drill-holes on the Green River anticline (references in text).

Figure 1

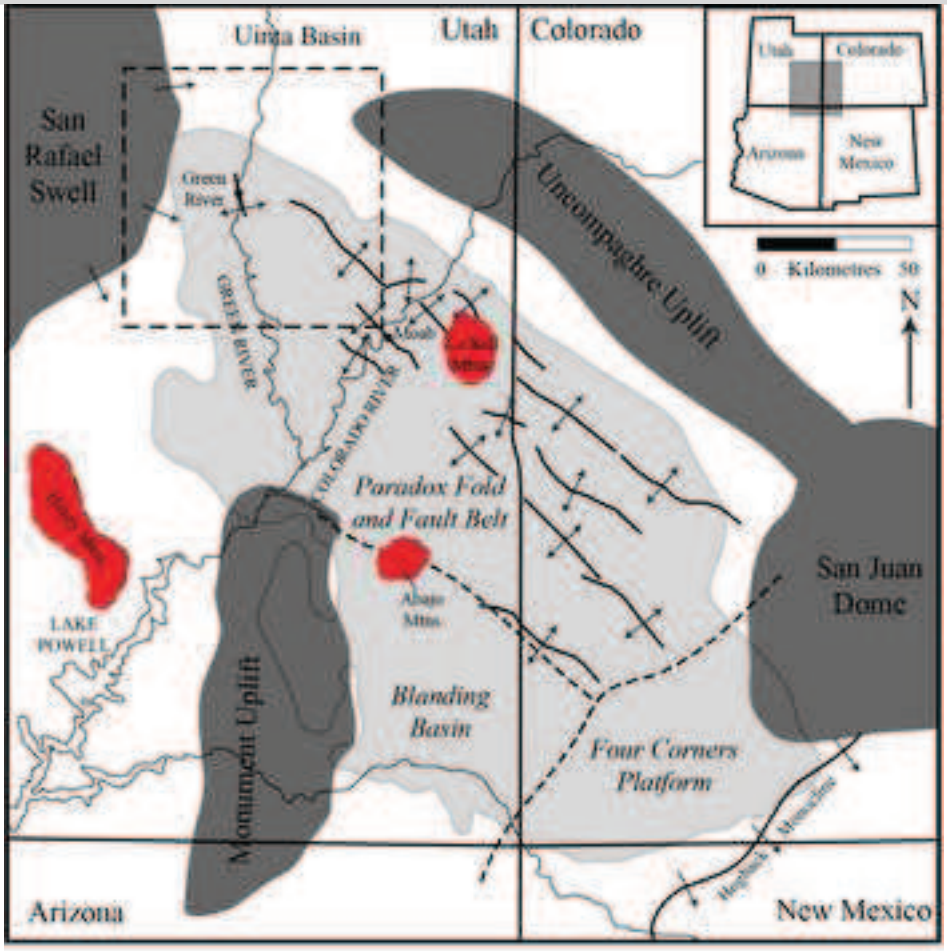

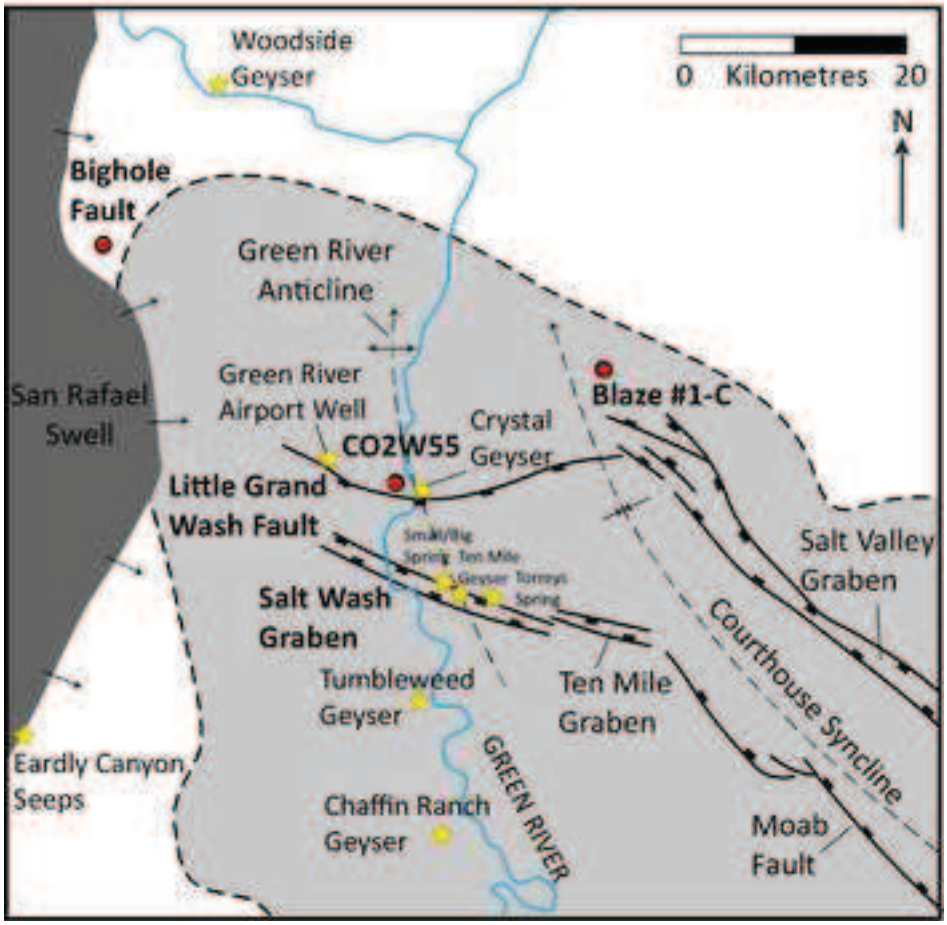

Figure 2

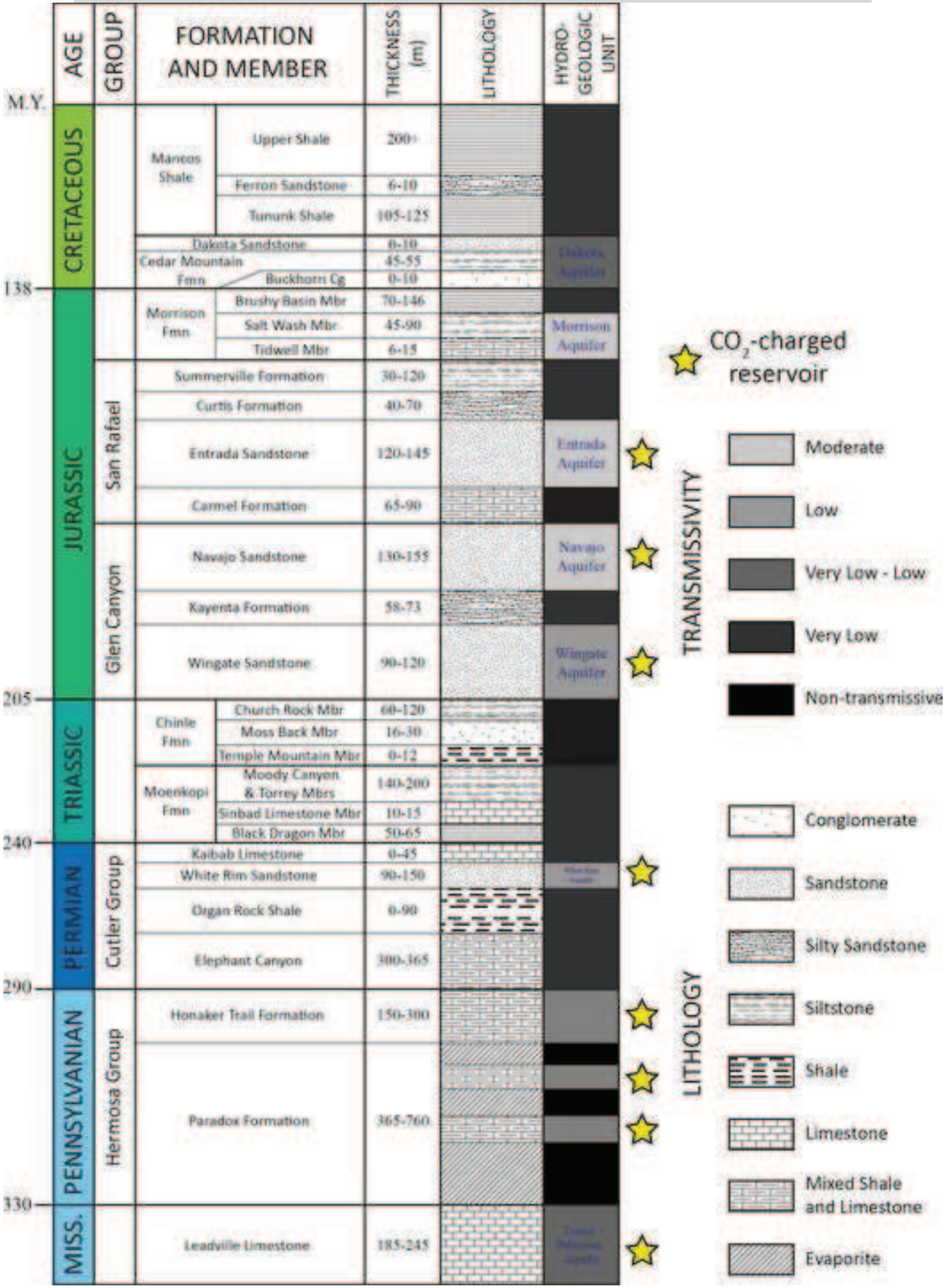

Figure 3

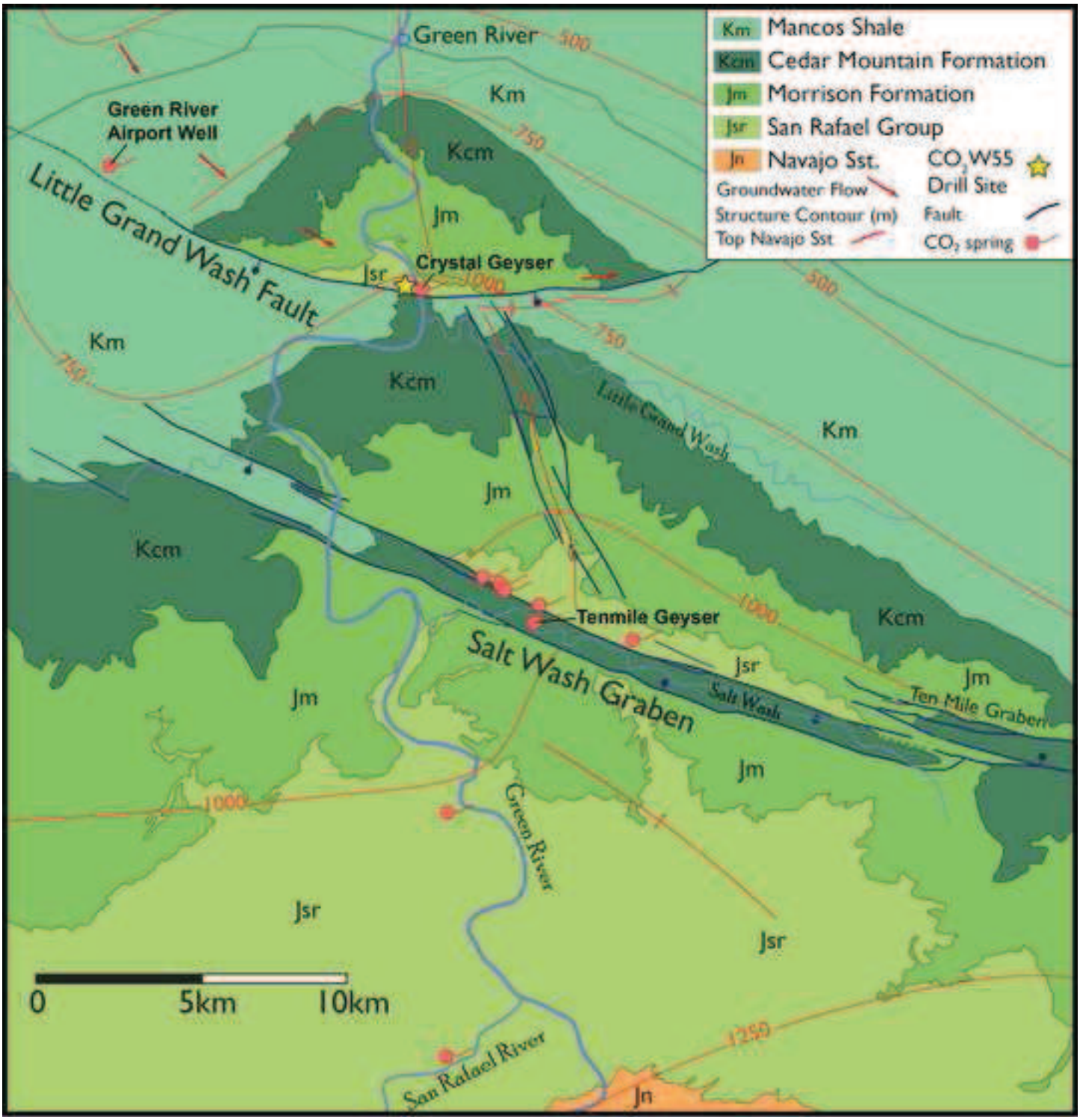

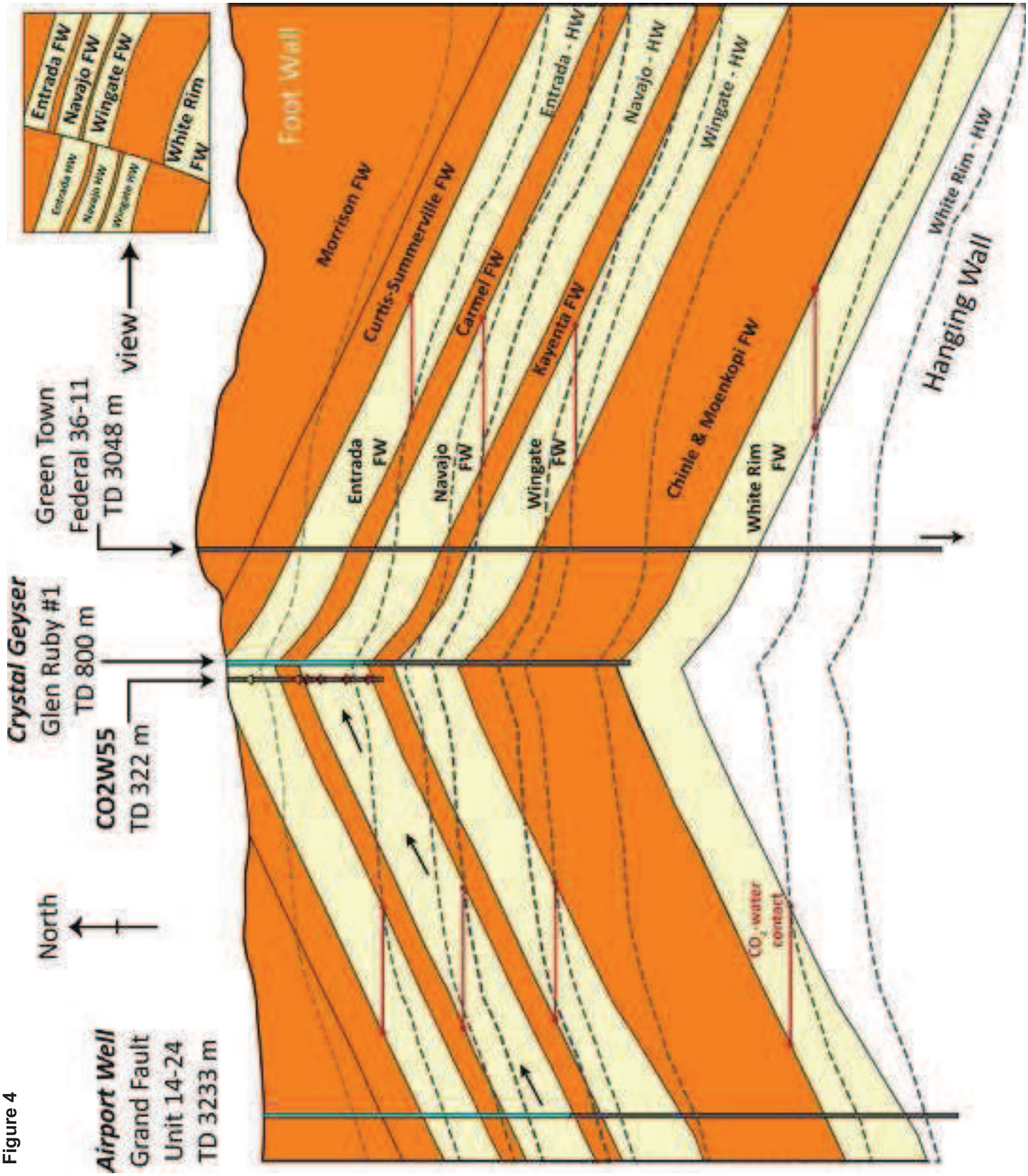

Figure 4

Figure 5

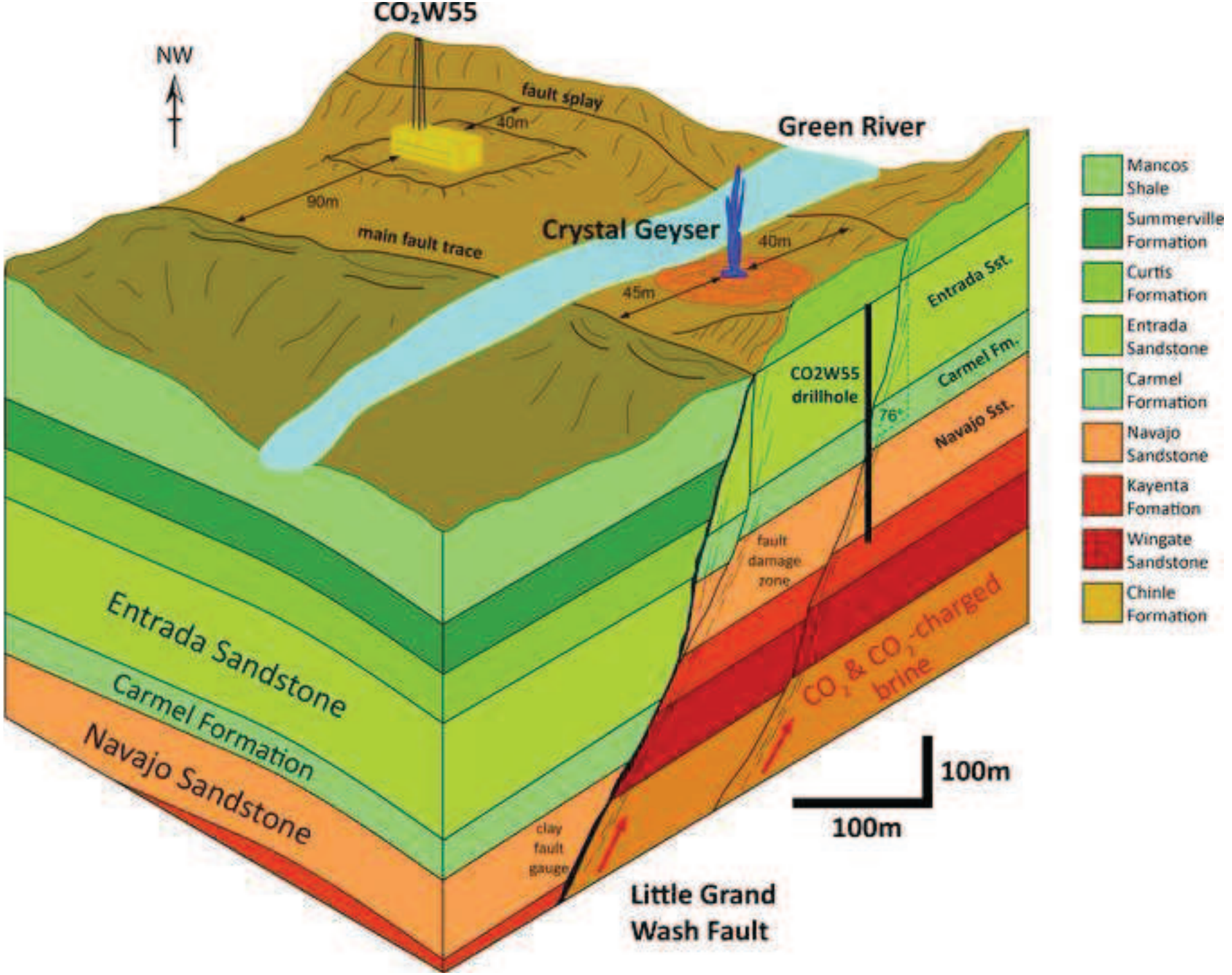

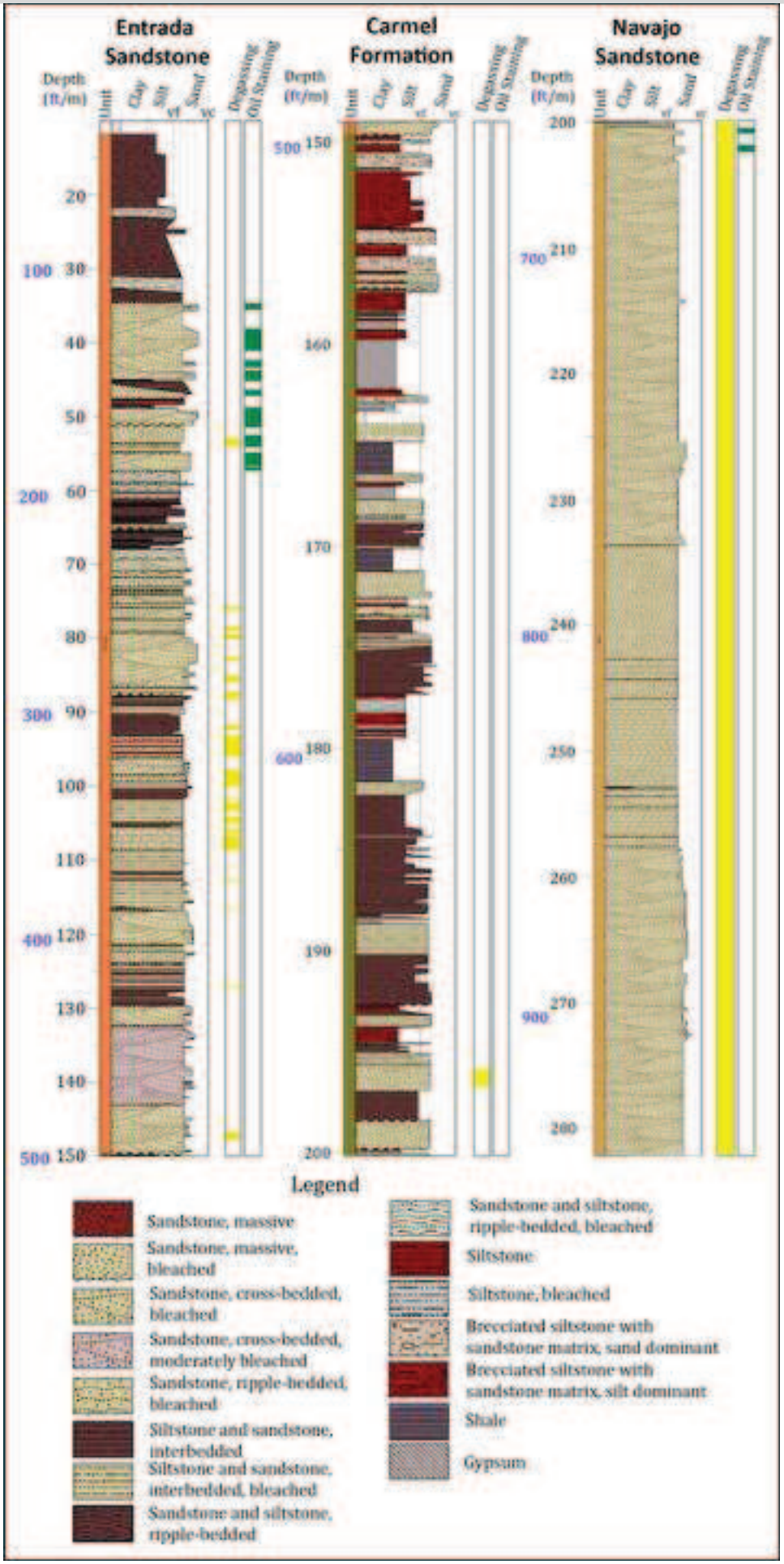

Figure 7

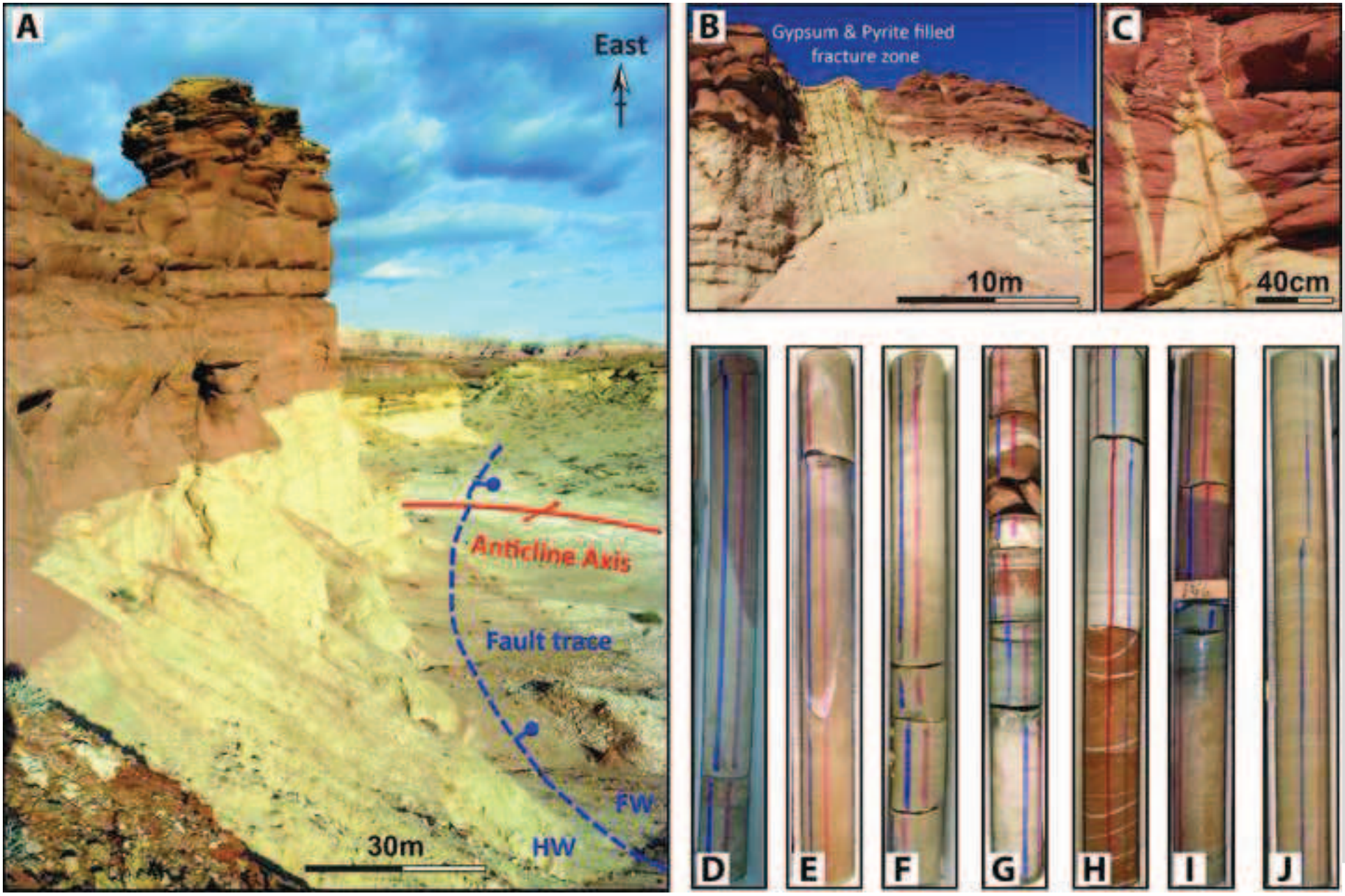

Figure 8

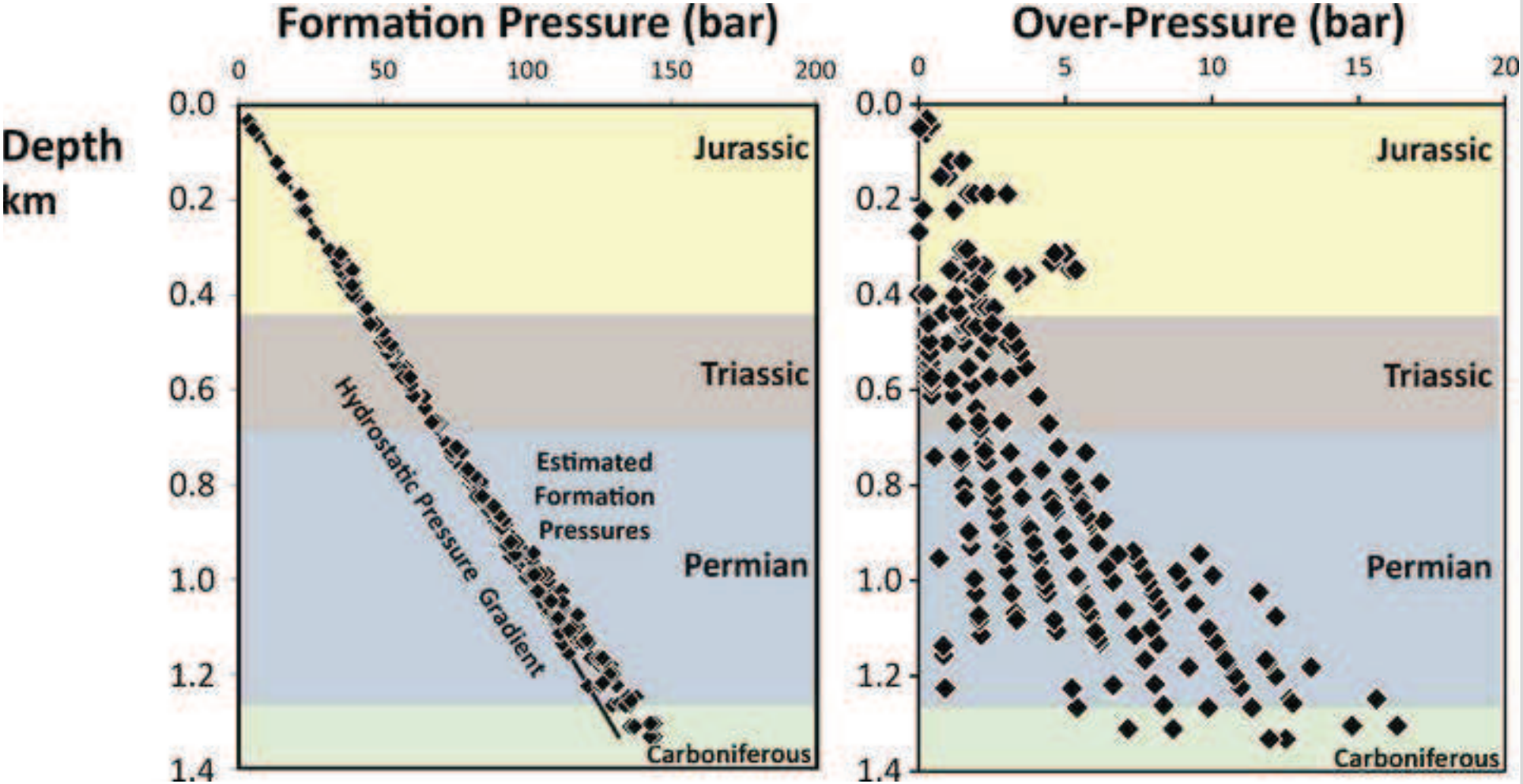

Figure 9

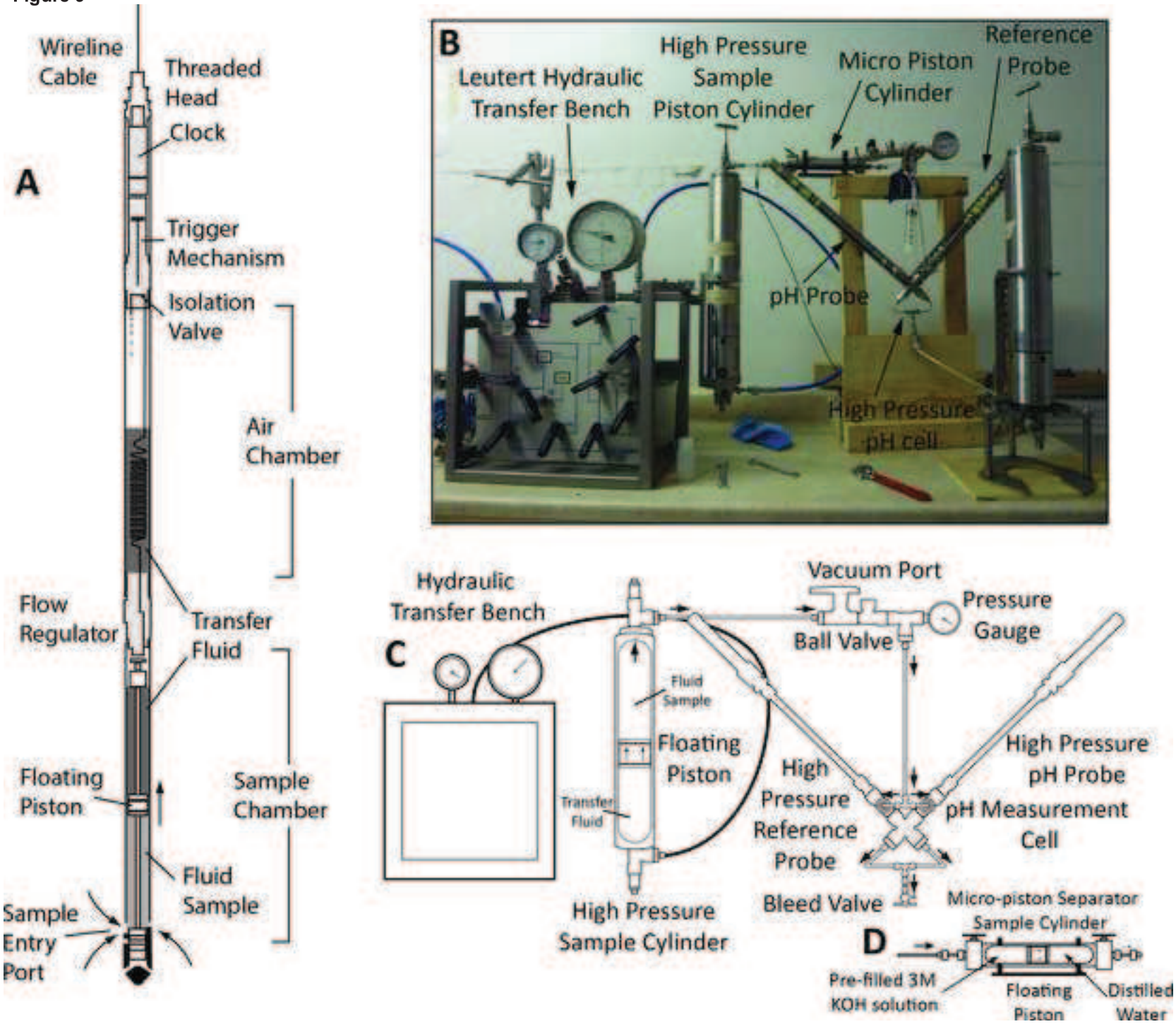

Figure 10

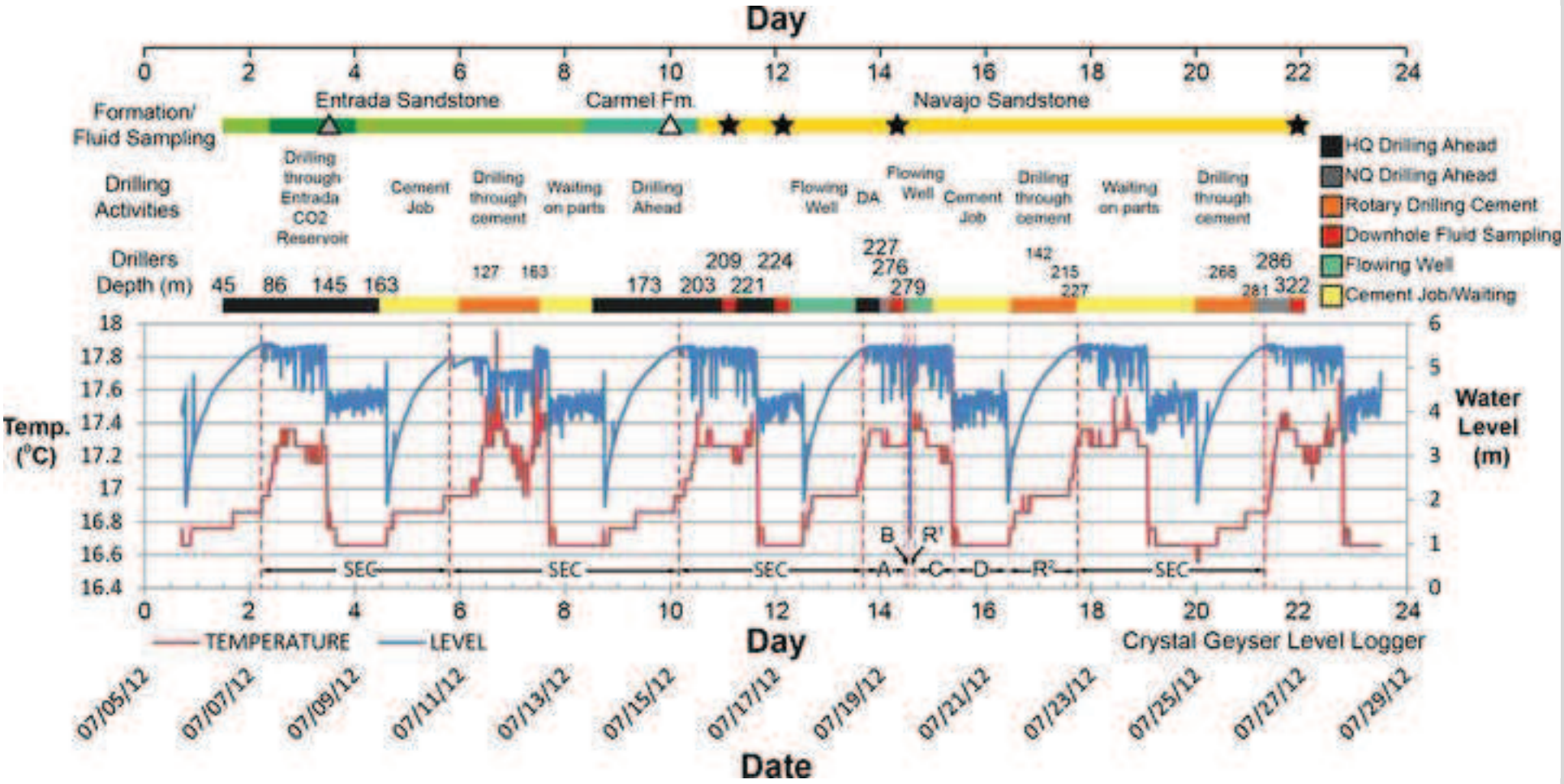

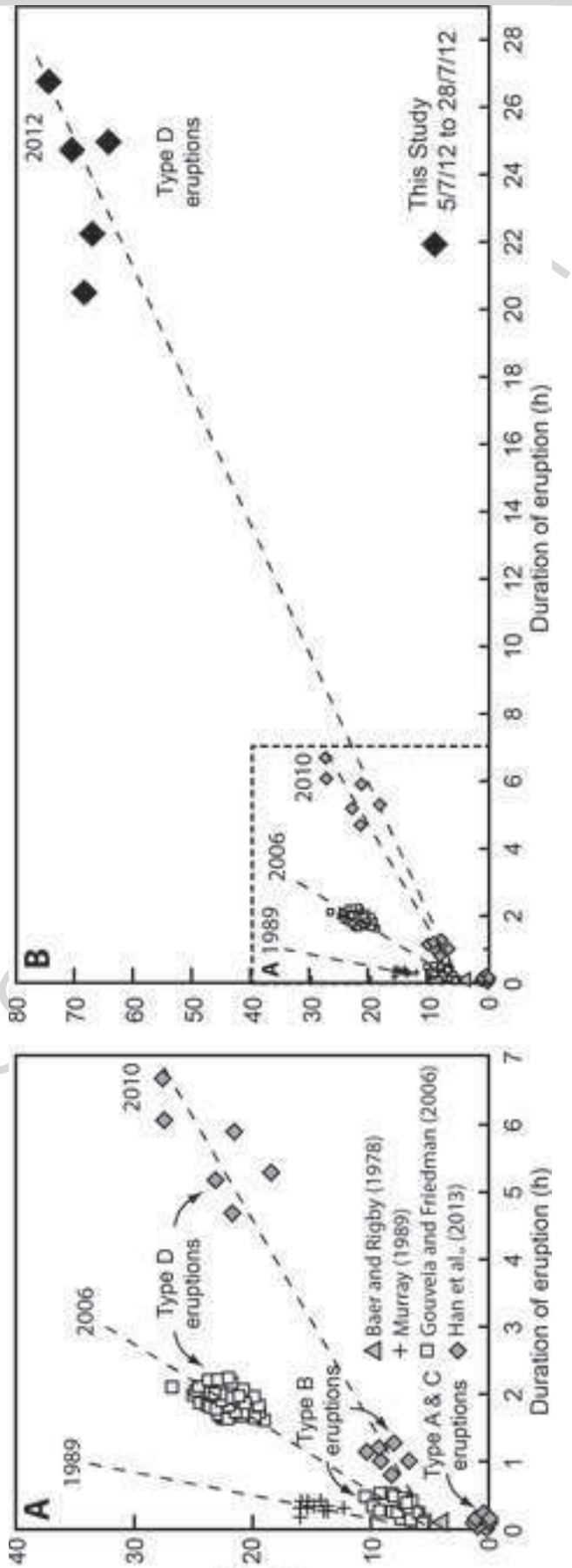

Figure 11

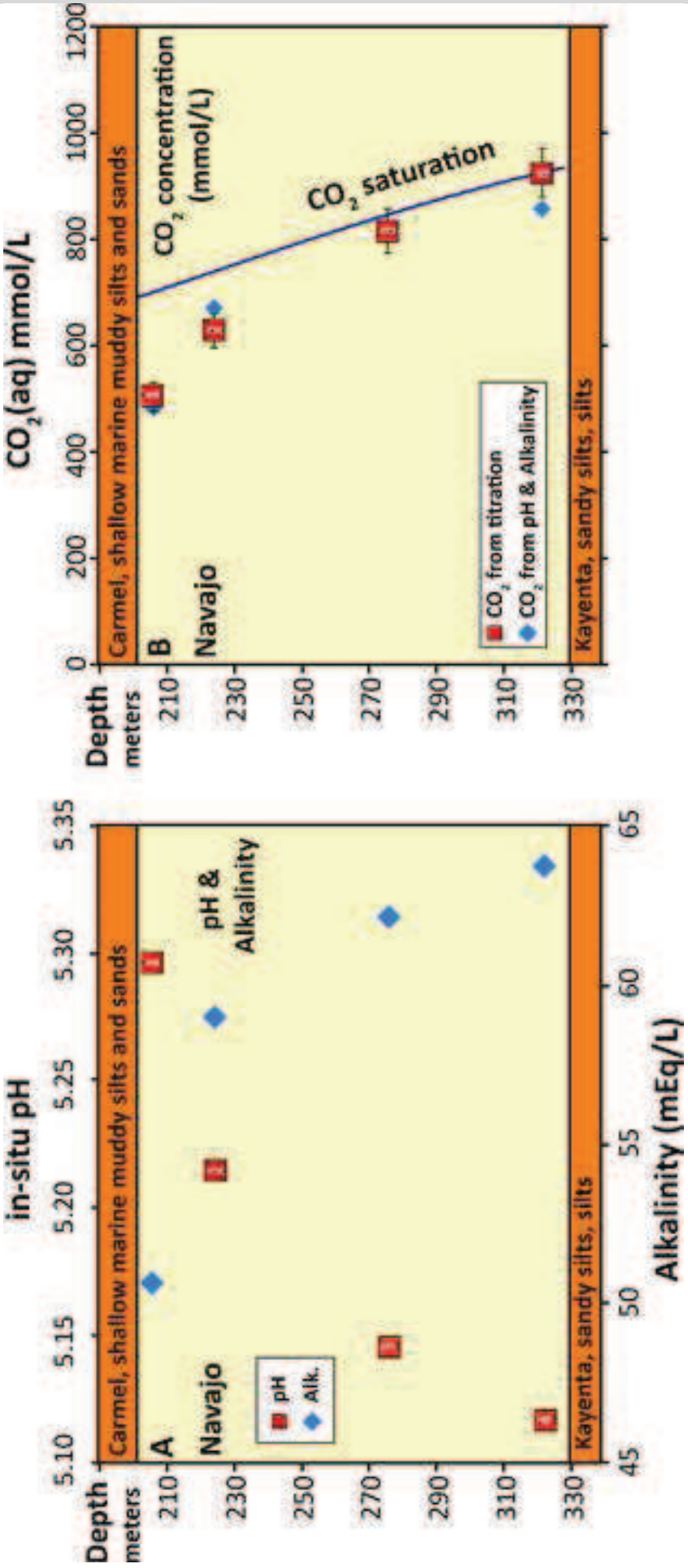

Figure 12

Figure 13

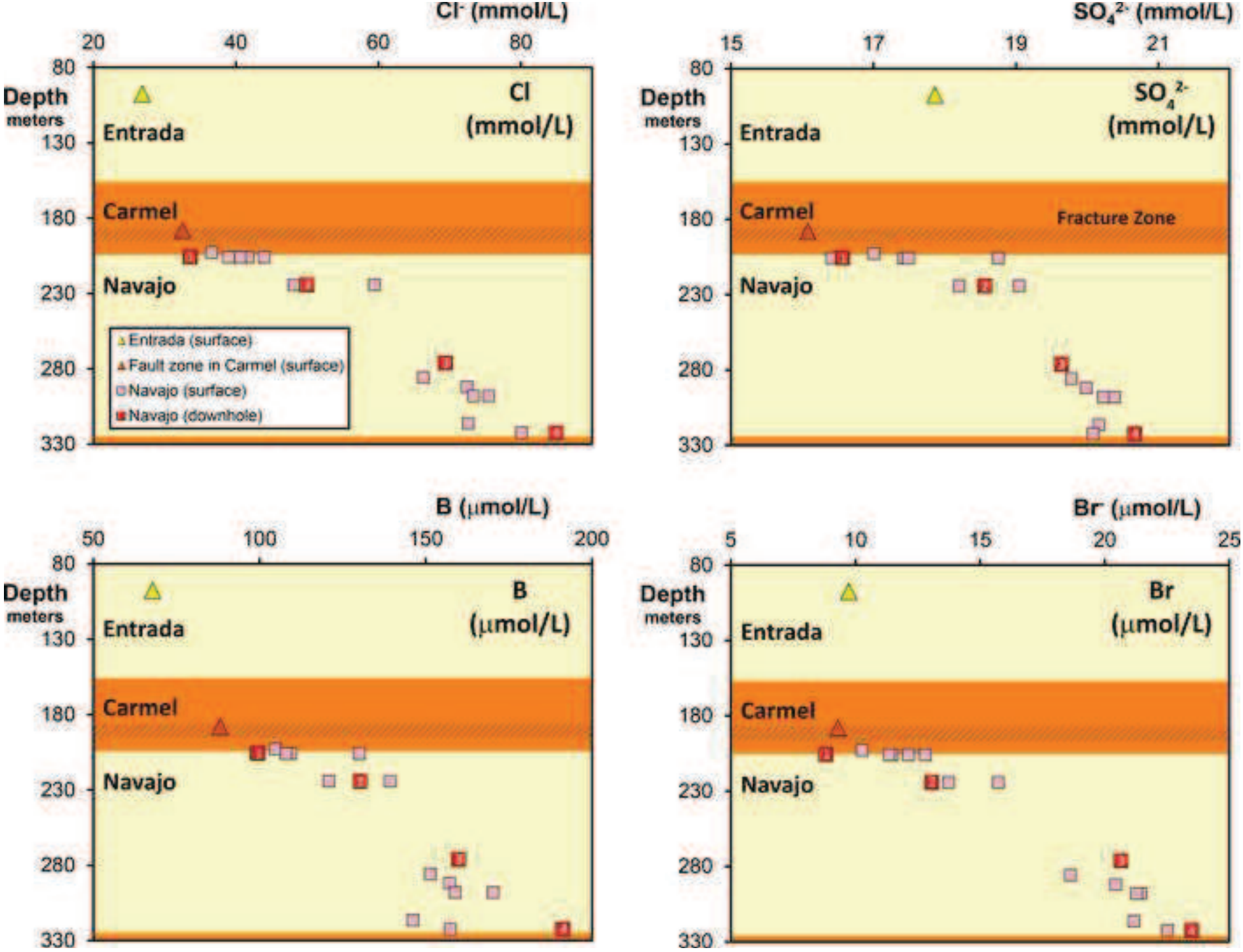

Figure 14

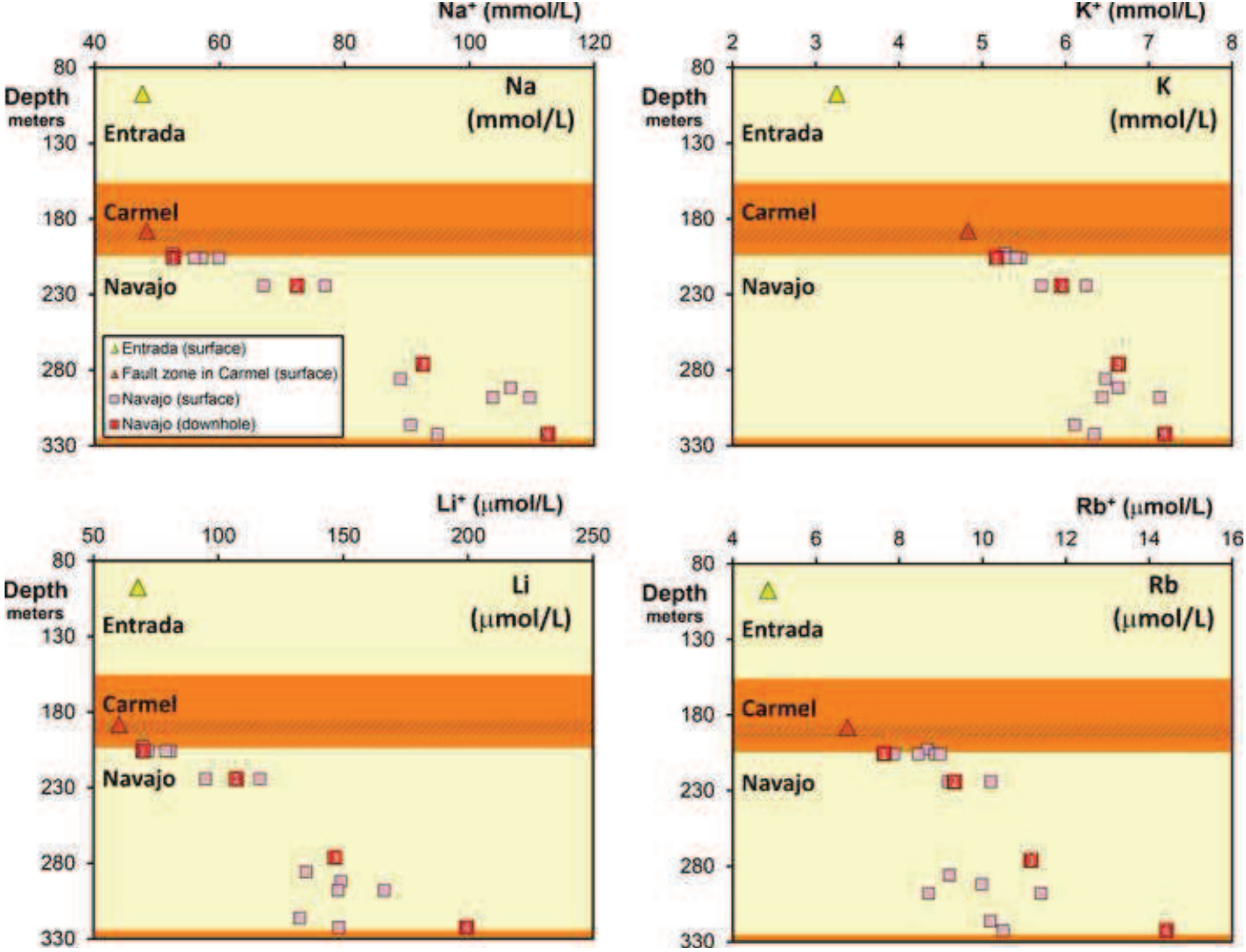

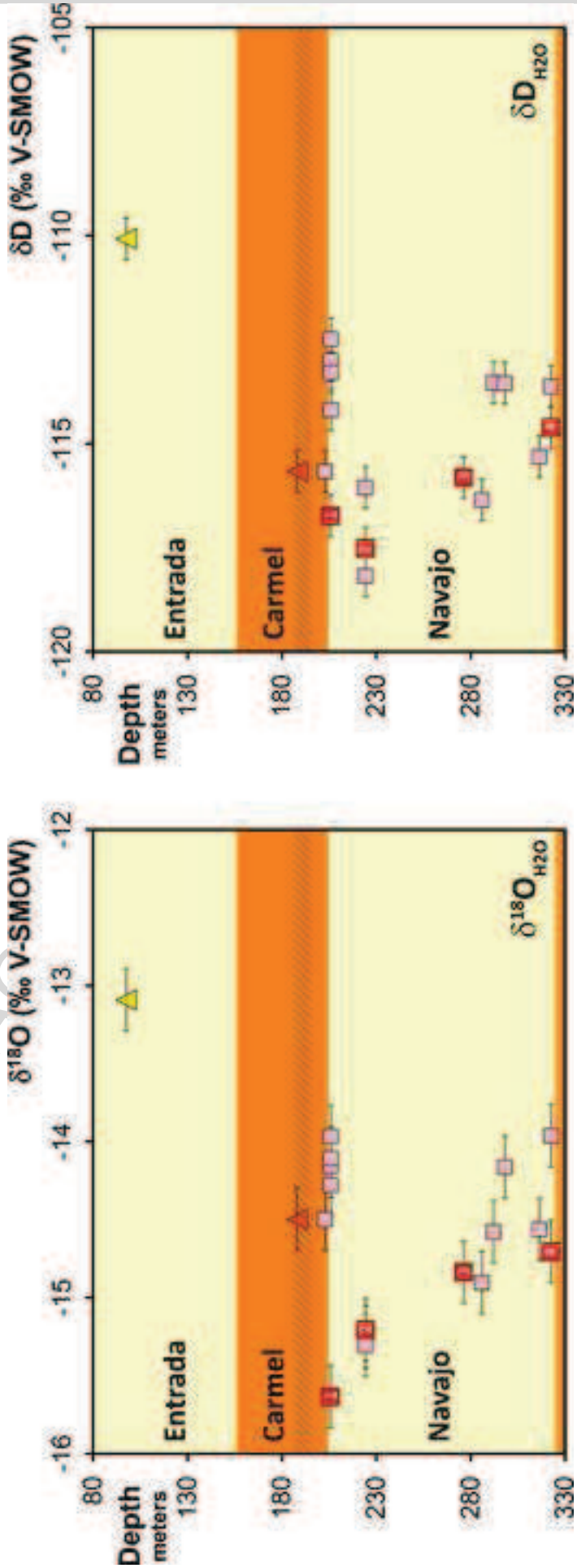

Figure 15

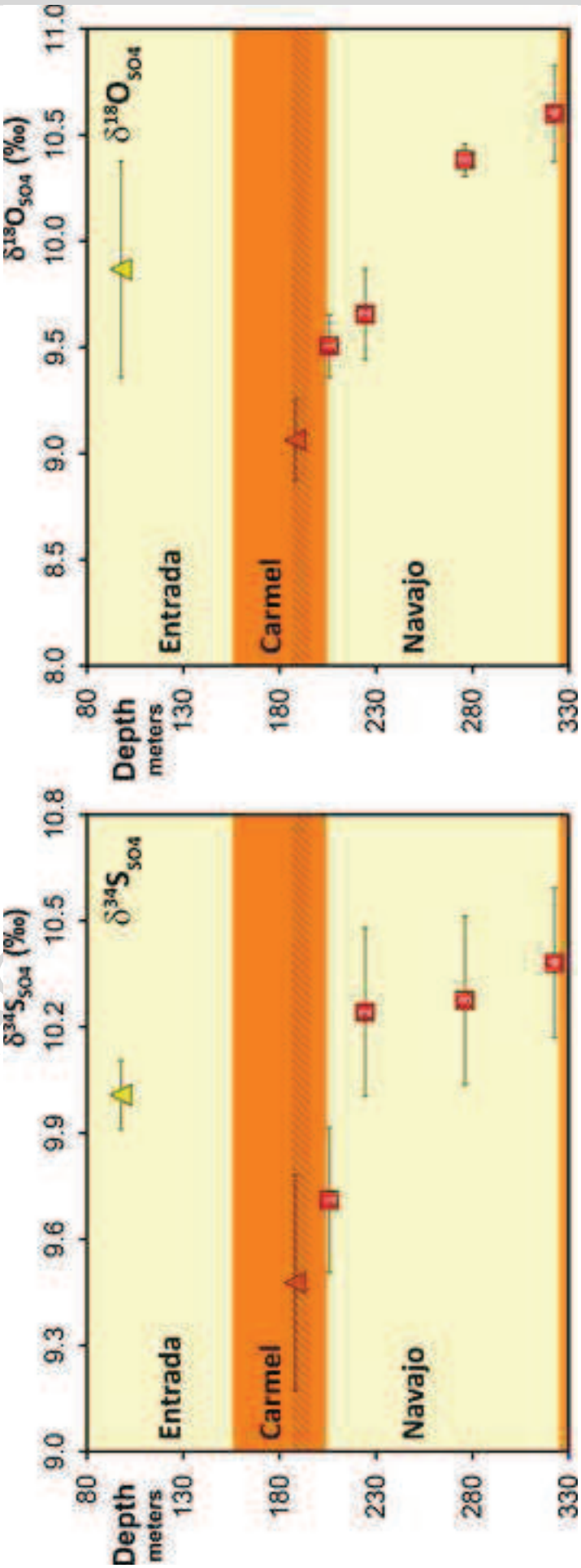

Figure 16

Figure 17

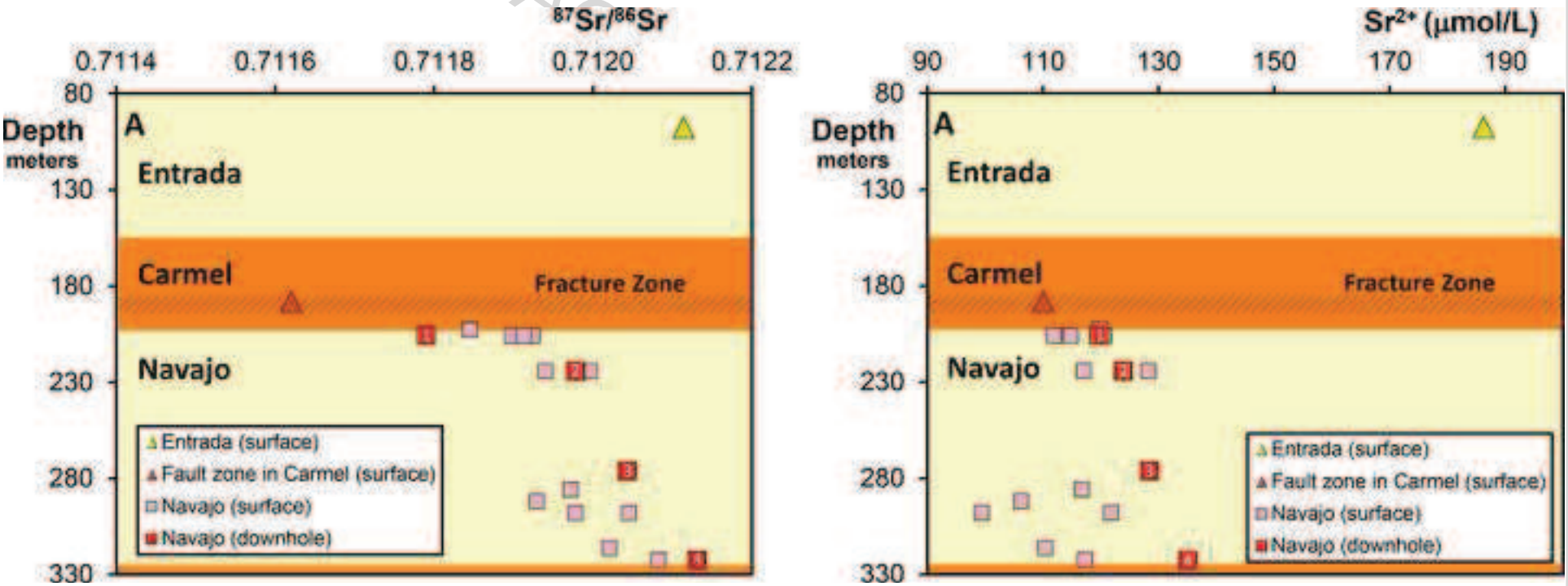

Figure 18

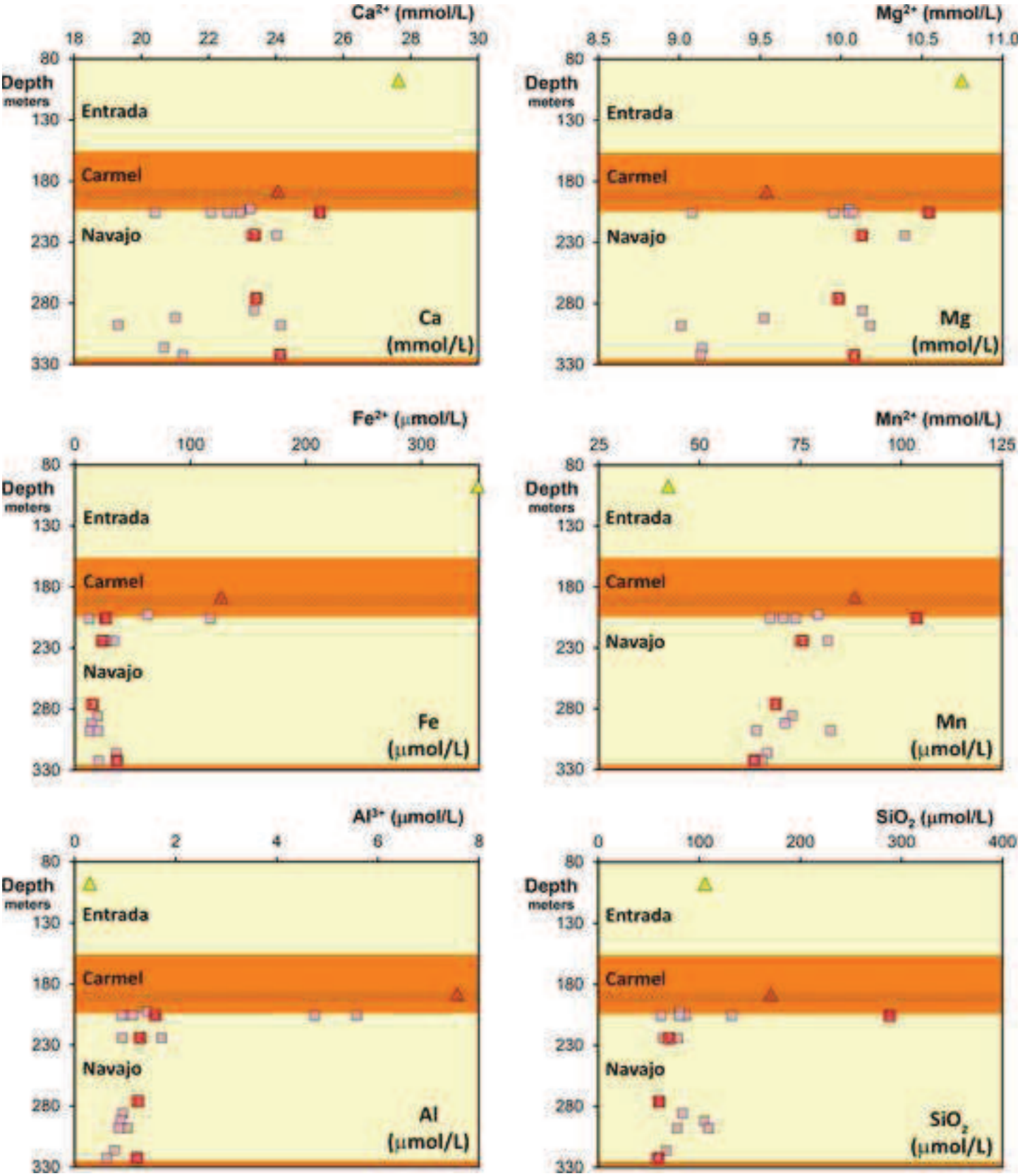

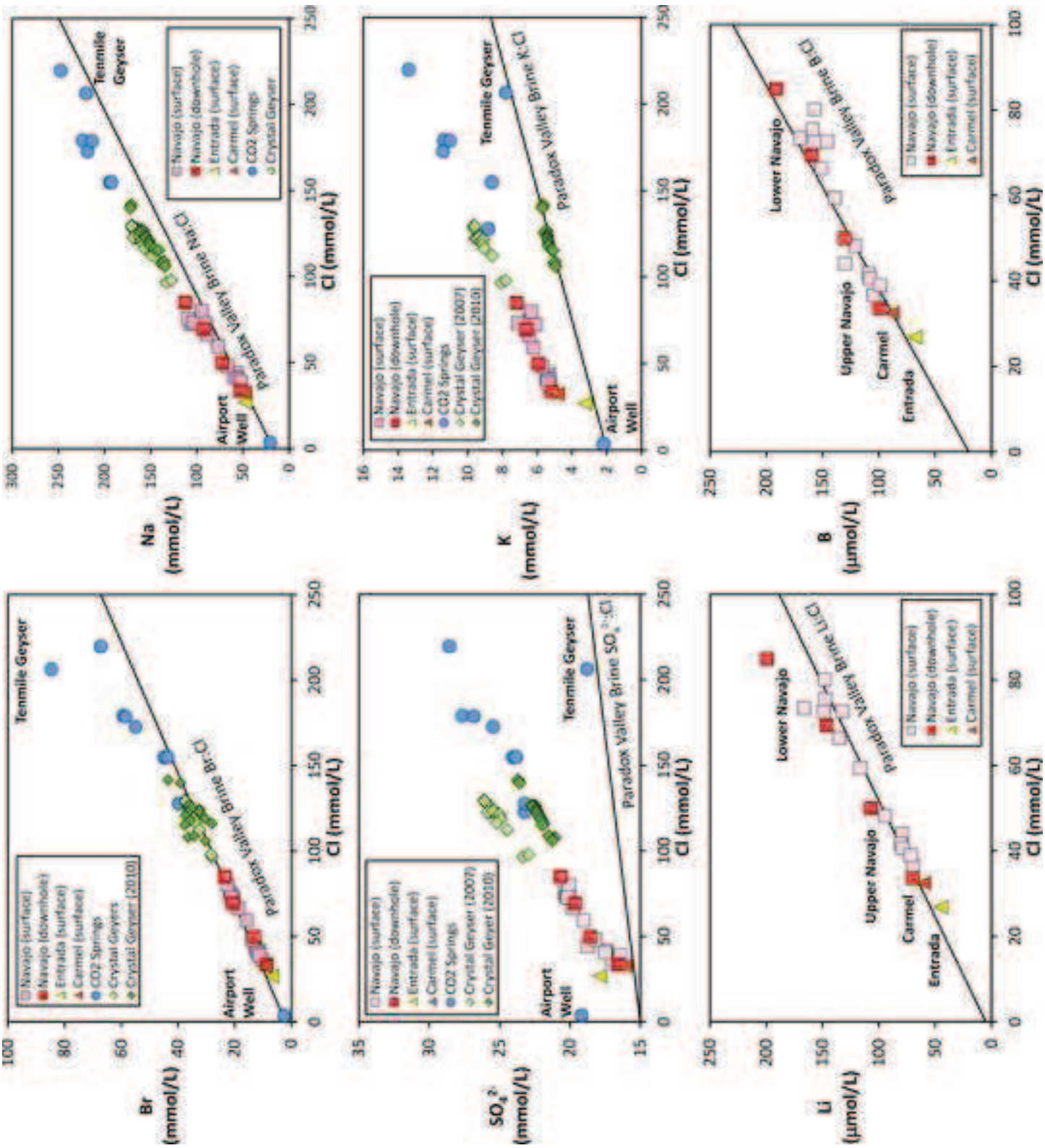

Figure 19

Figure 20

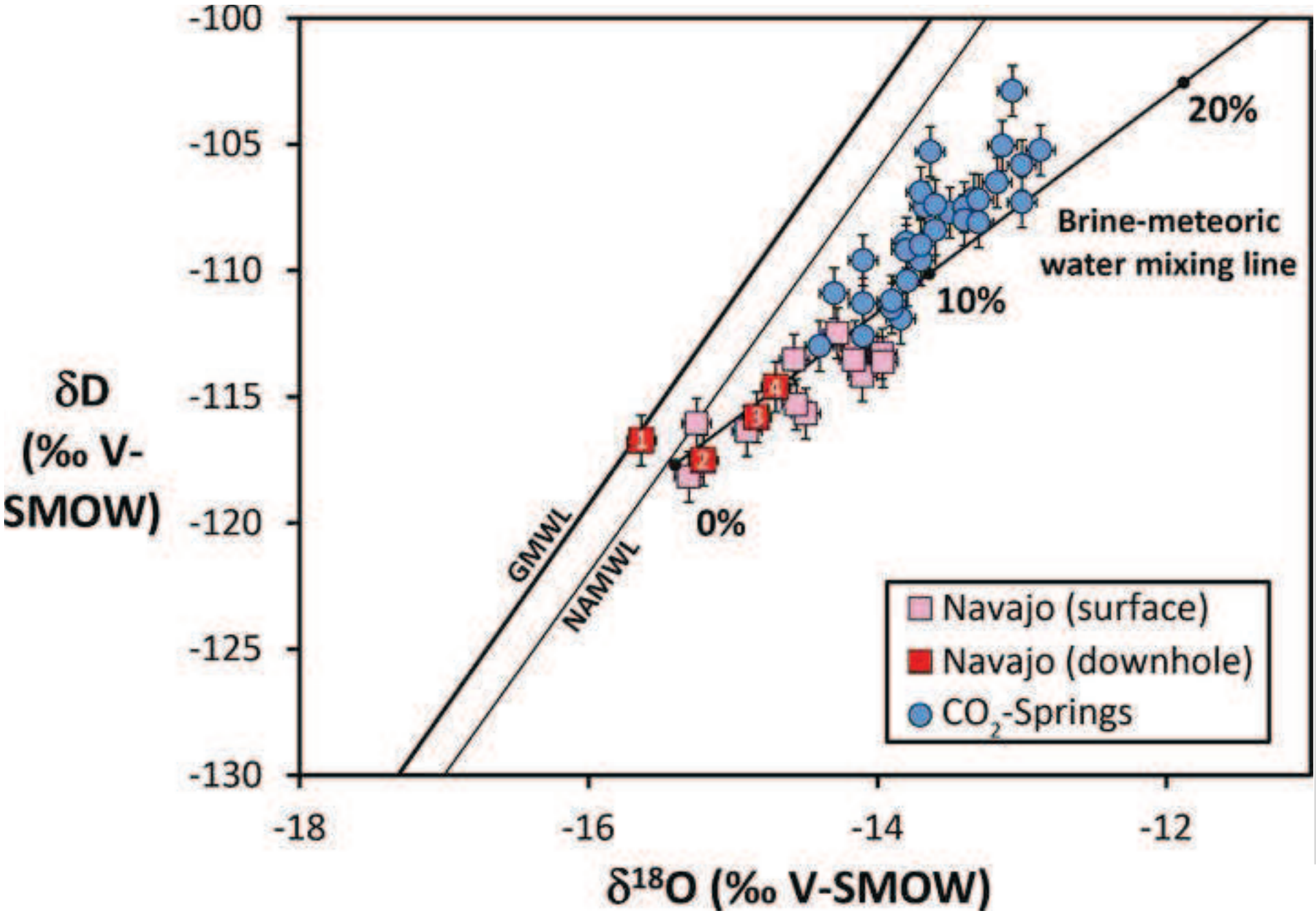

Figure 21

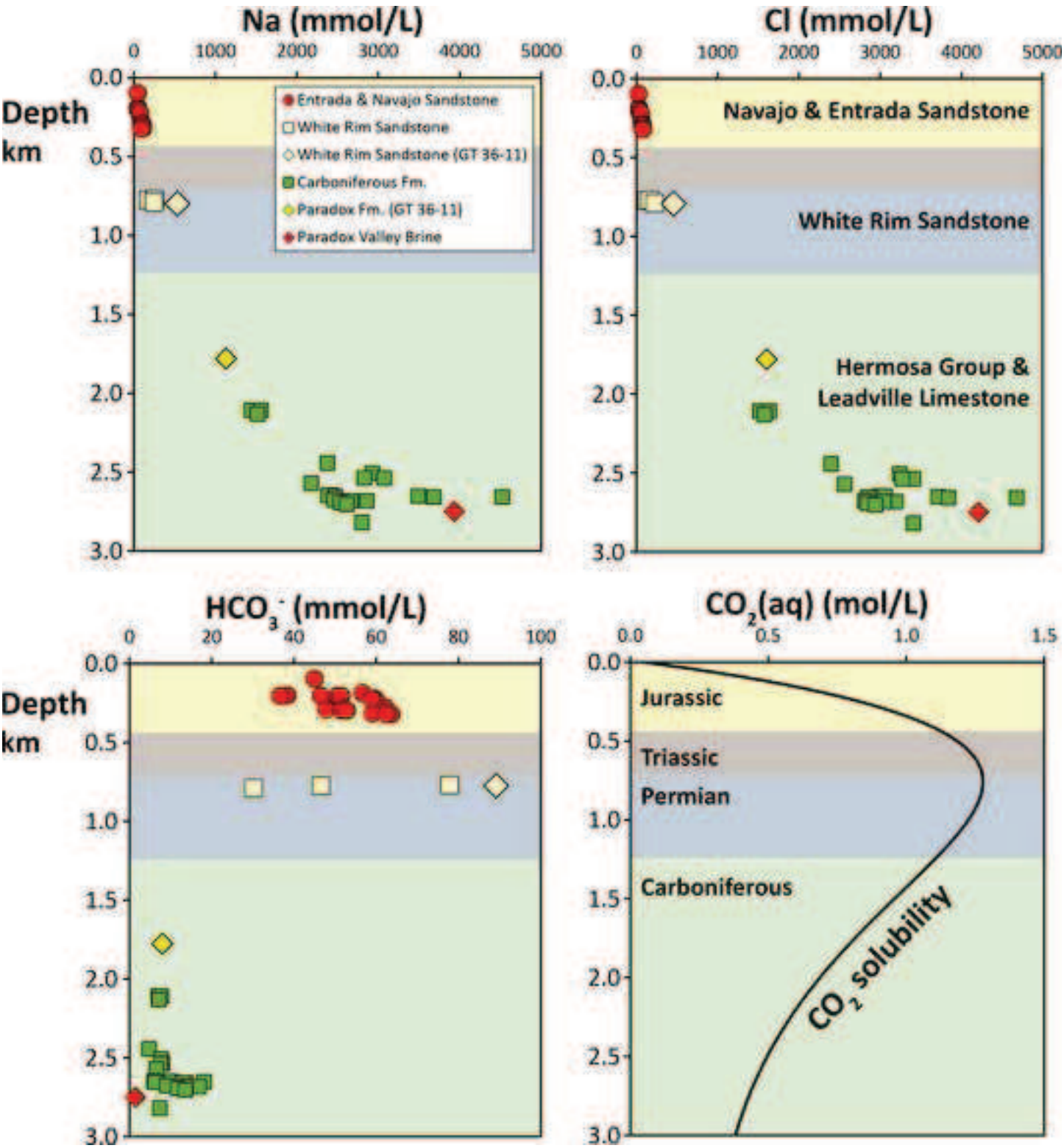

Figure 22

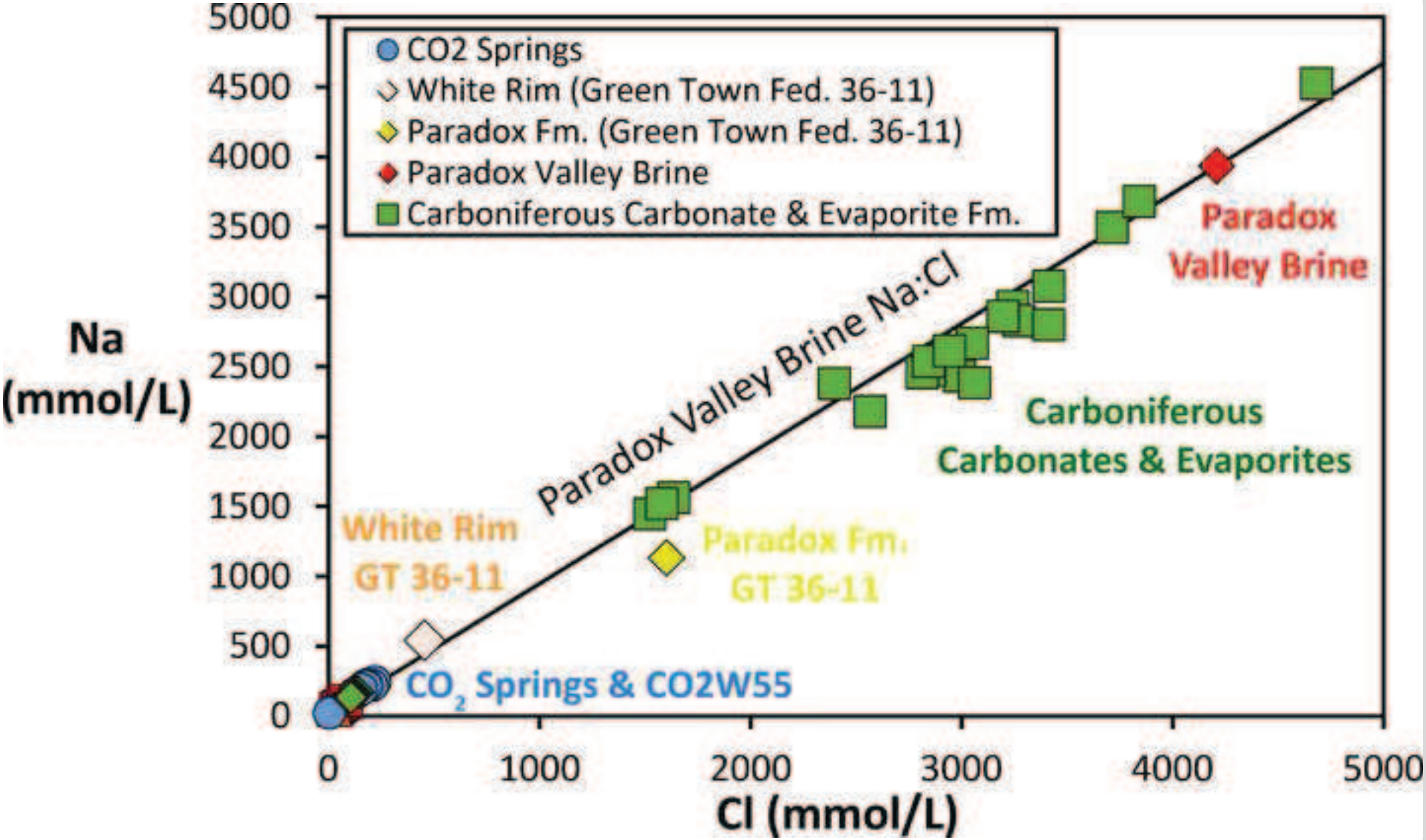

Figure 23

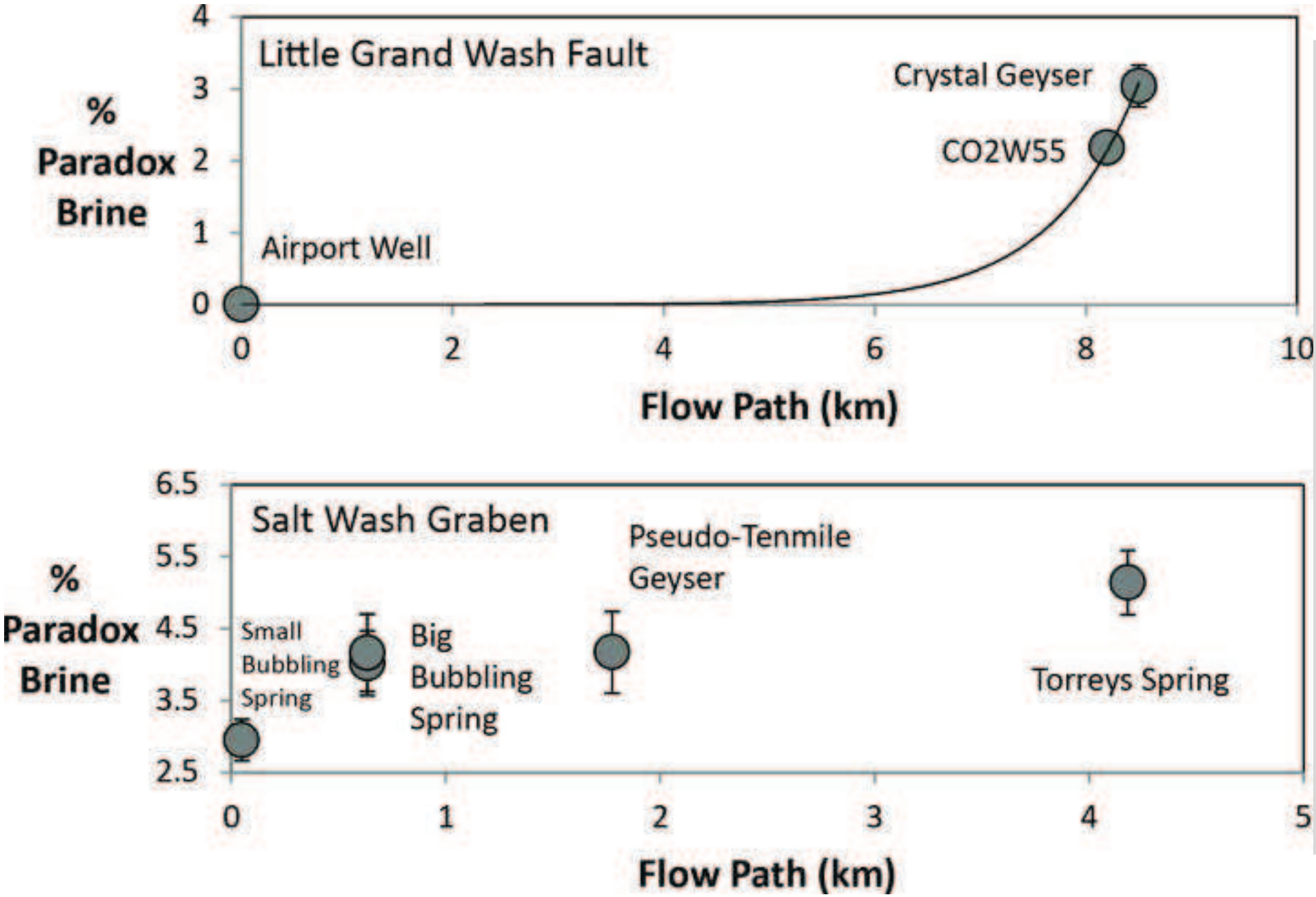

Figure 24

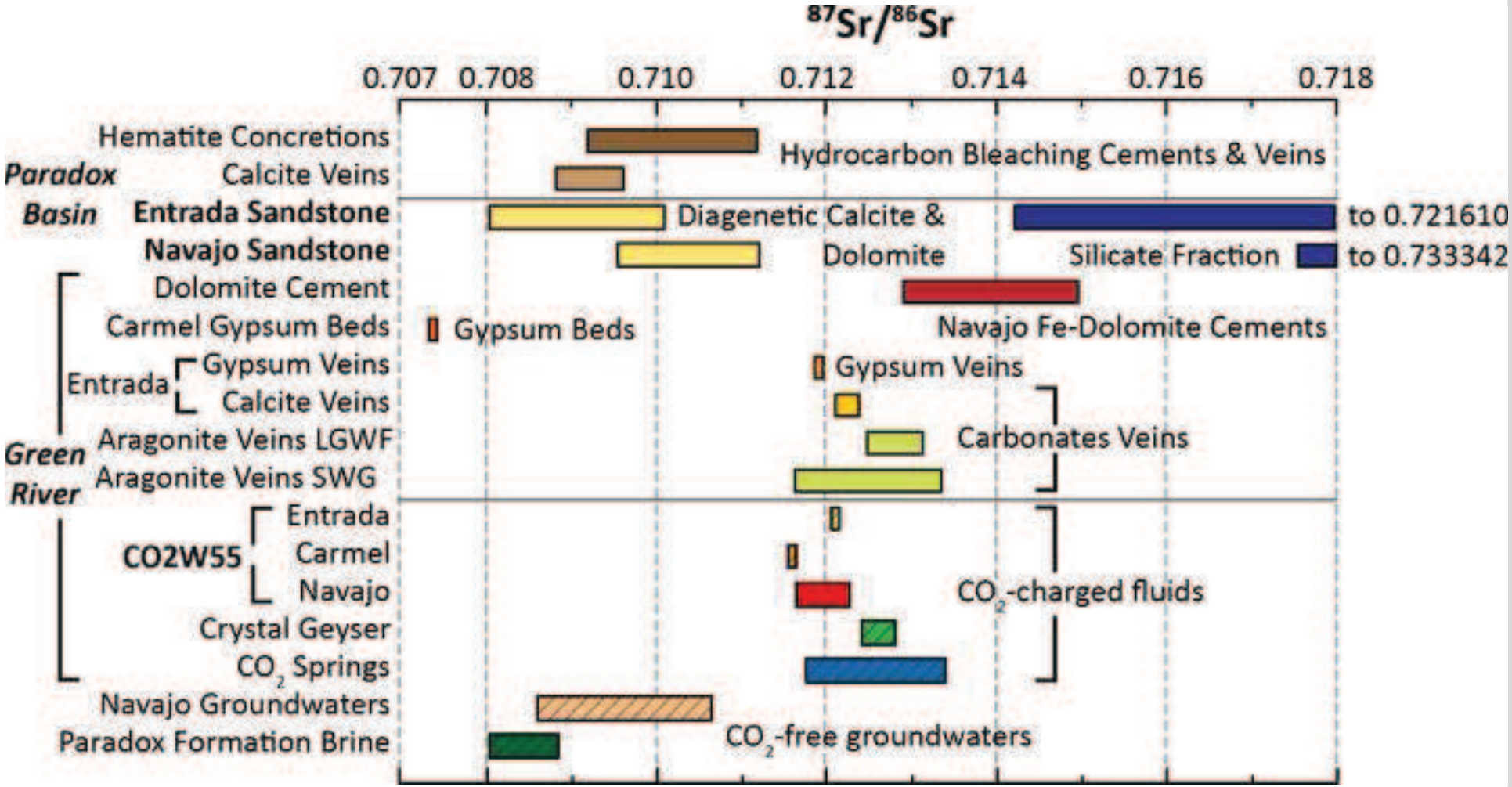

Figure 25

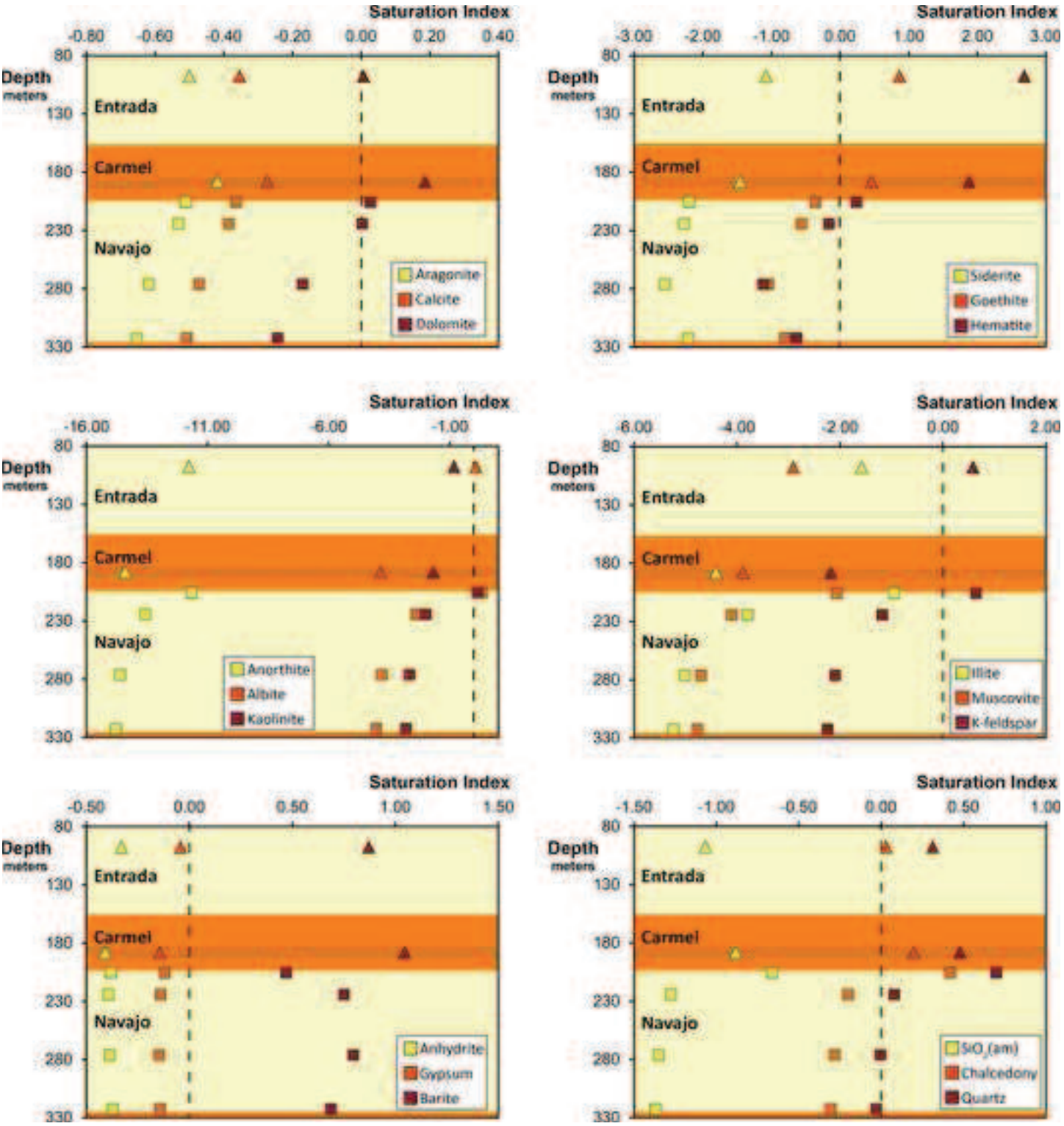

Figure 26

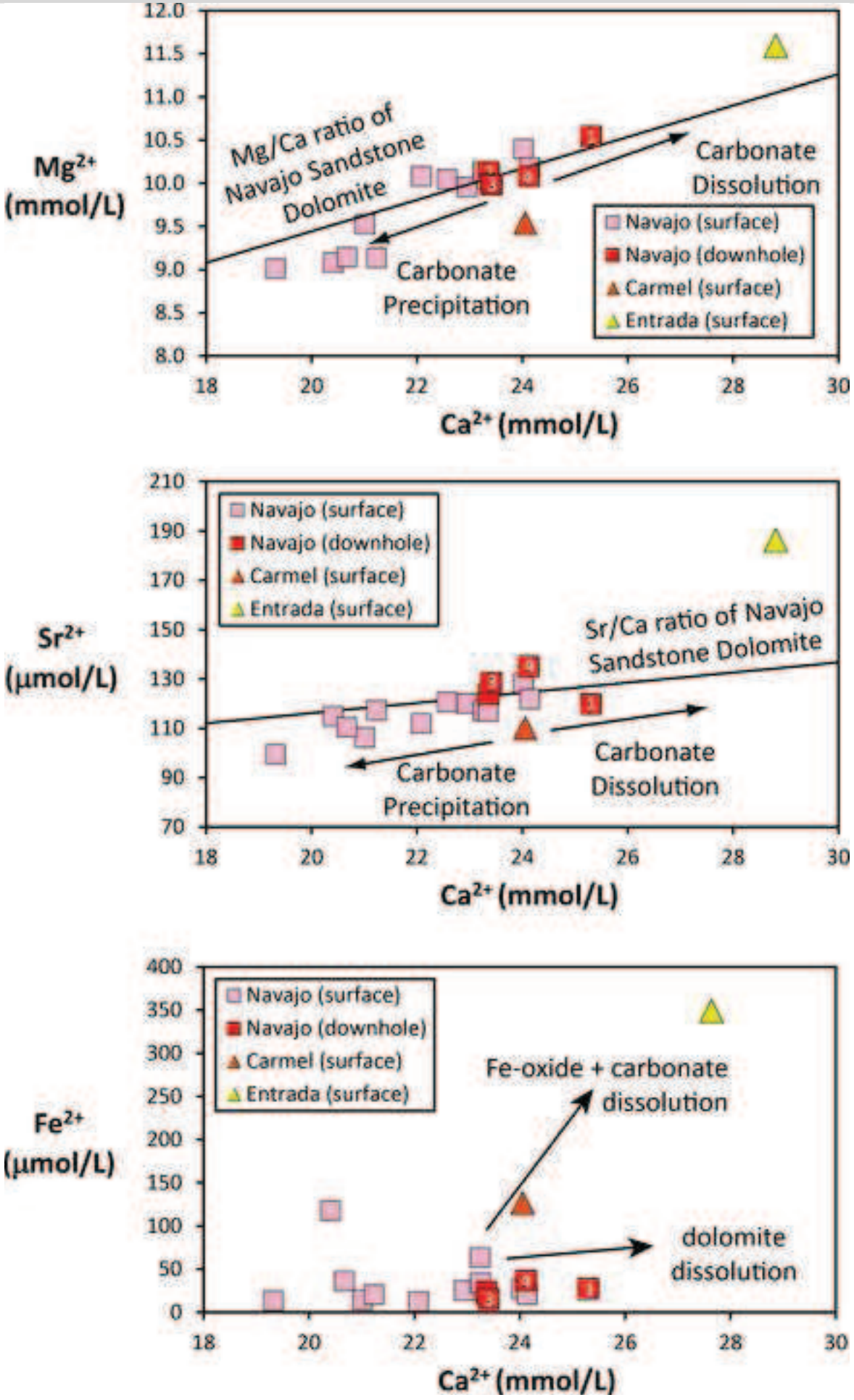

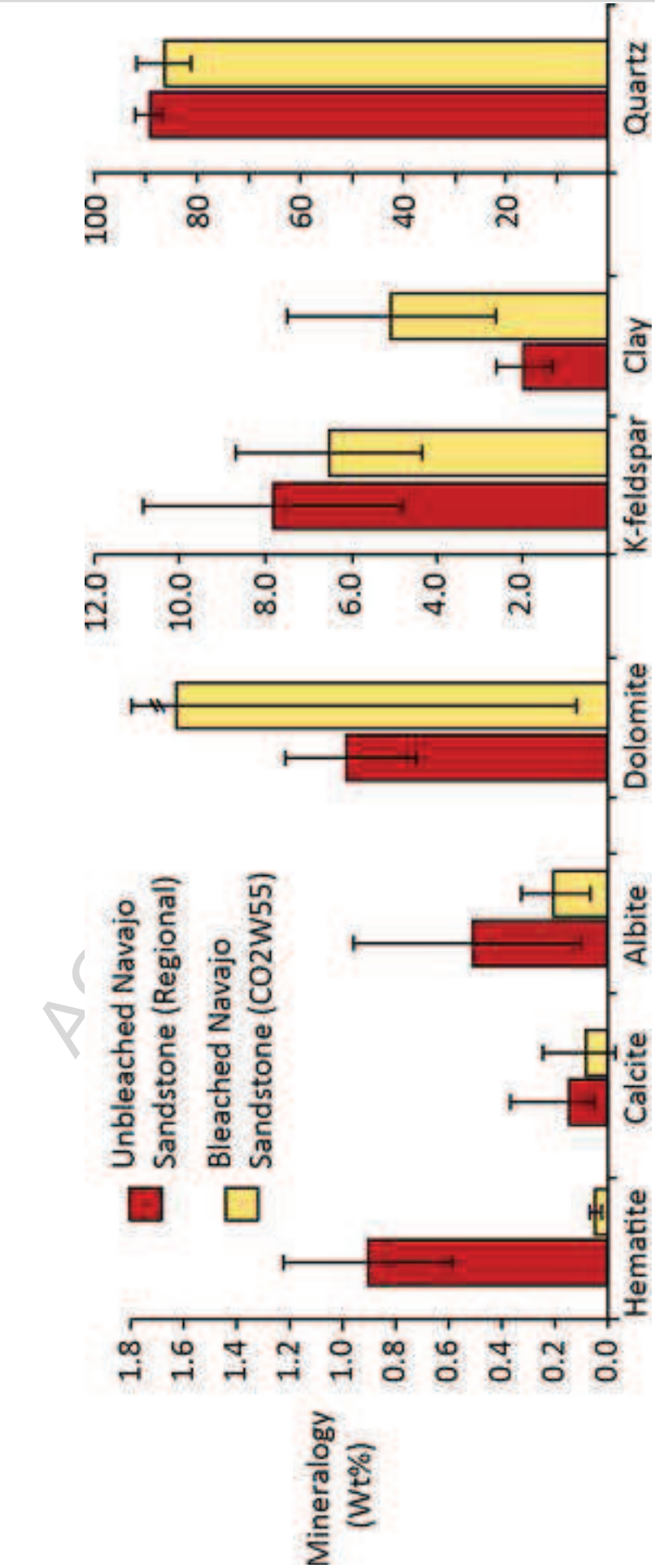

Figure 27

Figure 28

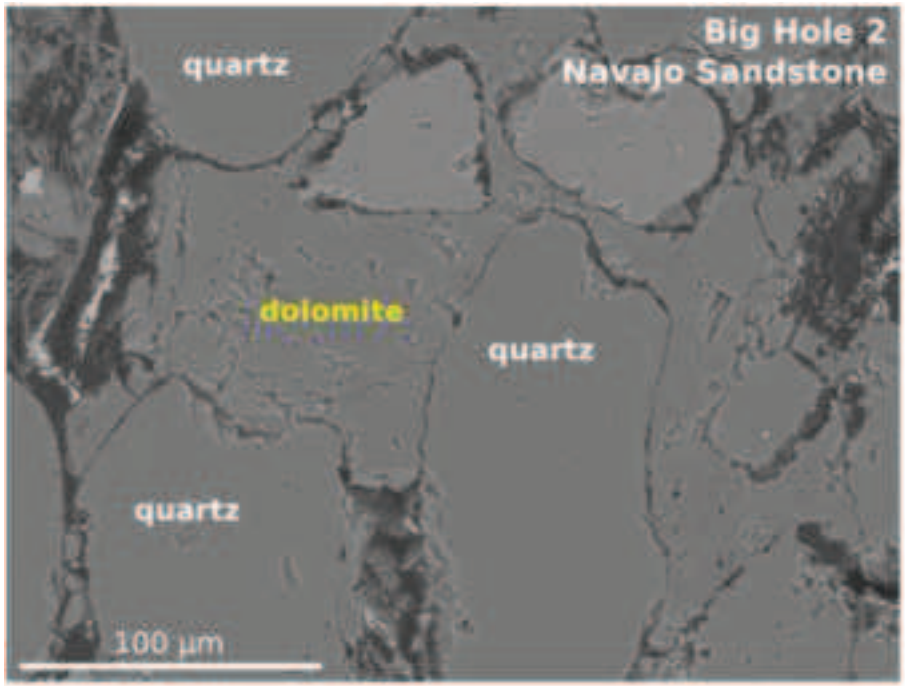

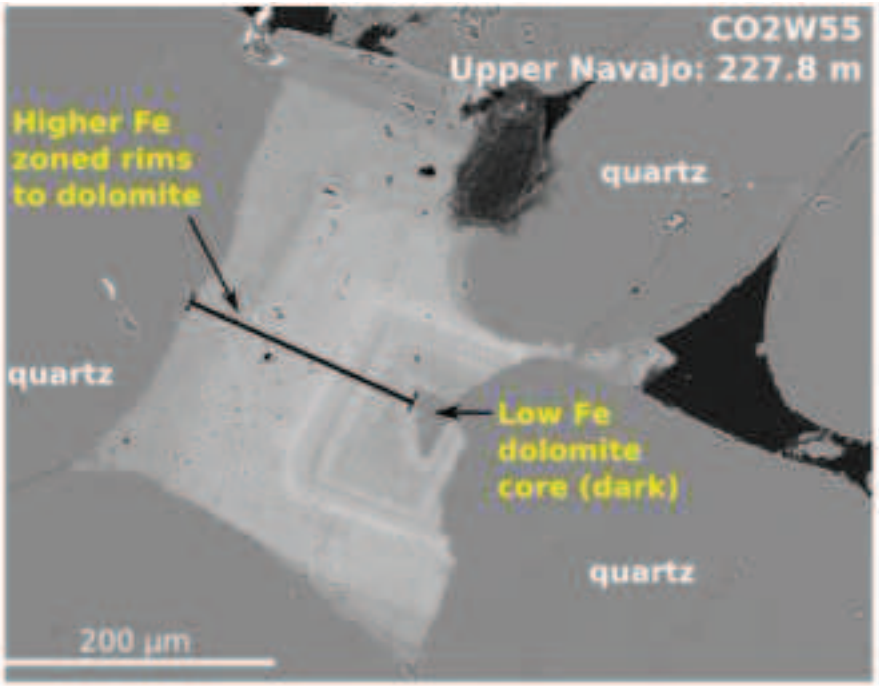

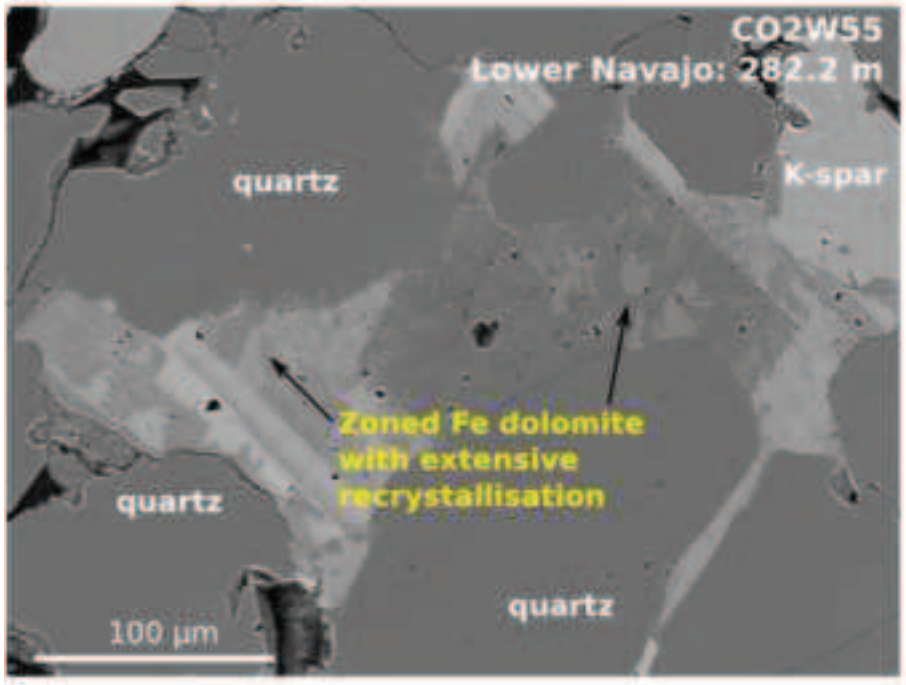

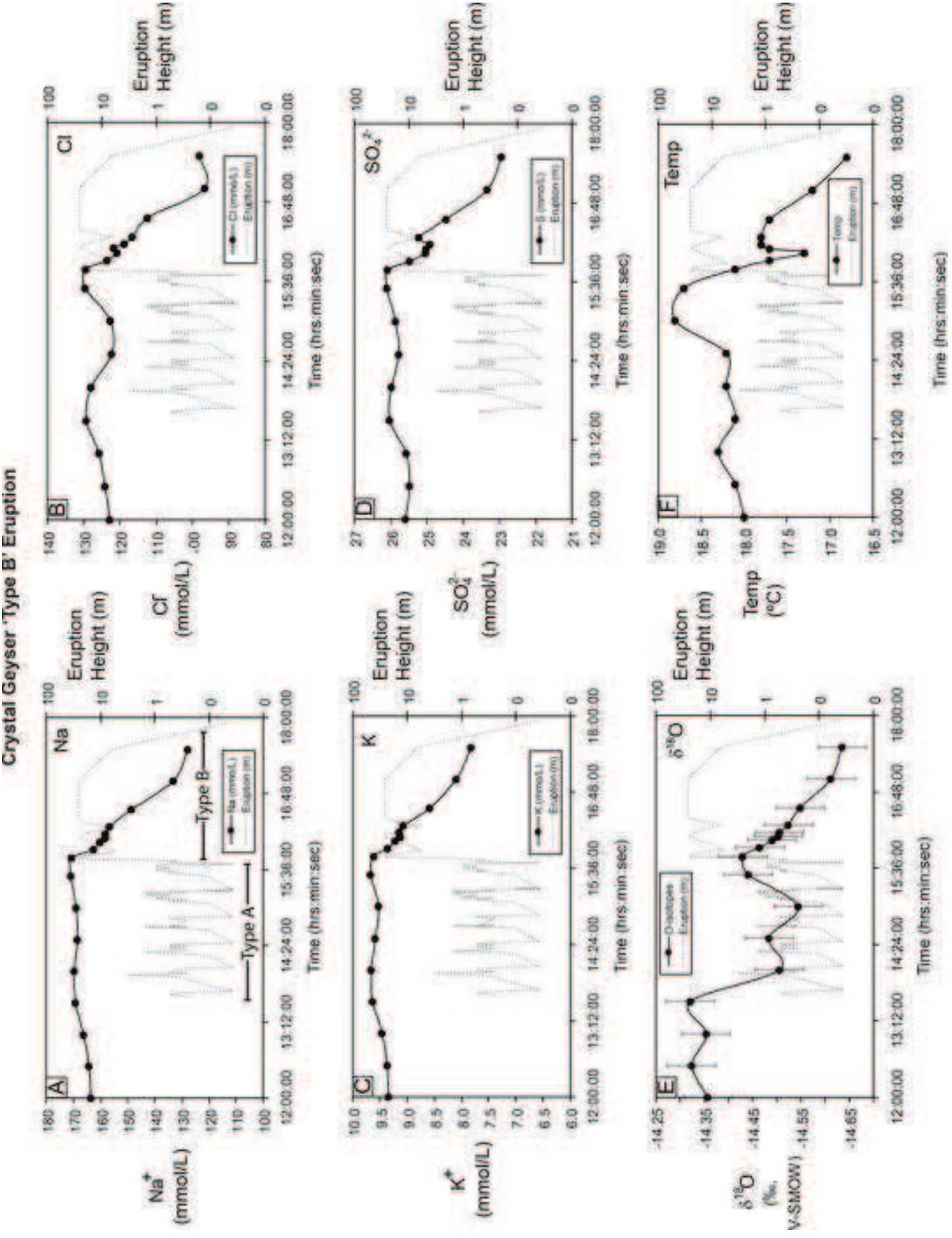

Figure 29

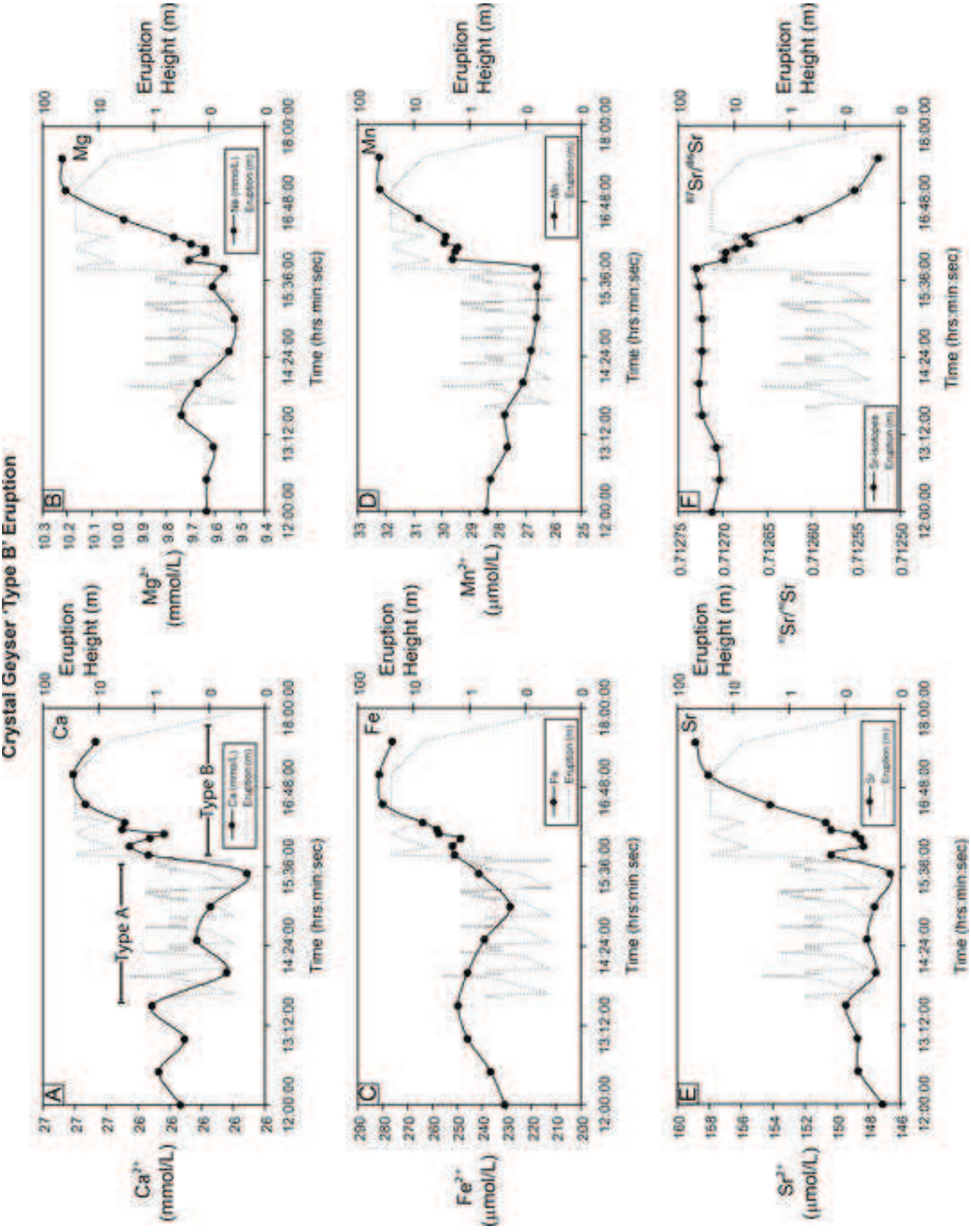

Figure 30

Figure 31

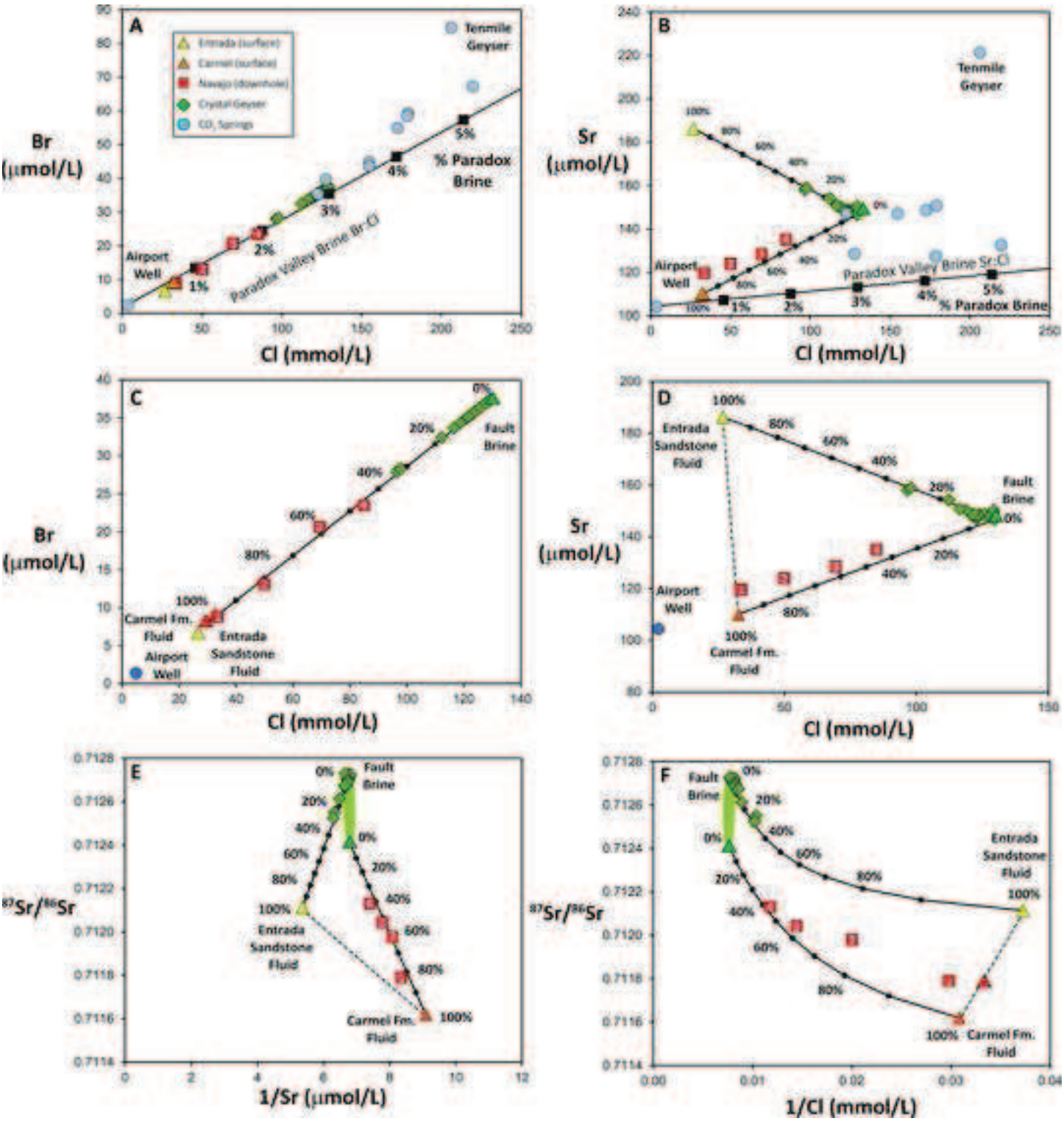

Figure 32

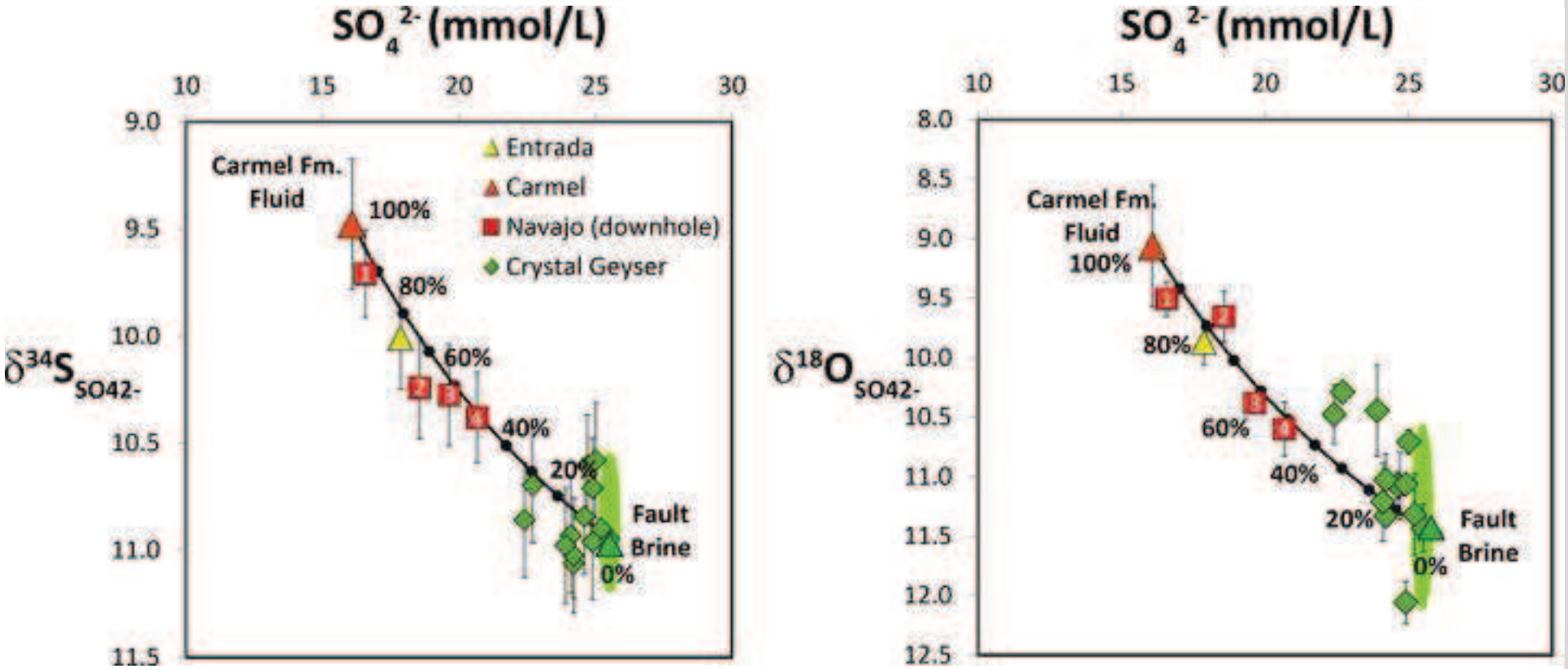

Figure 33

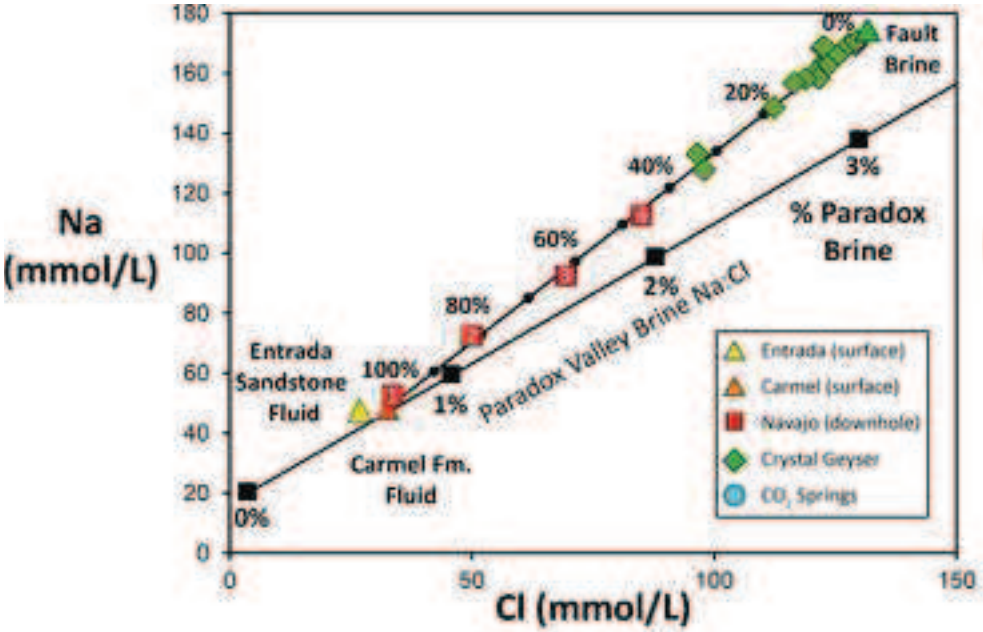

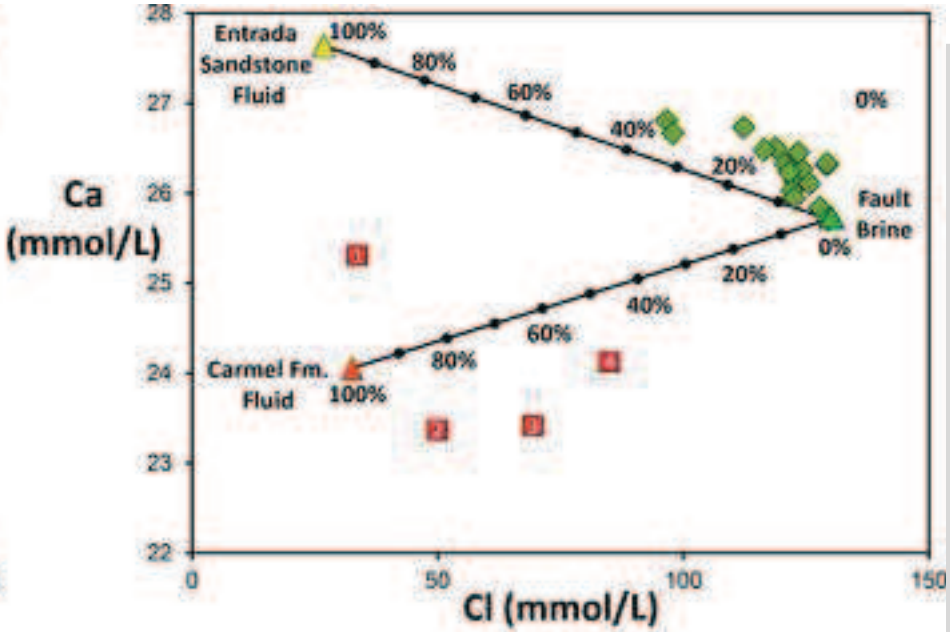

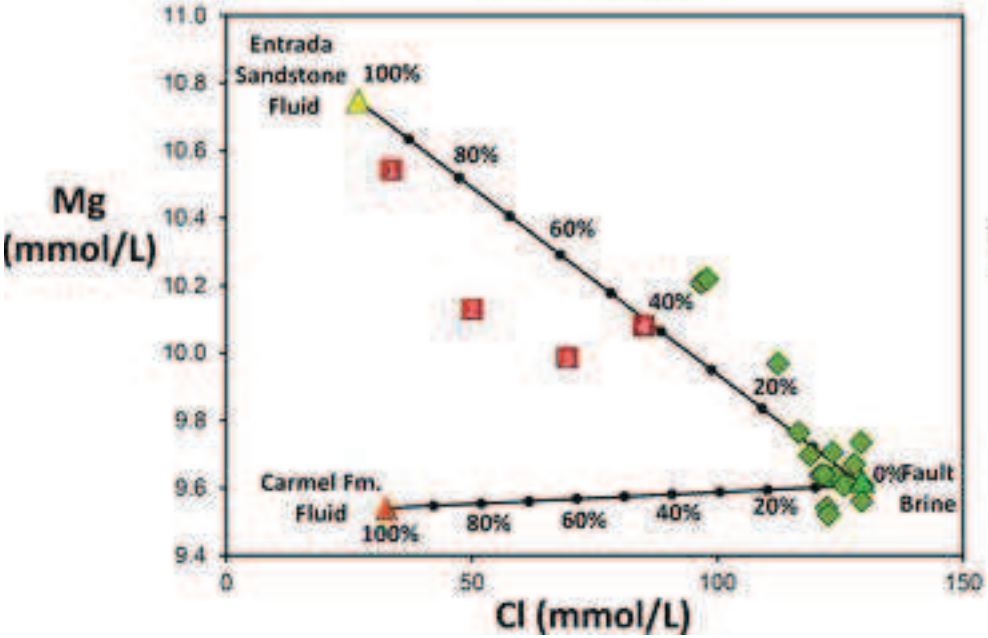

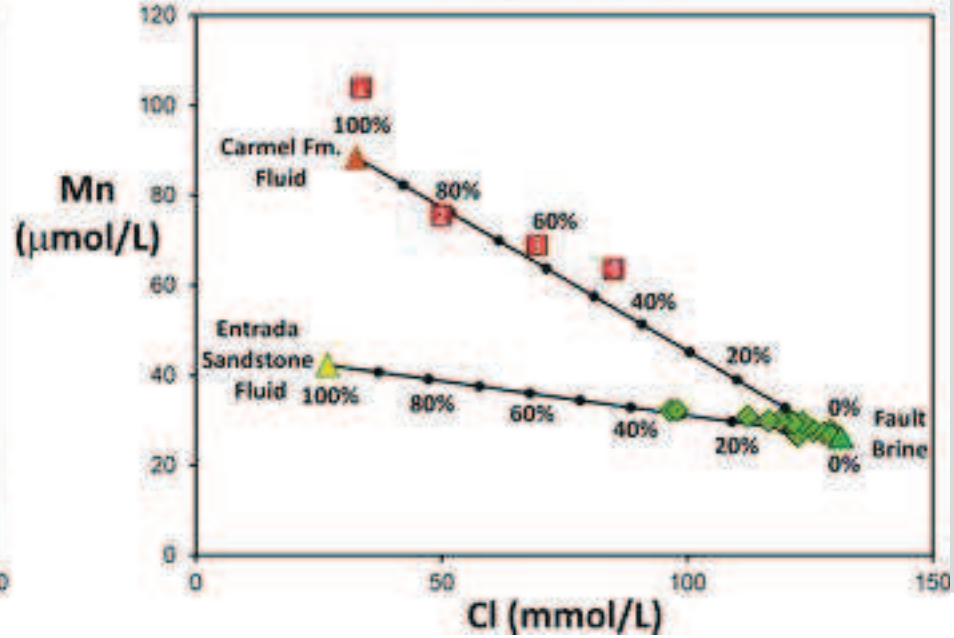

Figure 34

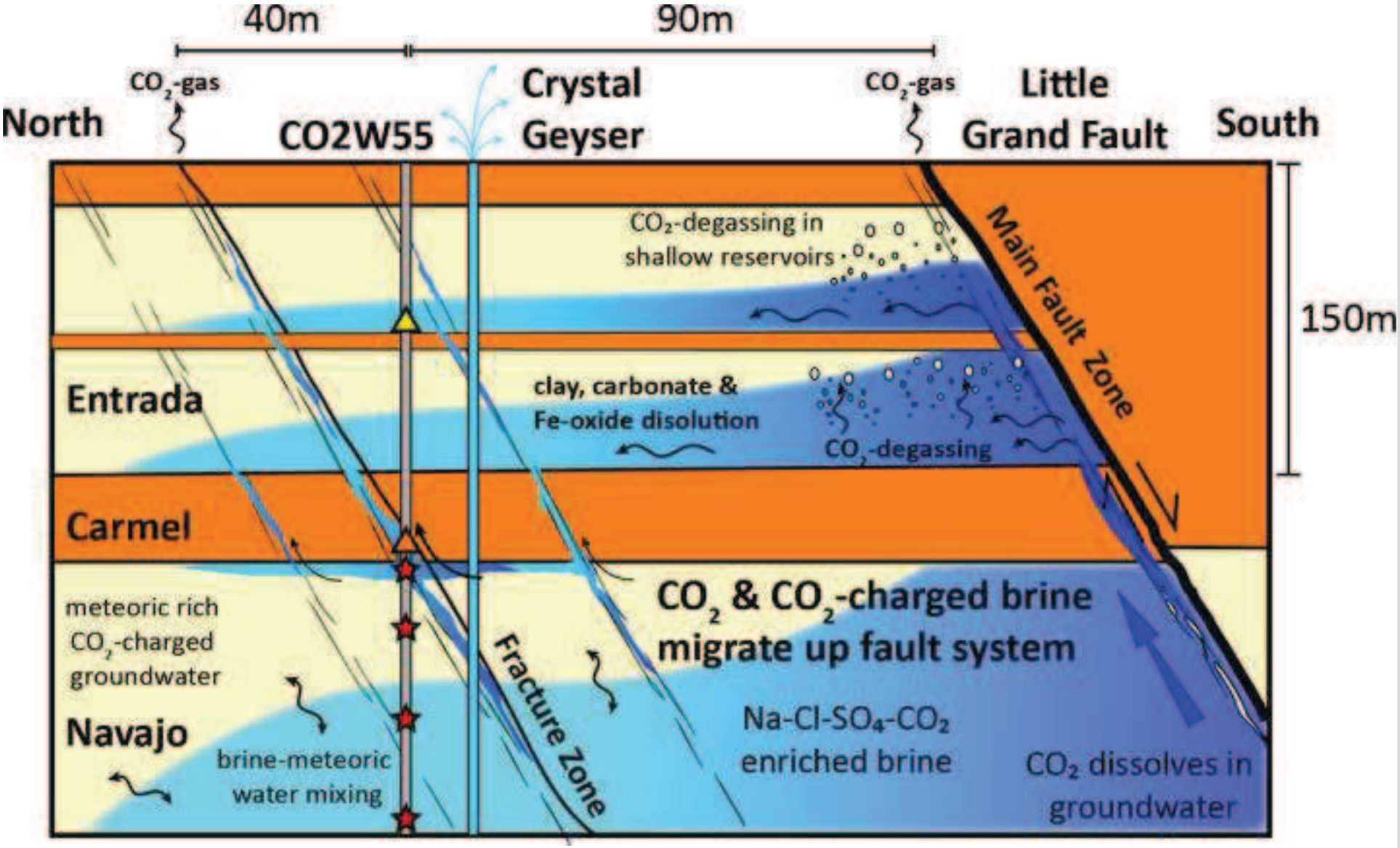

Figure 35

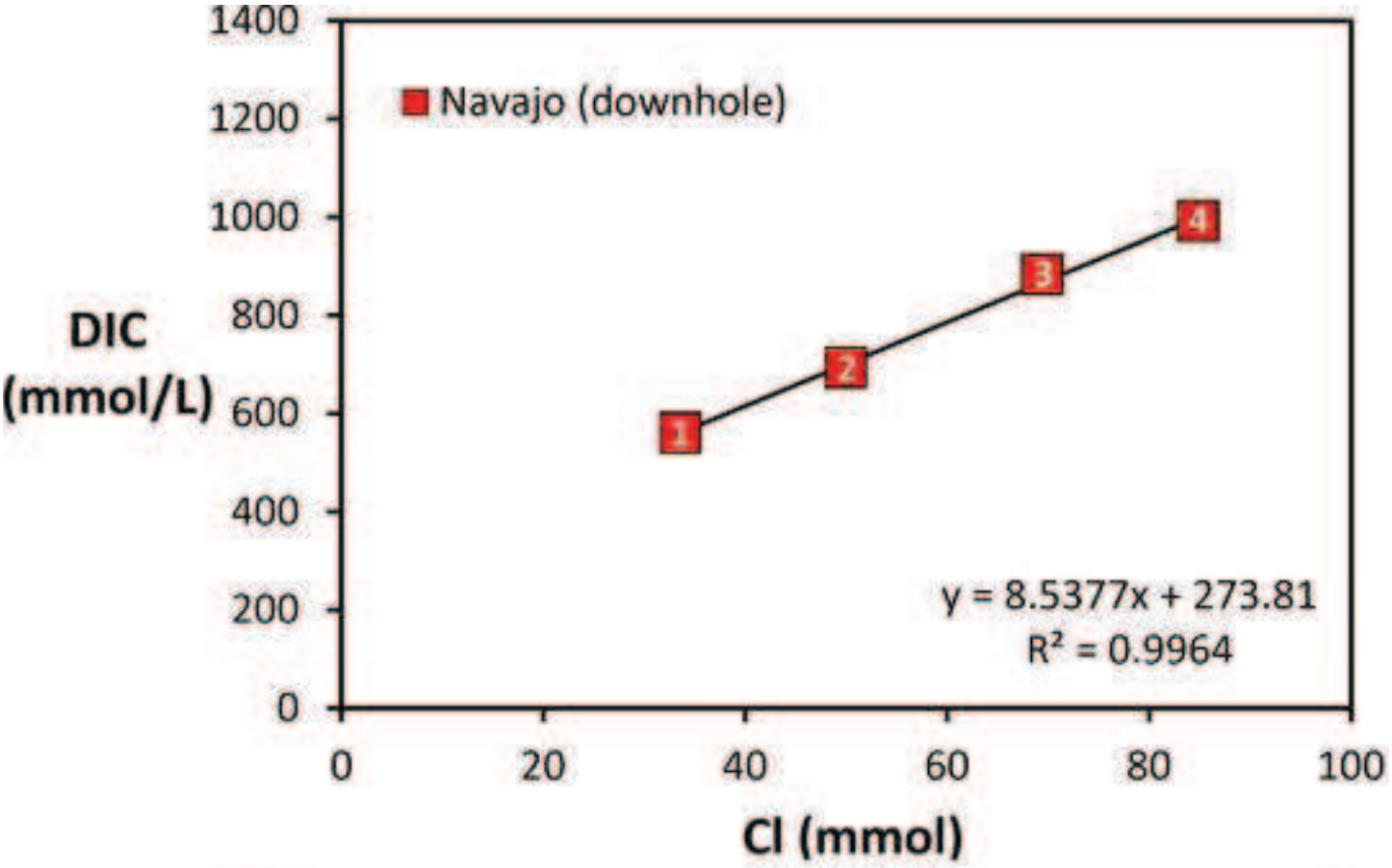

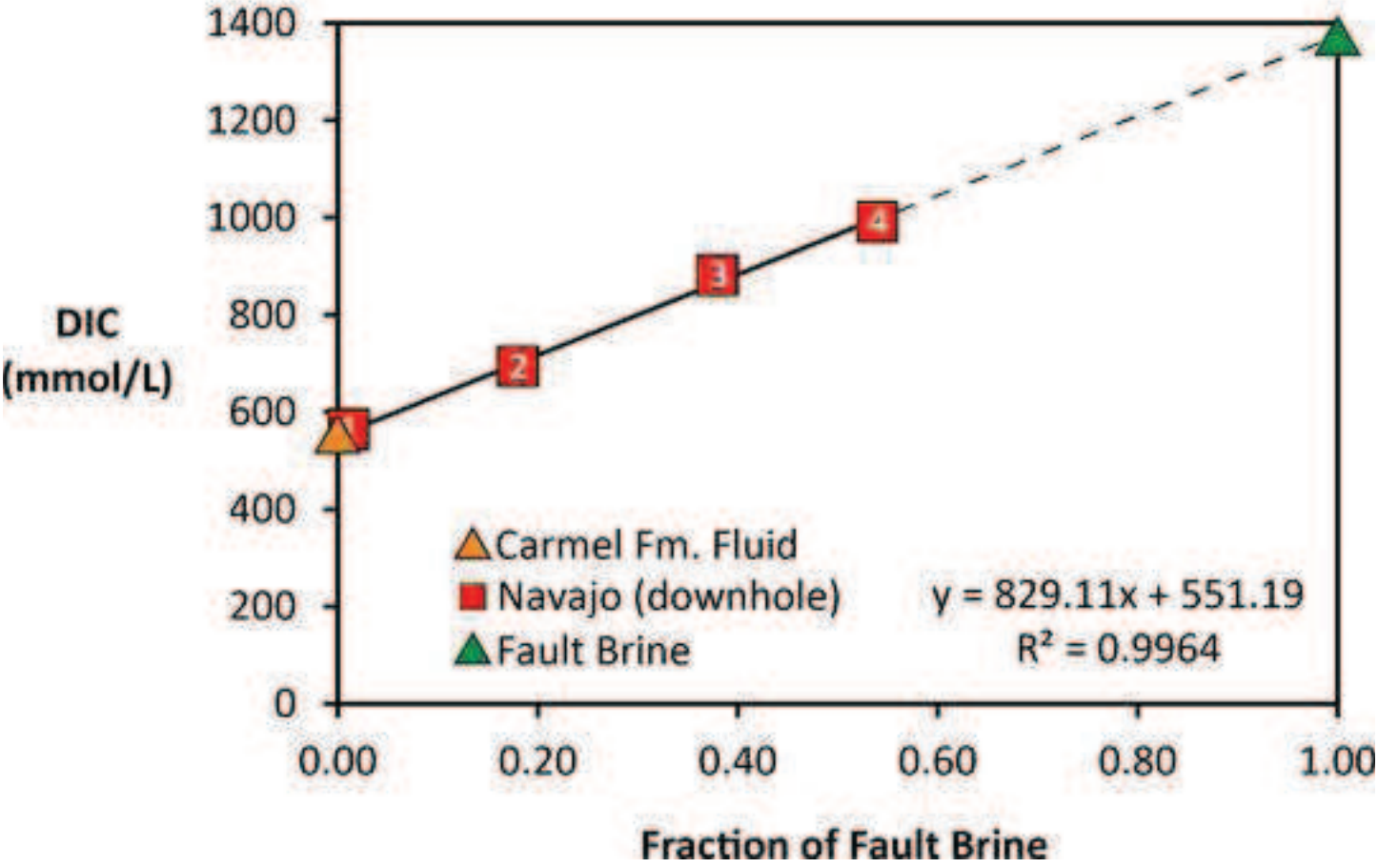

Table 1

Code	Formation	Depth	Temp	pH		DIC	Alkalinity	Al^{3+}	B^{+}	Ba^{2+}
		m	ºC	(surface)	(insitu)	mmol/l	mEq/L	µmol/l	µmol/l	µmol/l
ENTRADA	Entrada	98	13.6	6.3			45.00	0.3	67.8	0.4
UDP001	Carmel	188	15.5	6.2			56.68	7.6	88.1	0.6
DSF001	Navajo	206	15.9		5.30	561	50.62	1.6	99.5	0.2
DFS002	Navajo	224	16.3		5.21	692	59.24	1.3	130.3	0.3
DFS003	Navajo	276	17.4		5.15	882	62.14	1.3	159.9	0.4
DFS004	Navajo	322	18.3		5.13	991	63.74	1.2	191.2	0.3
UDP002	Navajo	203	15.8	6.43			38.43	1.4	104.7	0.4
UDP003*	Navajo	206	15.9	6.42			80.24	1.2	130.0	0.6
UDP004	Navajo	206	15.9	6.43			36.66	5.6	109.4	0.3
UDP005	Navajo	206	15.9	6.22			46.58	4.8	107.9	0.4
UDP006	Navajo	206	15.9	6.43			51.50	0.9	99.0	0.5
UDP007	Navajo	224	16.3	6.52			59.82	0.9	120.9	0.3
UDP008	Navajo	224	16.3	6.58			58.92	1.7	139.3	0.3
UDP009	Navajo	286	17.6	6.23			52.17	1.0	151.4	0.4
UDP010	Navajo	292	17.7	6.11			47.91	0.9	157.1	0.3
UDP011	Navajo	298	17.8	6.15			51.60	1.0	158.9	0.4
UDP012	Navajo	298	17.8	6.27			52.92	0.9	170.3	0.4
UDP013	Navajo	316	18.2	6.24			59.18	0.8	146.2	0.3
UDP014	Navajo	322	18.3	6.51			62.50	0.6	157.4	0.3

Table 2

Sample Labels	$^{87}Sr/^{86}Sr$	%error x10^{-6}	$\delta^{18}O$	δD	$\delta^{34}S$	σ	$\delta^{18}O$	σ
			VSMOW				sulphate	
ENTRADA	0.71211	6	-13.09	-110.1	10.01	0.24	9.87	0.51
UDP001	0.71162	6	-14.50	-115.7	9.48	0.34	9.06	0.19
DSF001	0.71179	8	-15.63	-116.7	9.71	0.21	9.51	0.15
DFS002	0.71198	7	-15.21	-117.5	10.24	0.24	9.66	0.21
DFS003	0.71204	7	-14.84	-115.8	10.28	0.24	10.38	0.08
DFS004	0.71213	7	-14.70	-114.6	10.38	0.21	10.60	0.23
UDP002	0.71185	7	-14.50	-115.7	#N/A	#N/A	#N/A	#N/A
UDP003	0.71192	7	-14.16	-113.0	#N/A	#N/A	#N/A	#N/A
UDP004	#N/A	#N/A	-14.11	-114.2	#N/A	#N/A	#N/A	#N/A
UDP005	0.71190	8	-13.97	-113.3	#N/A	#N/A	#N/A	#N/A
UDP006	0.71191	7	-14.28	-112.5	#N/A	#N/A	#N/A	#N/A
UDP007	0.71194	7	-15.25	-116.1	#N/A	#N/A	#N/A	#N/A
UDP008	0.71200	7	-15.30	-118.2	#N/A	#N/A	#N/A	#N/A
UDP009	0.71197	8	-14.90	-116.4	#N/A	#N/A	#N/A	#N/A
UDP010	0.71193	7	-14.58	-113.5	#N/A	#N/A	#N/A	#N/A
UDP011	0.71198	7	-14.16	-113.5	#N/A	#N/A	#N/A	#N/A
UDP012	0.71205	7	#N/A	#N/A	#N/A	#N/A	#N/A	#N/A
UDP013	0.71202	7	-14.56	-115.3	#N/A	#N/A	#N/A	#N/A
UDP014	0.71208	7	-13.96	-113.6	#N/A	#N/A	#N/A	#N/A

Table 3

Code	Spring	Latitude	Longitude	Eh	pH	Temp	Alkalinity	Al^{3+}	Ba^{2+}
				mV		ºC	mEq/L	µmol/l	µmol/l
CG001	Crystal Geyser	38.93900	-110.13550	-5	6.52	18.2	68.86	5.8	0.1
GR07009	Torreys Spring	38.85873	-110.07277	-39.6	6.51	16.4	78.72	5.8	0.0
GR07007	Tenmile Geyser	38.86272	-110.10125	-22.6	6.55	18.5	58.21	5.0	0.1
GR07004	Pseudo-Tenmile Geyser	38.86574	-110.10046	6.44	6.42	15.8	62.06	4.7	0.0
GR07018a	Chaffin Ranch Geyser	38.76350	-110.12744	-35	6.25	16	76.12	5.8	0.0
GR07002	Green River Airport Well	38.96618	-110.22624	-42	6.28	26.8	37.08	4.6	0.1
GR07012a	Big Bubbling Spring	38.87107	-110.11154	-32	6.36	17.7	66.04	5.0	0.0
GR07010	Small Bubbling Spring	38.87265	-110.11662	-7	6.24	19.2	56.54	4.3	0.1
GR07013a	Side Seep, BBS	38.86998	-110.11086	-32	6.25	17.9	59.69	4.3	0.1
GR07019	Tumble Weed Geyser	38.81984	-110.12753	-32	6.3	17.9	62.12	6.0	0.0

Table 4

Code	Spring	Ar	N_2	CO_2	CH_4	$\delta^{13}C$-CO_2
		%	%	%	vpm	‰ PVDB
CG001	Crystal Geyser	0.54	3.36	96.1	73	-6.87
GR07009	Torreys Spring	1.91	7.23	90.9	81	-6.23
GR07007	Tenmile Geyser	1.41	18.1	80.5	247	-6.89
GR07004	Pseudo-Tenmile Geyser	0.68	2.27	97.1	98	-7.09
GR07018a	Chaffin Ranch Geyser	0.68	3.6	95.5	108	-6.3
GR07002	Green River Airport Well	0.99	3.91	95.1	171	-6.28
GR07012a	Big Bubbling Spring	1.53	5.45	93	94	-6.99

Table 5

Code	Time	pH	Temp	Alkalinity	Al^{3+}	Ba^{2+}	Ca^{2+}	Fe^{2+}	K^{+}	Mg^{2+}	Mn^{2+}	Na^{+}
			ºC	mEq/L	µmol/l	µmol/l	mmol/l	µmol/l	mmol/l	mmol/l	µmol/l	mmol/l
CG1	12:00:00	6.32	18	75.59	5.82	0.08	26.13	230.60	9.35	9.63	28.40	163.56
CG2	12:30:00	6.38	18.1	69.35	5.38	0.08	26.27	236.41	9.37	9.64	28.25	164.41
CG3	13:00:00	6.38	18.3	68.98	5.56	0.07	26.11	245.59	9.46	9.61	27.63	166.21
CG4	13:30:00	6.38	18.1	64.70	6.07	0.09	26.31	249.52	9.64	9.73	27.75	169.29
CG5	14:00:00	6.38	18.2	74.53	5.39	0.07	25.84	245.61	9.66	9.67	27.08	169.69
CG6	14:30:00	6.37	18.2	62.83	6.17	0.07	26.03	238.93	9.58	9.54	26.80	168.38
CG7	15:00:00	6.31	18.8	62.67	5.31	0.08	25.94	228.53	9.52	9.52	26.60	168.87
CG8	15:30:00	6.38	18.7	68.34	5.95	0.08	25.71	240.97	9.67	9.61	26.58	170.81
CG9	15:47:00	6.57	18.1	68.71	5.99	0.07	26.33	250.77	9.61	9.56	26.62	170.65
CG10	15:55:10	6.57	17.7	71.21	6.09	0.08	26.45	251.78	9.36	9.71	29.62	162.50
CG11	16:02:00	6.55	17.3	62.66	5.75	0.08	26.32	248.30	9.22	9.64	29.51	160.07
CG12	16:06:00	6.57	17.7	69.75	5.78	0.08	26.24	257.15	9.12	9.64	29.42	158.24
CG13	16:10:00	6.55	17.8	72.49	5.85	0.07	26.50	257.88	9.14	9.70	29.89	158.09
CG14	16:16:30	6.55	17.8	58.35	5.98	0.08	26.48	263.72	9.07	9.76	29.84	156.75
CG15	16:33:00	6.55	17.7	66.23	6.47	0.08	26.73	279.75	8.58	9.97	30.81	148.57
CG16	17:00:00	6.53	17.2	64.85	5.43	0.08	26.81	281.12	8.09	10.21	32.19	133.06
CG17	17:30:00	6.56	16.8	61.11	5.49	0.08	26.67	276.02	7.82	10.22	32.23	127.74

Table 6

Code	Sample Type	Formation	Locality/Drill-hole	Latitude	Longitude	Depth metres
RS 067	Calcite Vein	Entrada	Salt Wash Graben	38.86487	-110.09982	surface outcrop
RS 092	Calcite Vein	Entrada	Salt Wash Graben	38.87023	-110.11190	surface outcrop
RS 073	Gypsum Vein	Entrada	Salt Wash Graben	38.86655	-110.10241	surface outcrop
RS 073	Gypsum Vein	Entrada	Salt Wash Graben	38.86655	-110.10241	surface outcrop
RS 073	Gypsum Vein	Entrada	Salt Wash Graben	38.86655	-110.10241	surface outcrop
525.5	Gypsum Bed	Carmel	CO2W55	38.93792	-110.13892	160.2
NRS053	Sandstone	Navajo	CO2W55	38.93792	-110.13892	227.8
NRS097	Sandstone	Navajo	CO2W55	38.93792	-110.13892	259.7
A638/1	Sandstone	Navajo	Blaze #1-C	38.98117	-109.84936	1419.6
K3B	Siltsone/sandstone	Kayenta	San Rafael Swell	38.92237	-110.44165	surface outcrop
W9	Sandstone	Wingate	San Rafael Swell	38.92374	-110.44413	surface outcrop

Table 7

Code	Drill-hole	Formation	Depth	Quartz	Albite	K-feldspar	Illite	Calcite	Dolomite
			metres				wt. %		
CNH 2A	CO2W55	Navajo	206.94	88.8	0.0	5.5	4.0	0.0	1.7
CNN 9B	CO2W55	Navajo	226.83	93.0	0.1	2.5	4.0	0.2	0.3
CNH-20	CO2W55	Navajo	237.74	80.5	0.2	8.3	6.0	0.0	4.8
CNH-31	CO2W55	Navajo	248.41	80.4	0.4	8.7	7.7	0.4	2.4
CNH-41	CO2W55	Navajo	250.85	92.0	0.3	5.8	1.5	0.0	0.4
CNH-50	CO2W55	Navajo	272.06	88.5	0.1	6.7	3.7	0.0	0.8
CNH-57	CO2W55	Navajo	282.21	82.1	0.3	8.0	8.4	0.0	1.1

Table 8.

Entrada Sandstone	Na	K	Ca	Mg	Sr	Fe	Mn	SO_4	Br	Cl	HCO_3
predicted	41.2	3.7	28.8	11.6	186.2	354.6	44.9	16.4	7.8	26.8	44.9
measured	47.6	3.3	27.6	10.7	186.3	348.9	42.3	17.9	6.7	26.8	45.0
% Difference	-14.0	13.4	4.2	7.8	0.0	1.6	6.2	-8.1	15.3	0.0	-0.3

Fault Brine	Na	K	Ca	Mg	Sr	Fe	Mn	SO_4	Br	Cl	HCO_3
predicted	164.7	8.9	23.1	9.7	148.4	45.1	28.6	24.2	36.2	129.6	75.2
measured	170.8	9.7	25.7	9.6	146.7	241.0	26.6	25.5	37.4	129.6	68.3
% Difference	-3.6	-7.4	-10.2	0.7	1.2	**-81.3**	7.4	-5.0	-3.2	0.0	10.0

Carmel Formation	Na	K	Ca	Mg	Sr	Fe	Mn	SO_4	Br	Cl	HCO_3
predicted	51.3	5.1	25.3	10.6	119.4	26.7	104.7	16.5	8.5	32.5	50.3
measured	48.3	4.8	24.1	9.5	110.1	126.8	88.5	16.8	9.3	32.5	56.7
% Difference	6.1	6.1	5.3	10.6	8.5	**-78.9**	**18.3**	-2.1	-8.6	0.0	-11.2

Highlights

- We discuss drilling of a natural CO_2 reservoir and CO_2-degassing fault.
- Pressurized fluids for geochemistry, pH and CO_2 content were recovered.
- The fluids dissolve hematite and carbonate minerals as they flow away from the fault.
- Fluid geochemistry shows CO_2 is effectively dissolved during migration.
- Switching of reservoir source coincides with eruption onset of a CO_2-geyser